LA-UR- 99 5430

Approved for public release; distribution is unlimited

Title: MEASUREMENT OF THE PARITY-VIOLATING GAMMA ASYMMETRY A_gamma IN THE CAPTURE OF POLARIZED COLD NEUTRONS BY PARA-HYDROGEN, n(arrow) + p -> d+gamma

Author(s): A. Bazhenov, C.S. Blessinger, J.D. Bowman, T.E. Chupp, K.P. Coulter, S.J. Freedman, B.K. Fujikawa, T.R. Gentile, G.L. Greene, G.L. Hansen, G.E. Hogan, S. Ishimoto, G.L. Jones, J.N. Knudson, E. Kolomenski, S.K. Lamoreaux, M.B. Leuschner, A. Masaike, Y. Masuda, Y. Matsuda, G.L. Morgan, K. Morimoto, C.L. Morris, H. Nann, S.I. Penttila, A. Pirozhkov, V.R. Pomeroy, D.R. Rich, A. Serebrov, E.I. Sharapov, D.A. Smith, W.M. Snow, T.B. Smith, R.C. Welsh, F.E. Wietfeldt, W.S. Wilburn, V.W. Yuan, and J. Zenger

Submitted to:

Los Alamos
NATIONAL LABORATORY

Los Alamos National Laboratory, an affirmative action/equal opportunity employer, is operated by the University of California for the U.S. Department of Energy under contract W-7405-ENG-36. By acceptance of this article, the publisher recognizes that the U.S. Government retains a nonexclusive, royalty-free license to publish or reproduce the published form of this contribution, or to allow others to do so, for U.S. Government purposes. Los Alamos National Laboratory requests that the publisher identify this article as work performed under the auspices of the U.S. Department of Energy. Los Alamos National Laboratory strongly supports academic freedom and a researcher's right to publish; as an institution, however, the Laboratory does not endorse the viewpoint of a publication or guarantee its technical correctness.

Form 836 (10/96)

Author list for

MEASUREMENT OF THE PARITY-VIOLATING GAMMA ASYMMETRY A_γ IN THE CAPTURE OF POLARIZED COLD NEUTRONS BY PARA-HYDROGEN, $\vec{n} + p \rightarrow d + \gamma$

A. Bazhenov, C.S. Blessinger, J.D. Bowman, T.E. Chupp, K.P. Coulter, S.J. Freedman, B.K. Fujikawa, T.R. Gentile, G.L. Greene, G.L. Hansen, G.E. Hogan, S. Ishimoto, G.L. Jones, J.N. Knudson, E. Kolomenski, S.K. Lamoreaux, M.B. Leuschner, A. Masaike, Y. Masuda, Y. Matsuda, G.L. Morgan, K. Morimoto, C.L. Morris, H. Nann, S.I. Penttila, A. Pirozhkov, V.R. Pomeroy, D.R. Rich, A. Serebrov, E.I. Sharapov, D.A. Smith, W.M. Snow T.B. Smith, R.C.Welsh, F.E. Wietfeldt, W.S. Wilburn, V.W. Yuan, and J. Zerger.

Measurement of the Parity-Violating Gamma Asymmetry A_γ in the Capture of Polarized Cold Neutrons by Para-Hydrogen, $\vec{n} + p \rightarrow d + \gamma$

J.D. Bowman (Spokesman), G.L. Greene, G.E. Hogan, J.N. Knudson, S.K. Lamoreaux, G.L. Morgan, C.L. Morris, S.I. Penttilä, D.A. Smith, T.B. Smith, W.S. Wilburn, and V.W. Yuan
Los Alamos National Laboratory

A. Bazhenov, E. Kolomenski, A. Pirozhkov, and A. Serebrov
Petersburg Nuclear Physics Institute

C.S. Blessinger, G. Hansen, H. Nann, D.R. Rich, and W.M. Snow
Indiana University

T.E. Chupp, K.P. Coulter, R.C. Welsh, and J. Zerger
University of Michigan

S.J. Freedman and B.K. Fujikawa
University of California, Berkeley

T.R. Gentile, G.L. Jones, and F.E. Wietfeldt
National Institute of Standards and Technology

M.B. Leuschner and V.R. Pomeroy
University of New Hampshire

A. Masaike and Y. Matsuda
Kyoto University

S. Ishimoto, Y. Masuda, and K. Morimoto
KEK National Laboratory, Japan

E.I. Sharapov
Joint Institute for Nuclear Research, Dubna

Submitted to the U.S. Department of Energy
17 April 1998

Abstract

We propose to measure the parity-violating asymmetry A_γ of the correlation between the direction of emission of the gamma ray $\vec{k}_\gamma$ and the neutron polarization $\vec{s}_n$ in the reaction $\vec{n} + p \rightarrow d + \gamma$. This asymmetry is expected to be $\approx 5 \times 10^{-8}$. We argue that it is possible to obtain a statistical uncertainty of 0.5×10^{-8} at LANSCE. We argue that systematic errors are expected to be small compared to the statistical error. The symmetries of the strong, weak, and electromagnetic interactions imply that A_γ is determined by the $\Delta I = 1$ part of the weak interaction. The sensitivity of the deuteron wave function to the long-range components of the NN interaction implies that A_γ is dominated by the longest-range $\Delta I = 1$ contribution, which is due to weak pion exchange. The asymmetry, A_γ, can therefore be related to the weak isovector pion-nucleon-nucleon coupling, H^1_π, with negligible uncertainty due to nuclear structure. (We use the definition of the weak nucleon-nucleon couplings of Adelberger and Haxton [1].) We will determine H^1_π with an uncertainty of 1.0×10^{-7}, 10% of its expected value, 1.1×10^{-6}. At present there are two experiments; gamma ray circular polarization for ^{18}F ($H^1_\pi < 0.3 \times 10^{-6}$) and the anapole moment of ^{133}Cs ($H^1_\pi = 2.4 \pm 0.6 \times 10^{-6}$) that have been interpreted to give very different values of H^1_π.

There are three physics goals that this measurement addresses, matched to three different energy regimes. A measurement of H^1_π to the proposed accuracy will fix its value, thereby resolving the current controversy. We outline a feasible and partially complete program of measurements that will over-constrain the weak NN couplings. Completion of this program will finally allow parity violation measurements to be used to address questions in nuclear physics. A reliable measurement of H^1_π is an essential part of an experimental program to over-determine the weak NN couplings and thereby test the internal consistency of the meson-exchange picture of the weak NN interaction. Such a test of the meson exchange picture has the potential to tell us something new about low energy QCD, especially if the meson picture fails. Finally, since the $\Delta I = 1$ flavor-conserving weak NN interaction is dominated by quark-quark neutral currents at the electroweak scale, we can learn how the effective strength of quark-quark neutral currents is modified by QCD.

Contents

1 Introduction 3

1.1 Discussion of Mass Scales of the Weak Interactions 4

1.2 Status of Our Knowledge of the Weak Meson-Nucleon Couplings 8

1.2.1 Theoretical Estimates of the Sizes of the Weak Meson-Exchange Couplings . 8

1.2.2 What We Know from Experiments 9

1.3 Strategy to Determine the Couplings from Two-Nucleon Experiments 12

1.4 Calculations of H_s^1 13

1.5 Symmetry Considerations for $\vec{n} + p \to d + \gamma$ 14

1.6 Role of the hadronic weak interaction in the study of the weak interaction 15

1.7 Search for New Weak Neutral Gauge Bosons 15

1.8 Summary 15

2 Advantages of LANSCE 16

3 Description of the Proposed Experiment 17

3.1 Neutron Source and Optimization of the Experimental Configuration 17

3.2 Neutron Polarizer 24

3.2.1 Polarizing Super Mirrors 24

3.2.2 Neutron Polarization with a ^{3}He Spin Filter 25

3.3 RF Spin Flipper 31

3.4 Liquid Para-Hydrogen Target 32

3.4.1 Target Vessel 33

3.4.2 Ortho–Para-Hydrogen Conversion 35

3.4.3 Cryocooler 35

3.4.4 Vacuum system 36

3.4.5 Hydrogen Safety 36

3.4.6 Instrumentation 37

3.5 Gamma Detector 38

3.5.1 Cesium Iodide Scintillators 38

3.5.2 Current Mode Signal 40

3.5.3 Amplification of Photocathode Signal 40

3.6 Detector Electronics 41

3.6.1 Low-Noise Preamplifiers 42

3.6.2 Sum and Difference Amplifiers 42

3.7 Data Acquisition System 42

3.7.1 VME-Based Data Acquisition Electronics 44

3.7.2 PC-based Data Acquisition System (PC DAQ) 44

3.7.3 Data Storage and Distribution 45

3.8 Magnetic Guide Field 45

4 Systematic Effects in the Experiment $\vec{n} + p \rightarrow d + \gamma$ 46
4.1 Statistical Errors . . . 46
4.2 Sources of Systematic Effects . . . 46
4.2.1 Systematic Errors of Instrumental Origin . . . 46
4.2.2 Systematic Errors from Interactions of the Neutron Spin . . . 48
4.2.3 Time-Dependent Effects . . . 51
4.3 Online Diagnostics . . . 53
4.3.1 Identification of Systematic Effects . . . 53
4.3.2 Target Diagnostics . . . 54
4.4 Auxiliary Measurements . . . 56

5 Progress to Date 57
5.1 Test Run . . . 57
5.1.1 Current-Mode Signal . . . 59
5.1.2 Electronic Noise . . . 60
5.1.3 Spectral Density . . . 61
5.1.4 Detector Sensitivity to Magnetic Fields . . . 61
5.2 Development of the Detector Electronics . . . 61
5.3 Computer Modeling . . . 63
5.3.1 Neutrons in the Liquid Para-Hydrogen Target . . . 63
5.3.2 Modeling of CsI Detector Array . . . 67
5.4 Neutron Guide and Shutter . . . 70

6 Progress Expected in the Near Future 72

7 Conclusion 72

A Budget and Manpower 74

B Schedule 78

C Personnel 79

D Publications and Presentations 84

1 Introduction

The hadronic weak interaction manifests itself in parity-violating phenomena both in the two-nucleon system and in nuclei. A parity-violating signal is necessary to isolate experimentally the hadronic weak interaction (which does not conserve parity) from the much larger effects of the strong and electromagnetic interactions (which conserve parity). The weak interaction between nucleons in a nucleus was first observed in experiments on low energy polarized neutron capture in 1964 [2]. Since the pioneering experiments of Abov, parity-violating phenomena in nuclei have been extensively studied experimentally. Parity-violating alpha transitions, parity-violating circular γ-ray polarizations, parity-violating asymmetries from polarized nuclei, and most recently anapole moments of nuclear ground states have been observed and measured with good precision.

Although a theoretical framework (the weak meson-exchange potential) has been developed, the theoretical understanding of weak interactions in nuclei has not kept pace with experiment. In particular:

1. The weak couplings that give the spin, isospin, position, and momentum dependence of the potential have not yet been determined.
2. The validity of the description of the weak interaction in nuclei using a meson-exchange potential model has not been established.
3. A quantitative description of many measured parity-violating observables does not exist.

The determination of the weak meson-exchange couplings from measurements in nuclei has been difficult because the observables depend on the nuclear wave functions of the states involved in either transitions or moments. These wave functions can not be exactly calculated, except in few-nucleon systems. Measurements of parity violation have been made in the two-nucleon pp system, where nuclear structure does not effect the interpretation. However, as discussed below, these observables depend upon the weak ρ and ω couplings. In order to unambiguously determine the long-range $\Delta I = 1$ component of the weak interaction carried by the pion, measurements in the np system are required.

The aim of the present proposal is to determine experimentally the most important of the couplings in the weak meson exchange potential, the weak pion-nucleon coupling H^1_π. As in the pp system, there will be no ambiguity in the interpretation of the result arising from nuclear structure. We will measure the parity-violating directional correlation A_γ between the spin direction of polarized neutrons and the γ-ray direction in the reaction $\vec{n} + p \rightarrow d + \gamma$. The observed asymmetry depends on only one of the couplings, the $\Delta I = 1$ pion coupling H^1_π, and therefore the lack of knowledge of the other couplings does not affect the determination of H^1_π. The weak exchange of the π, which is the lightest meson, contributes the longest-range component to the weak meson-exchange potential. In addition, the weak exchange of the pion contributes only to the $\Delta I = 1$ channel.

The determination of H^1_π is important for several reasons:

1. A knowledge of H^1_π is necessary to understand and interpret measurements of parity-violating observables in complex nuclei. For example, we discuss below a controversy concerning the interpretation of the measured anapole moment of ^{133}Cs involving the value of H^1_π.
2. The knowledge of H^1_π is an essential part of a program of measurements in two-nucleon systems to determine a complete set of the couplings in the weak meson-exchange potential. Such a program is both feasible, and partially complete.

3. In fact enough measurements in the two-nucleon system are possible to over constrain the weak meson-exchange couplings and test the validity of the meson exchange description of the weak force between nucleons. Once the weak meson-exchange potential has been established by measurements in two-nucleon systems, the interpretation of parity-violating phenomena in finite nuclei will be reduced to understanding the nuclear structure of the states involved.

4. A knowledge of H_w^2 will stimulate theoretical work to calculate H_w^1 starting from the standard-model description of weak interactions and a QCD description of the strong interactions.

1.1 Discussion of Mass Scales of the Weak Interactions

During the same period that parity-violating phenomena were being investigated in nuclei, there was rapid progress in experiments and theory studying weak interactions and decays of particles. As quarks were discovered and the electroweak theory was developed to explain leptonic and semi-leptonic weak processes and predict neutral weak currents, the parameters describing the weak interactions of quarks were fixed. $W^{\pm}$ and Z^0 boson production experiments at LEP and Fermilab verified that the strengths of $qqW^{\pm}$ and qqZ^0 weak couplings could be described by the standard model [3, 4, 5, 6, 7].

The challenge now is to connect the standard model description of the hadronic weak interaction across mass scales. These mass scales range from 100 GeV to the spacing of nuclear levels, 1 MeV. At the highest mass scale, that appropriate for the weak interactions of point-like leptons, QCD effects are small and the quark-quark weak interaction effects can be calculated. At lower mass scales, the appropriate degrees of freedom become composite and the role of the strong interaction becomes crucial. In order to put the problem of the weak interactions between nucleons in context we will briefly discuss these mass scales.

The largest mass scale is that of the mass of the gauge bosons of the weak interaction, the $W^{\pm}$ and the Z^0, $\approx$ 100 GeV. The standard model is thought to very accurately describe the weak interactions of point-like leptons; electrons, muons, taus, and their neutrinos. The leptons couple to their neutrinos with a universal $V - A$ weak coupling. The decay of a μ^-

$$\mu^- \rightarrow e^- + \bar{\nu}_e + \nu_\mu$$

is typical of this class of decays and interactions. (See figure 1.) A small number of parameters, the Weinberg angle, the gauge boson, lepton, and neutrino masses, the neutrino mixing angles, and α, must be determined experimentally.

For large momentum transfer (> 1 GeV) the weak interactions of quarks, such as dilepton production in $p\bar{p}$ scattering (see figure 2), is calculable using next-to-leading order QCD corrections to standard electroweak theory. The weak interactions of quarks are more complex than those of leptons. Linear combinations of quark fields, rather than the quark fields themselves, couple to the weak gauge bosons. In contrast to the lepton flavor, quark flavor is not conserved. In addition to the quark masses, the quark mixing angles (CKM matrix elements) must be determined from experiment.

The mass scale of bound systems of quarks such as nucleons and mesons is less than the QCD mass scale of $\Lambda \approx 1$ GeV. The simplest weak interactions of hadrons are their semi-leptonic decays. An example is neutron beta decay,

$$n \rightarrow p + e^- + \bar{\nu}_e.$$

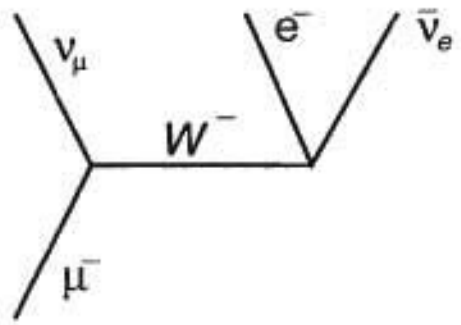

Figure 1: Decay of the μ^- through the leptonic weak interaction.

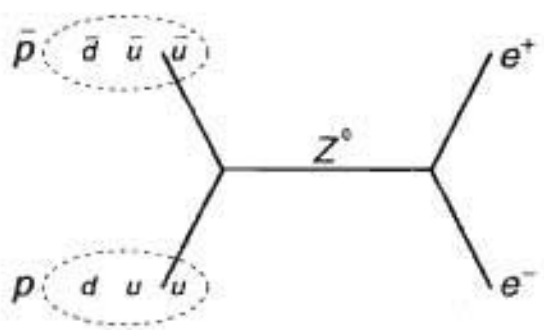

Figure 2: Dilepton production in $p\bar{p}$ scattering.

shown in figure 3. The strong interactions of quarks, through gluon exchange, modify semi-leptonic decay rates from the values that would be expected in their absence. For example, the magnitude of the axial vector coupling constant G_A in neutron beta decay is 30% larger than the vector coupling constant G_V.

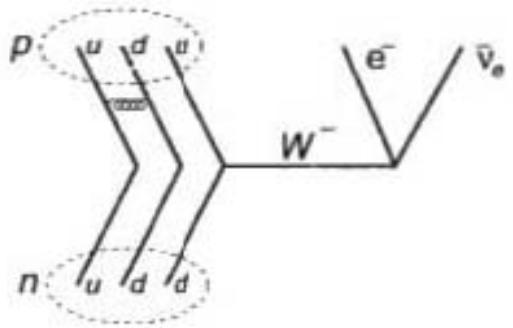

Figure 3: Decay of the neutron through the semi-leptonic weak interaction.

Just like purely leptonic and semi-leptonic weak interactions, purely hadronic weak interaction between nucleons can be mediated by the exchange of the $W^{\pm}$ and Z^0 bosons. At momentum transfers typical of nucleon-nucleon or nuclear interactions, ≈ 300 MeV, the appropriate degrees of freedom are meson and nucleons. The range of the $W^{\pm}$ and Z^0 is ≈ 0.02 fm, much shorter than the distance between nucleons. The hard-core repulsion in the NN interaction keeps the nucleons much farther apart than the range of the weak gauge bosons. The long-range weak force between nucleons is mediated by the exchange of light mesons. As shown in figure 4, a weak gauge boson, is emitted by a quark, travels a short distance, and changes into a π, ρ, or ω, which then couples strongly to another nucleon. As in the case of semi-leptonic decays, the coupling strengths are modified by strong interactions of the bound quarks.

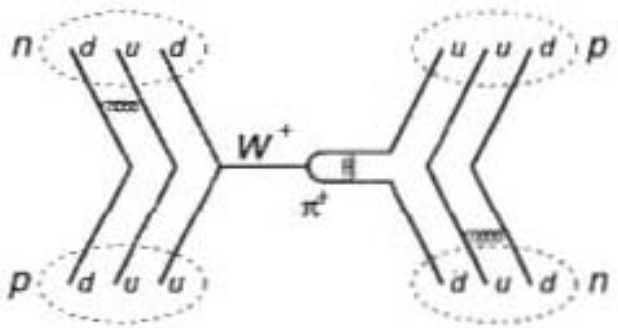

Figure 4: Neutron-proton scattering, mediated by the hadronic weak interaction.

The above description of parity-violating phenomena in nuclei has taken as its starting point the weak meson-exchange potential model described by figure 5. The degrees of freedom are nucleons and mesons. The exchanged weak gauge boson has been collapsed into a weak meson-nucleon vertex. The weak interaction can change isospin and therefore isospin is not conserved at the weak vertex. The other vertex describes the the strong interaction of mesons and nucleons and the couplings are known experimentally. Because QCD has not been solved for bound systems, the weak meson-nucleon couplings $H_\mu^{\Delta I}$ must be determined from experiment. The weak meson-exchange potential V_{pnc} has the form

$$V_{pnc} = \sum_{\mu=\pi,\rho,\omega} \sum_{\Delta I=0,1,2} H_\mu^{\Delta I} V_\mu^{\Delta I} \tag{1}$$

where V_{pnc} is a linear combination of terms each involving the exchange of a π, ρ, or ω meson with a second index describing the isospin exchanged in the weak interaction. For example the $\Delta I = 1$ pion potential has the following form:

$$V_\pi^1 = \frac{i}{m} [\vec{\tau}_1 \times \vec{\tau}_2]_z (\vec{\sigma}_1 + \vec{\sigma}_2) \cdot \vec{u}_\pi(\vec{r}), \tag{2}$$

where m is the nucleon mass,

$$\vec{u}_\pi(\vec{r}) = \left[\vec{p}, \frac{e^{-m_\pi r}}{4\pi r}\right], \tag{3}$$

m_π is the pion mass, $\vec{r} = \vec{r}_1 - \vec{r}_2$, and $\vec{p} = \vec{p}_1 - \vec{p}_2$. The Yukawa function in $\vec{u}_\pi(\vec{r})$ (and the weak potentials for the other mesons) gives the dependence of V_π^1 on the separation of the two interacting nucleons. The range of V_π^1 is longer than that of the other weak meson potentials.

The parity-violating nucleon-nucleon interaction is much weaker than the strong nucleon-nucleon interaction. Theories of parity violating phenomena in nuclei start with solutions of the strong, parity-conserving, nuclear Hamiltonian ψ and admix parity-odd components ϕ treating the two-body weak meson-exchange potential as a perturbation.

$$\psi' = \psi + \frac{\langle\phi|V_{pnc}|\psi\rangle}{\Delta E}\phi. \tag{4}$$

An observable such as a nuclear anapole moment a can be expressed as a matrix element of the corresponding operator:

$$a = \frac{\pi e \mu}{m} \langle\psi'|\vec{r} \times \vec{\sigma}|\psi'\rangle, \tag{5}$$

where e is the quantum of charge and μ is the magnetic moment of the unpaired nucleon. If the observable involves a transition between states, the initial and final states would be different. It is evident that each parity-violating observable is given by a linear combination of the weak meson-nucleon couplings times matrix elements of operators between nuclear states. For the two-body system the wave functions are known, the matrix elements can be reliably calculated, and the relationship between observables and the couplings is unambiguous. For more than a few bodies the nuclear wave functions can not be exactly calculated and the expressions for parity-violating observables are uncertain for two reasons: the couplings are not known and the nuclear matrix elements can not be reliably calculated.

The strategy of the present proposal is to overcome the problem of imperfect knowledge of the nuclear wave function by experimentally determining a parity-violating observable in the two-body system. We propose to measure the directional asymmetry of the direction of emission of the γ-ray

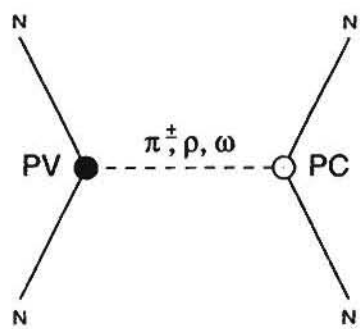

Figure 5: Meson-exchange model of the hadronic weak interaction.

when a polarized neutron is captured on a proton, $\vec{n}+p \rightarrow d+\gamma$. We show below that this observable is uniquely related to the longest range and most important of the weak meson-nucleon couplings, H_π^1. The bulk of the proposal describes an experiment that will determine H_π^1 with a statistical accuracy of 10% of its expected value and with systematic errors much less than statistical errors.

The remainder of the introduction is organized as follows. We briefly discuss what is known experimentally about H_π^1 and other weak meson-nucleon couplings. We outline a strategy of how to experimentally determine the weak meson-nucleon couplings in two-body systems. Indeed enough two-body experiments are either underway or possible to over-constrain the weak meson-exchange couplings and test the applicability of the weak meson-exchange potential to the description of parity-violating phenomena in nuclei. Once the weak meson-exchange potential is determined and established, it can be used as the starting point for the description of parity-violating phenomena in $A > 3$ nuclei. We next discuss theories that seek to relate H_π^1 to the next higher mass scale. These theories seek to describe or predict the values of the weak meson-exchange couplings starting from a pictures of mesons and nucleons as made up of quarks and interaction through the exchange of gluons, QCD. We conclude the introduction by discussing the expression for the directional asymmetry in $\vec{n} + p \rightarrow d + \gamma$ in terms of the weak couplings.

1.2 Status of Our Knowledge of the Weak Meson-Nucleon Couplings

1.2.1 Theoretical Estimates of the Sizes of the Weak Meson-Exchange Couplings

The order of magnitude of the weak NN couplings (5×10^{-7}) can be estimated on dimensional grounds as the product of the average momentum of nucleons in the nucleus (0.2 GeV/c) and the weak coupling ($G_F/(\hbar c)^3 = 1.16 \times 10^{-5}$ GeV^{-2}). The most systematic theoretical analysis of this approach to describing the weak NN interaction is given in a review by Desplanques, Donoghue, and Holstein (DDH) [8]. These authors used the non-relativistic quark model, PCAC, weak SU(6) symmetry, current algebra, and strong SU(3) symmetry to relate known $\Delta S = 1$ hyperon decay amplitudes to the weak meson-nucleon-nucleon couplings. There are considerable model dependencies in these estimates arising from the difficulties in treating strong interaction effects. These authors produced "best" estimates and "reasonable ranges" for the couplings, given in table 1. Desplanques

has recently revised the "reasonable range" for H_π^1 [9]. DDH considered exchanges of the three lightest mesons, π, ρ, and ω. There are seven possible couplings that are labeled according to the meson exchanged and the isospin exchanged ΔI at the vertex. Adelberger and Haxton [1] give expressions for parity-violating observables in their review.

Exchanged Meson	Coupling	ΔI	"Best Value" (10^{-6})	"Reasonable Range" (10^{-6})
π	H_π^1	1	1.08	0.0–2.71
ρ	H_ρ^0	0	1.59	−1.59–4.29
ρ	H_ρ^1	1	0.03	0.0–0.053
ρ	H_ρ^2	2	1.33	−1.06–1.54
ρ	H'^1_ρ	1	0.00	none
ω	H_ω^0	0	0.80	−2.39–4.29
ω	H_ω^1	1	0.48	0.32–0.80

Table 1: Estimated weak meson-nucleon couplings from ref. [1].

It is evident that if the couplings H_ρ^1 and H'^1_ρ satisfy the bounds given in table 1, they will play a negligible role in determining the outcomes of experiments. In what follows we concentrate on the remaining 5 couplings.

1.2.2 What We Know from Experiments

Experiments in the *pp* System An extensive program of high-quality experiments has been carried out to measure the parity-violating longitudinal asymmetry A_z in the scattering of polarized protons from unpolarized protons at 15 and 45 MeV. These experiments show the predicted energy dependence of the longitudinal asymmetry. The experiments determine a linear combination of weak couplings, for example at 45 MeV A_z is given by

$$A_z = -0.053\left(H_\rho^0 + H_\rho^2/\sqrt{6}\right) - 0.016\left(H_\omega^0 + H_\omega^1\right), \tag{6}$$

to an accuracy of 10%.

Experiments in the *np* System Measurements have been made in *np* capture of both the directional asymmetry A_γ and circular polarization P_γ of the emitted γ-rays. Both experiments were statistically limited, and yielded null results. In the first case, Caviagnac, *et al.* [10] report a value of $A_\gamma = 0.6 \pm 2.1 \times 10^{-7}$, which gives for the $\Delta I = 1$ weak pion coupling $H_\pi^1 = -1.3 \pm 4.7 \times 10^{-6}$ (see equation 20). In the second case, Knyaz'kov, *et al.* [11] report a value of $P_\gamma = 1.8 \pm 1.8 \times 10^{-7}$, which gives for the combination of the $\Delta I = 0$ and 2 weak rho couplings $H_\rho^0 + 2H_\rho^2/\sqrt{6} = 8.2 \pm 8.2 \times 10^{-6}$ (see equation 12). The inverse reaction, deuteron photo-disintegration by circularly polarized γ-rays, has been measured by Earle, *et al.* [12], who also report a null result. These experimental limits are less stringent than the "reasonable ranges" given in table 1. Clearly, experiments with improved statistical precision are required.

Measurement of P_γ from ^{18}F and its Interpretation The determination of the weak meson-nucleon exchange couplings from experimental measurements in nuclei are discussed in the review by Adelberger and Haxton[1]. There are substantial uncertainties in interpreting most experiments in nuclei because one cannot make reliable *ab initio* calculations of the amplitudes of the weak meson-nucleon exchange potential operators. The circular polarization P_γ of the 1081 keV transition in ^{18}F is an exception to this unfortunate situation because the matrix elements needed to extract a value for H_π^1 from experiments can be measured. The circular polarization of a $\Delta I = 1$ parity forbidden gamma transition in ^{18}F has been measured in five different and internally consistent experiments (references given in [1]). To a good approximation the circular polarization is due to the parity-violating mixing between the $J = 0$, $I = 0$ parity-odd level ($|-\rangle$) in ^{18}F and the nearly degenerate $J = 0$, even-parity, $I = 1$ level ($|+\rangle$). The circular polarization is given by:

$$P_\gamma = \frac{2}{\Delta E} \frac{\langle +|V_{pnc}|-\rangle \langle gs|M1|+\rangle}{\langle gs|E1|-\rangle}. \tag{7}$$

The magnitudes of the $M1$ and $E1$ transition amplitudes and the energy splitting $\Delta E = 39$ keV between the levels are known experimentally. Bennet, Lowry, and Krien [13] and Haxton [14] pointed out that the unknown amplitude, $\langle +|V_{pnc}|-\rangle$, could be related to the lifetime of the first forbidden beta decay between isobaric analog states of $|+\rangle$ and $|-\rangle$ in ^{18}Ne. For beta transitions between opposite parity $J = 0$ levels, spin and parity selection rules exclude all but two of the six possible transition amplitudes. One of these vanishes in the long wavelength limit leaving only the M_{00}^5 amplitude. Haxton uses PCAC, current algebra, and the approximation that the neutron and proton densities are the same for the $A = 18$ system to argue that the two-body part of M_{00}^5 renormalizes the one-body part and that the operator for the weak nucleon-nucleon potential due to pion exchange is to within a known constant an isospin rotation of the operator for M_{00}^5. Haxton estimates the contributions of heavy mesons as a 5% correction to the pion term. Since the experimental value of the asymmetry, $P_\gamma = 8 \pm 39 \times 10^{-5}$, is consistent with zero, an upper limit for H_π^1 results. Adelberger and Haxton find $H_\pi^1 < 0.35 \times 10^{-6}$. This value is a fraction of the DDH "best" value and is an order of magnitude smaller than the "reasonable range". This result has been interpreted as evidence for (unexpected) suppression of quark-quark neutral currents. Haxton's arguments, outlined above, appear sound. The comparison of H_π^1 from ^{18}F and H_π^1 from $\vec{n} + p \to d + \gamma$ will test the applicability of the weak meson-exchange potential to weak phenomena in $A > 3$ nuclei.

Measurements of the Anapole Moments ^{133}Cs and ^{205}Tl and their Interpretation Recently, the anapole moments of nuclear ground states have been observed using laser spectroscopy on atomic beams. These measurements have observed, for the first time, a static moment of a nucleus that is forbidden by parity. Although in its infancy, the experimental study of nuclear anapole moments is potentially important to the understanding of the weak interaction in nuclei because nuclear anapole moments can be measured in many nuclei and their systematic behavior established. Knowledge of systematics can then be used to check the correctness of the models used to determine the nuclear wave functions.

The anapole moment operator [15] is a parity-odd rank one tensor and is given by

$$\vec{a} = -\pi \int r^2 \vec{j}(r)\, d^3r, \tag{8}$$

where $\vec{j}(r)$ is the electromagnetic current density operator. The anapole moment has an expectation

value of zero for states of definite parity. The size of the anapole moment is given by the dimensionless constant κ_a, whose value is thought to be theoretically stable for three reasons:

1. The anapole moment of a nuclear state is a diagonal matrix element, in contrast to a transition matrix element.

2. The nuclear wave function can be constrained by the measured magnetic moment of the state. The single-particle estimate is $\mu_{sp} = 1.72$ for ^{133}Cs and $\mu_{sp} = 2.79$ for ^{205}Tl (see, for example, [16]). By comparison, the experimental values are $\mu_{exp} = 2.58$ and $\mu_{exp} = 1.64$, respectively. The rough agreement between the single-particle estimates and experimental values of the magnetic moments justifies the theoretical approach to anapole moments of starting from single-particle estimates and then adding many-body effects as corrections. Information on the spatial distribution of the electromagnetic current can be obtained from the magnetic hyperfine anomaly. This information can be used to constrain the wave function.

3. The contribution to anapole moment of the spin of the odd proton (neutron) can be estimated analytically and gives results close to those from full many-body calculations[1] [17].

The estimate of the one-body part of the anapole moment is similar to the calculation of the contribution of the spin of the unpaired nucleon to the magnetic moment of a nucleus. The analytical estimate [18] gives a value in rough agreement with detailed nuclear structure calculations by Haxton [19], Haxton, Henley, and Musolf [20], Flambaum and Murray [21], and Dmitriev and Telitsin [17]. The latter is the most recent calculation and includes the effects of spin, spin-orbit, convection, and contact currents, many-body corrections, and RPA re-normalization of the weak interaction addition to the single-particle weak interaction.

The non-zero measurement of the anapole moment of ^{133}Cs [22] has been analyzed by Flambaum and Murray [21] to extract a value for H_π^1. Their result, $H_\pi^1 = 2.26 \pm 0.50(\text{expt}) \pm 0.83(\text{theor}) \times 10^{-6}$ is a factor of two larger than the DDH value and a factor of *seven* larger than the upper limit set by the ^{18}F experiments. Their analysis, however, is controversial for two reasons [23]. First, the ^{133}Cs anapole moment is almost as sensitive to H_ρ^1 as to H_π^1. Wilburn and Bowman find

$$\kappa_a \approx 1.05 \times 10^5 \left(H_\pi^1 + 0.69 H_\rho^0\right). \tag{9}$$

Because of this sensitivity, and because of the lack of model-independent constraints on H_ρ^0, it is possible to extract values of the two couplings that agree with both experiments. Secondly, the result from ^{133}Cs are inconsistent with an earlier null measurement of the anapole moment of ^{205}Tl [24]. The situation is summarized in figure 6. This result suggests that nuclear structure effects that are not included in the theory may be important in interpreting the measurements, assuming both measurements are correct.

The present controversy concerning the interpretation of measured nuclear anapole moments highlights the need to determine the weak couplings from experiments in few-nucleon systems whose interpretation is free from uncertainties in nuclear structure and demonstrates the nuclear physics that can be learned. If the weak meson-nucleon couplings were known, the present controversy could be more definitively addressed. One would calculate the values of the anapole moments using the measured values of the couplings from few-nucleon experiments; if the measured values of the anapole moments disagreed with these predictions, the problem would lie with the measurements, the nuclear theory, or the applicability of the meson-exchange model to nuclei.

[1] Dmitriev and Telitsin find that a naive harmonic oscillator model gives results that agree with their full calculation to within 10%.

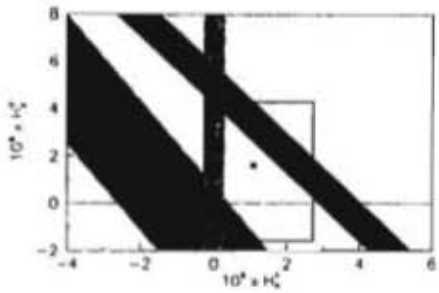

Figure 6: Weak coupling constants H^1_π and H^0_ρ extracted from the ^{18}F (light band), ^{205}Tl (medium band), and ^{133}Cs (dark band) experiments. Also shown are the DDH "best" values (square) and "reasonable range" (box).

1.3 Strategy to Determine the Couplings from Two-Nucleon Experiments

The purpose of the present proposal is to determine the most important coupling, H^1_π. This determination of H^1_π, free from any uncertainties arising from nuclear structure, will be the cornerstone of any effort to determine a complete set of couplings. In the expressions for most experimental observables, H^1_π occurs in combination with others. It is therefore highly desirable to develop an experimental program to determine the other couplings.

As discussed in section 1.2.2, the PSI measurement of A_z in pp scattering at 45 MeV is given by a linear combination of H^0_ρ, H^2_ρ, H^0_ω, and H^1_ω:

$$A_z = -0.053\left(H^0_\rho + H^2_\rho/\sqrt{6}\right) - 0.016\left(H^0_\omega + H^1_\omega\right). \tag{10}$$

An experiment in progress at TRIUMF [25] to measure A_z at 221 MeV is sensitive to only the ρ couplings:

$$A_z = 0.028\left(H^0_\rho + H^2_\rho/\sqrt{6}\right). \tag{11}$$

The low energy pp experiment and the TRIUMF experiment will determine the linear combination of ω couplings $H^0_\omega + H^1_\omega$ and the linear combination of ρ couplings $H^0_\rho + H^2_\rho/\sqrt{6}$. One further experiment is necessary to separate the two ρ couplings.

The problem of separately determining the weak ρ couplings could be resolved by measuring the circular polarization P_γ of the gammas emitted in the $\vec{n} + p \rightarrow d + \gamma$ reaction. This observable is primarily sensitive to the $\Delta I = 0$ and 2 ρ couplings [1]:

$$P_\gamma = 0.022H^0_\rho + 0.043H^2_\rho/\sqrt{6} - 0.002H^0_\omega. \tag{12}$$

The combination of this measurement and the TRIUMF pp measurement would then independently determine H^0_ρ and H^2_ρ. In practice, it is experimentally easier to measure the inverse reaction, the directional asymmetry in the photo-disintegration of the deuteron by circularly polarized photons, due to the low efficiency of γ-ray polarization analyzers. As in the case of A_γ, existing measurements

of P_γ (or of the inverse reaction) [26, 11, 12] are not of sufficient precision to accomplish this task. With the availability of very intense gamma beams from Compton back-scattering using free electron lasers [27], a more precise measurement of the deuteron photo-disintegration asymmetry is possible and should be pursued.

Finally, there is another observable in the np system that is primarily sensitive to H_π^1: the parity-violating spin rotation of transversely polarized neutrons in a liquid para-hydrogen target. There is a theoretical calculation for the low-energy neutron spin rotation angle ϕ_{PNC} per unit length in para-hydrogen [28]

$$\phi_{PNC} = -1.31H_\pi^1 - 0.23H_\rho^0 - 0.25H_\rho^2 - 0.23H_\omega^0, \tag{13}$$

in units of radians per meter, which implies that this observable is also primarily sensitive to H_π^1. An experimental sensitivity of about 2×10^{-4} radians per meter would be required to see this effect for the DDH value of H_π^1. The sensitivity goal for a similar experiment in progress to search for parity violating neutron spin rotation in helium is 1×10^{-7} radians per meter [29]. An experiment to measure the longitudinal asymmetry A_z in np scattering at neutron energies of tens of MeV is also possible. This observable is sensitive to H_π^1 and other couplings. A theoretical calculation of this observable is in progress [30]. With the addition of these two experiments, we begin to be able to over constrain the weak couplings and test the internal consistency of the meson exchange picture of the weak NN interaction.

1.4 Calculations of H_π^1

The estimate of H_π^1 from the quark model and weak SU(6) symmetry have been discussed above. The revised estimate of the "reasonable range" by Desplanques is: $0 < H_\pi^1 < 0.6 \times 10^{-6}$ down from $0 < H_\pi^1 < 1.1 \times 10^{-6}$ by Desplanques, Donoghue, and Holstein. Recently, Henley, Hwang, and Kislinger [31] have carried out QCD sum rule calculations of H_π^1. These calculations include the effects of gluon exchange that are absent in earlier quark model calculations. Henley *et al.* make the approximation that there are no strange quarks in the nucleon or charged pion. There are therefore no contributions to H_π^1 from $W^\pm$ exchange [32]. In any case, the contributions of charged currents would be Cabbibo suppressed if strange quarks were included. The calculation of Henley *et al.* adds Z^0 exchange to the diagrams involved in the strong interaction of the pion and the nucleon. Non-perturbative effects are described by the polarizability of a pion condensate in both the calculation of the strong pion-nucleon-nucleon coupling, $g_{\pi NN}$, and the weak meson-nucleon-nucleon coupling, H_π^1. Henley *et al.* fit the polarizability of the pion condensate to the experimental value of $g_{\pi NN}$. This procedure leads to a prediction of a small value of $H_\pi^1 = 0.5 \times 10^{-7}$, about half the error expected from the proposed measurement.

Kaplan and Savage present a contrary view concerning the role of strangeness [33]. They estimate H_π^1 and other parity-violating couplings in the framework of pion chiral perturbation theory. They explicitly consider the strange and anti-strange sea quark component of the nucleon wave function. Kaplan and Savage estimate that the contribution of strange components of the nucleon to H_π^1 may be as large as 1.4×10^{-6}. They argue multi-pion exchange may invalidate the conclusion that the ^{18}F experiment can be interpreted as a measurement of H_π^1. Kaplan and Savage give a large theoretical uncertainty in these estimates. The quark model and QCD calculations favor small values of H_π^1. The chiral perturbation theory estimates suggest the possibility that H_π^1 may be large due to strangeness, but the uncertainty in these estimates is large. An experiment that provides a statistically accurate value of H_π^1 with small systematic and theoretical errors will challenge theories

that attempt to evaluate H_π^1 and will stimulate work in the calculation of the modification of weak interactions between quarks in the non-perturbative regime.

1.5 Symmetry Considerations for $\vec{n} + p \to d + \gamma$

It is worth understanding the reasons why the parity-violating gamma asymmetry, A_γ, in the reaction $\vec{n}+p \to d+\gamma$ is primarily sensitive to only the $\Delta I = 1$ component of the weak interaction. First of all, due to the large size of the deuteron only the longest-range components of the NN interaction (due to π and ρ exchange) are important in this reaction. From the non-relativistic weak NN potential, weak π exchange is $\Delta I = 1$ and weak ρ exchange is mainly $\Delta I = 0$ and $\Delta I = 2$.

Now consider the possible electromagnetic transitions in the $\vec{n} + p \to d + \gamma$ reaction. For low-energy neutrons, we will consider only $L = 0$ and $L = 1$ capture and reaction channels. Without parity violation, the channels for the initial state are $\left|{}^1S_0, I = 1\right\rangle_i$ and $\left|{}^3S_1, I = 0\right\rangle_i$ and the final state channel for the $(J^\pi, I) = (1^+, 0)$ deuteron is $\left|{}^3S_1, I = 0\right\rangle_D$ (ignoring the small tensor component in the deuteron). The weak interaction mixes in the following $L = 1$ components to the singlet and triplet S-waves in both the initial and final states:

$$\left|{}^1S_0, I = 1\right\rangle_i \longrightarrow \left|{}^1S_0, I = 1\right\rangle_i + f_0 \left|{}^3P_0, I = 1\right\rangle_i, \tag{14}$$

$$\left|{}^3S_1, I = 0\right\rangle_i \longrightarrow \left|{}^3S_1, I = 0\right\rangle_i + g_0 \left|{}^1P_1, I = 0\right\rangle_i + g_1 \left|{}^3P_1, I = 1\right\rangle_i, \tag{15}$$

$$\left|{}^3S_1, I = 0\right\rangle_D \longrightarrow \left|{}^3S_1, I = 0\right\rangle_D + h_0 \left|{}^1P_1, I = 0\right\rangle_D + h_1 \left|{}^3P_1, I = 1\right\rangle_D, \tag{16}$$

where the f_I, g_I and h_I terms are the amplitudes of the small weak interaction-induced admixtures with isospin change I. If one now writes down the matrix elements of the electromagnetic interaction, keeping only the lowest order multipoles consistent with parity conservation in the electromagnetic interaction and with isospin selection rules that forbid $E1$ transitions in self-conjugate nuclei like the deuteron, one obtains the parity conserving term $\langle M1 | \langle {}^3S_1, I = 0 |_D H_{em} | {}^1S_0, I = 1 \rangle$ and the parity violating terms

$$f_0 \langle E1 | \langle {}^3S_1, I = 0 |_D H_{em} | {}^3P_0, I = 1 \rangle, \tag{17}$$

$$g_1 \langle E1 | \langle {}^3S_1, I = 0 |_D H_{em} | {}^3P_1, I = 1 \rangle, \tag{18}$$

$$h_1 \langle E1 | \langle {}^3P_1, I = 1 |_D H_{em} | {}^3S_1, I = 0 \rangle. \tag{19}$$

Finally, since a gamma asymmetry cannot be produced from a $J = 0$ initial state, we are left with only a $\Delta I = 1$ contribution to parity violation in the gamma asymmetry. There are small corrections to this argument from isospin violation, higher-order multipole contributions, relativistic effects etc. but the main result survives a more exact treatment. This result was first obtained by Danilov [34].

There are two calculations of A_γ as a function of the weak couplings. Adelberger and Haxton [1] find:

$$A_\gamma = -0.045 \left(H_\pi^1 - 0.02 H_\rho^1 + 0.02 H_\omega^1 + 0.04 H'^1_\rho \right). \tag{20}$$

The contributions of the non-pion couplings are estimated by taking the DDH upper limits $H_\rho^1 = 5 \times 10^{-8}$ and $H_\omega^1 = 8 \times 10^{-7}$. Desplanques and Missimer, who use H_π^1 and weak nucleon-nucleon amplitudes X to parameterize the weak nucleon-nucleon interaction [35], find:

$$A_\gamma = -0.045 \left(H_\pi^1 + 0.11 X_{pn}^+ - 0.11 X_{pn}^- \right). \tag{21}$$

The X's are linear combinations of the $\Delta I = 1$ meson exchange couplings other than H_π^1. These calculations of A_γ agree on the coefficient of H_π^1 and both find the contributions from other mesons to be small. An accurate measurement of A_γ is therefore an accurate measurement of H_π^1.

1.6 Role of the hadronic weak interaction in the study of the weak interaction

The study of parity violation in nuclei has played an important role in the development of our understanding of the weak interaction. The current-current hypothesis for the form of the weak interaction implies that parity admixture in nuclear wave functions would be first order in the Fermi coupling G_F, while the four-Fermion form of the weak interaction implies second-order admixtures. The observation of circular polarization in a gamma transition in ^{181}Ta, $P_\gamma \sim 10^{-7}$, by Lobashov, *et al.* [36, 37] gave strong support to the current-current hypothesis.

1.7 Search for New Weak Neutral Gauge Bosons

As the search for weak neutral currents was being pursued, it was recognized that the hadronic weak interaction might be a good place to search for and study weak neutral currents. In contrast to charged currents the contributions of weak neutral currents to the $\Delta I = 1$ hadronic weak interaction are not Cabibbo suppressed. The $\Delta I = 1$ pion coupling might be strongly influenced by weak neutral currents, in the language of the standard model Z^0 exchange. As discussed above, the qqZ^0 has been measured in large momentum transfer experiments. The existence of the qqZ^0 coupling implies the existence of a weak neutral current contribution to the weak nucleon-nucleon interaction, according to figure 3. The standard model is widely believed to be incomplete. If in addition to the Z^0 of the standard model, there exist other gauge bosons that couple to quarks and do not decay into leptons, these additional Z^0's would also contribute to H_π^1, but would not be observed in other processes. The role of the hadronic weak interaction as a direct probe of weak neutral currents is emphasized by Adelberger and Haxton [1]. However, we note that, the bound QCD problem has not yet been solved and there is considerable uncertainties in calculations of H_π^1 from the weak neutral current of the standard model. Until such calculations are possible only very large effects of additional Z^0's will be detectable in H_π^1.

1.8 Summary

The experiment to measure the directional asymmetry of gammas A_γ in $\vec{n} + p \rightarrow d + \gamma$ and extract a value of H_π^1 is of great interest for the following reasons:

1. We will show in section 3 that the experiment will measure the asymmetry with a statistical error of 0.5×10^{-8} and a negligible systematic error. A measurement of A_γ to this precision allows interesting conclusions to be drawn concerning H_π^1.

2. There is no nuclear structure uncertainty in the relationship between H_π^1 and the asymmetry. The uncertainty in the extracted value of H_π^1 will be small, 10% of the DDH theoretical estimate, given in table 1. There will be no uncertainties due to experimental systematic errors or nuclear structure. To a good approximation the asymmetry depends only on H_π^1.

3. An unambiguous value for H_π^1 will test theories of the weak interaction of hadrons in the non-perturbative regime and stimulate theoretical work in this area.

4. An unambiguous measurement will settle any controversy raised by the ^{133}Cs anapole moment and ^{18}F circular polarization results and their interpretation. The comparison of H_π^1 from $\vec{n} + p \rightarrow d + \gamma$ and H_π^1 from ^{18}F will test the applicability of the meson-exchange potential to $A > 3$ systems.

5. The determination of H_π^1 is the cornerstone of a feasible and partially complete program to over-constrain the weak NN couplings from parity-violating phenomena in the exactly calculable two-nucleon system.

6. The study of parity violation in the nucleon-nucleon interactions remains the only experimental means to directly study the weak neutral current interaction between quarks.

2 Advantages of LANSCE

LANSCE is uniquely suited as a site for this measurement. LANSCE has the only intense pulsed neutron source available for nuclear physics research and Los Alamos has a scientific staff that is unusually well qualified for this experiment.

When the upgrades currently in progress are complete, the Lujan Center spallation source will be the highest flux pulsed source in the world, equaling ISIS in average flux and exceeding it in peak flux. As noted throughout this proposal, there are compelling reasons for carrying out this experiment at a pulsed neutron source. Specific examples include:

- the pulsed nature of the beam provides neutron time-of-flight information, allowing determination of the neutron energy,
- systematic effects can be studied by their differing time-of-flight behaviors,
- the pulsed beam allows the use of a resonant RF spin flipper, eliminating the $\vec{\mu} \cdot \nabla B$ force on the neutrons,
- the ratio of gammas to neutrons is lower than at a reactor, and
- the prompt gamma background is separated in time from the neutrons of interest.

Not only does LANSCE provide the most intense such source, it is the only intense pulsed neutron facility at which proposals for nuclear physics experiments are entertained.

The Los Alamos staff associated with this effort is uniquely qualified to carry out the proposed work. The principal investigator, David Bowman is a world expert in precise parity violation experiments. He has measured parity violation in the nucleon-nucleon system as well as in neutron resonances with pulsed neutrons. Steve Lamoreaux and Geoff Greene have between them more than three decades of experience in a wide variety of precise measurements with cold neutrons. Seppo Penttilä has extensive experience in measurements of fundamental symmetries and is a world expert in cryogenic techniques for nuclear physics experiments. Scott Wilburn has participated in precise parity violation experiments using charged particles. Vincent Yuan has extensive experience with pulsed neutron experiments. In addition, as can be seen in appendix C, the rest of the collaboration is extremely experienced in studies of fundamental symmetries with low-energy neutrons.

3 Description of the Proposed Experiment

In this section we describe the conceptual design for the proposed measurement of A_γ in $\vec{n}+p \rightarrow d+\gamma$. The apparatus, shown schematically in figure 7, consists of a cold neutron source, followed by a neutron polarizer, and a liquid para-hydrogen target, surrounded by an array of gamma detectors. Neutrons from the spallation source are moderated by a liquid hydrogen moderator. The source is pulsed, thus allowing measurement of neutron energy through time-of-flight techniques. The neutron guide transports the neutrons from the moderator through the biological shield with high efficiency. The neutrons are then polarized in the vertical direction by transmission through polarized ^{3}He gas. The neutron spin direction can be subsequently reversed by the radio-frequency resonance spin flipper. The use of this type of a spin flipper is possible at a pulsed neutron source, as described in section 3.3. The use of this spin flipper reduces the systematic error associated with the $\vec{\mu}_n \cdot \nabla B$ force, where $\vec{\mu}_n$ is the neutron magnetic moment. The neutrons are captured in the target, which consists of liquid para-hydrogen. This state of hydrogen is required, since neutrons depolarize quickly in ortho-hydrogen, while those with energies below 15 meV retain their polarization in para-hydrogen. Gammas emitted in the capture process are detected in the CsI(Tl) detectors surrounding the target. The parity-violating asymmetry causes an up-down asymmetry in the angular distribution of the gamma-rays for vertical neutron spin. When the neutron spin is reversed, the up-down gamma asymmetry reverses. The parity-violating asymmetry in gamma flux,

$$\frac{d\omega}{d\Omega} = \frac{1}{4\pi}\left(1 + A_\gamma \cos\theta_{n,\gamma}\right), \tag{22}$$

is a measure of H^1_π, as discussed in the introduction.

First we describe the absolutely essential aspect of the experiment, the neutron beam and guide. A question can be raised: are there enough neutrons at LANSCE to measure the asymmetry with a statistical accuracy of 0.5×10^{-8}? We show that during one year of data taking the number of neutrons out of the guide will be $\approx 1.2 \times 10^{18}$. Next, we briefly consider the other essential elements of the experiment: ^{3}He polarizer, spin flipper, para-hydrogen target, and gamma detector. Then we determine the optimal size and configuration of the apparatus by roughly optimizing the statistical accuracy with respect to size, configuration, and cost. We conclude that a statistical accuracy of 0.5×10^{-8} in the gamma asymmetry A_γ is achievable. In the next section we consider the detailed design of the major components of the experiment. We finally discuss systematic errors and conclude that systematic errors can be made small compared to the statistical error. In the evaluation of systematic errors, the pulsed nature of the neutron source and the ability to measure the energy of neutrons that produce gamma-rays plays an essential role in the ability to eliminate some systematic errors completely and to diagnose others by their characteristic behavior with respect to neutron energy.

3.1 Neutron Source and Optimization of the Experimental Configuration

In the Manuel Lujan Jr. Neutron Scattering Center (MLNSC) spallation source intense low-energy neutron pulses are produced by directing 800 MeV proton pulses from the LANSCE accelerator onto a tungsten target at the rate of 20 Hz. After the completion of the accelerator and source upgrade the expected averaged proton beam current will be 200 μA. This proton beam intensity has been used in the neutron flux calculations in this proposal. The spallation target consists of two separate pieces of tungsten operated in a flux-trap geometry [38]. MeV-energy neutrons produced

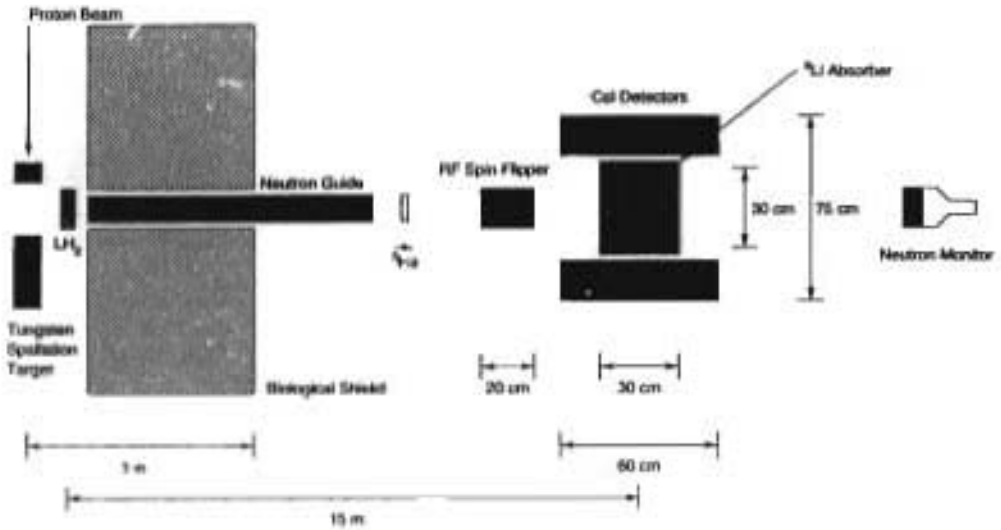

Figure 7: The conceptual design for the proposed experiment, showing the most important elements (not to scale). Approximate sizes and distances are indicated for some features.

in the tungsten are moderated by a partially-coupled liquid hydrogen moderator. The calculated source-moderator performance as a function of neutron energy is shown in figure 8. The spectrum gives the total neutron flux from the 13 cm × 13 cm LH_2 moderator surface. The spectrum consists of a Maxwellian low-energy component and a high-energy tail, which falls as $1/E$. The details of the Maxwellian distribution will depend on the ratio of ortho- to para-hydrogen in the moderator. The flux in figure 8 corresponds to the 50%-ortho, 50%-para case; however, plots of other ratios would not be distinguished from the 50%–50% case for ortho fractions greater than about 20%. The peak of the neutron flux, 6×10^{15} n/(s·sr·eV), is at about 4 meV.

The plan is to mount a 10 cm × 10 cm super-mirror guide that begins 1 m from the moderator and is about 13 m long. We assume that neutrons having a velocity component normal to the surface of the guide less than 15 m/s are totally reflected by the guide. The flux at the exit of the guide with and without the reflectivity of the guide is given in figure 9. The effect of the guide is to increase the flux at low neutron energies. The maximum of the intensity is shifted from 4 meV to 0.75 meV.

The guide improves the sensitivity of the experiment by increasing the flux at low neutron energies where the n–p capture cross section is larger.

The reasons for these improvements can be seen in figure 21, which shows the spin-dependent neutron scattering cross sections for para- and ortho-hydrogen and the capture cross section. Below 15 meV the para-hydrogen cross section is about 20 times smaller than the ortho-hydrogen cross section. The ground state of a para-hydrogen molecule has the two hydrogen spins anti-parallel and has $J^\pi = 0^+$. The rotational ground state of the ortho-hydrogen molecule has $J^\pi = 1^-$. The cross section on para hydrogen is small below 15 meV because the neutron does not have enough energy to

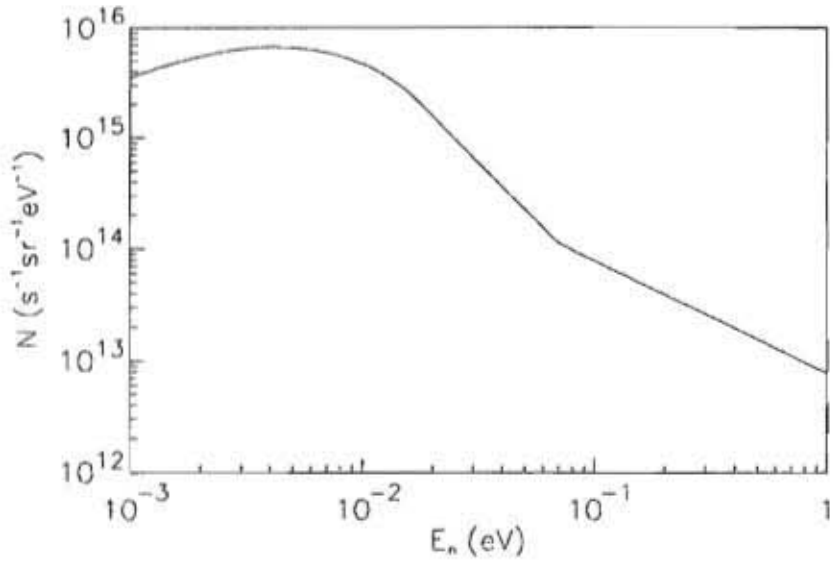

Figure 8: Neutron flux of the nuclear physics beam line at MLNSC. This is the total neutron flux out of the 13 cm × 13 cm liquid hydrogen moderator surface with an average proton current of 200 μA.

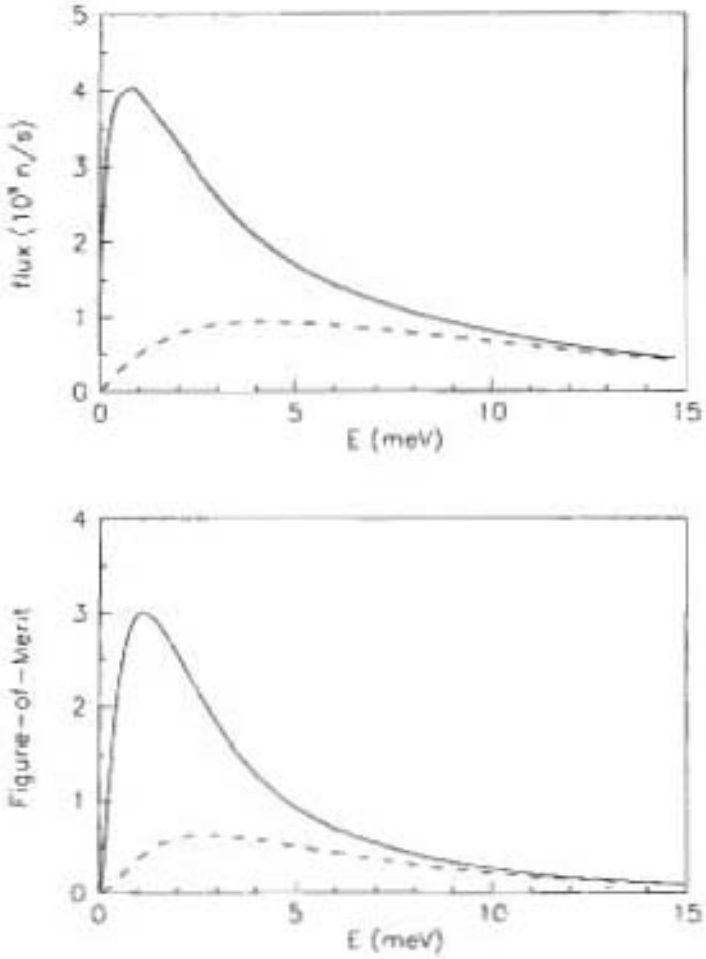

Figure 9: Neutron flux at the target (top) and figure-of-merit (bottom) with (solid) and without (dashed) a 10 cm × 10 cm neutron guide.

excite its first rotational state (45 meV) or to make a spin flip (15 meV). The small size of the cross section follows from the small singlet, non-spin-flip, scattering amplitudes from the two protons, which add coherently and the large triplet, spin-flip, scattering amplitudes which add destructively. Below 15 meV the neutron scatters elastically from the spin-zero para-hydrogen molecules and the neutron does not depolarize. Above 15 meV the neutron can excite spin-flip transitions and the cross section increases rapidly, approaching the ortho-hydrogen cross section. The neutron will rapidly depolarize as it propagates through para hydrogen. Neutrons of any energy can experience spin-flip transitions in scattering from ortho-hydrogen and therefore the neutron cross section is large at all energies. It is, therefore, essential to carry out the experiment with a para-hydrogen target and with neutron energies below 15 meV.

The neutron polarizer consists of a cell of polarized ^{3}He gas. As described in section 3.2.2 the polarized ^{3}He acts as a spin filter. One neutron spin state is preferentially absorbed by polarized ^{3}He. The transmitted neutrons are polarized parallel to the ^{3}He polarization direction. The cross section for the exothermic capture reaction $n+^3He \rightarrow p + t$ is proportional to $1/v$ leading to high neutron polarizations at low energies and small transmissions. The figure-of-merit ((neutron polarization)^2 × transmission) has a maximum at some neutron energy. The experiment is optimized by matching this energy to the peak of the neutron flux. Figure 10 shows a plot of the error in the asymmetry for 1 year of data-taking versus the thickness of the ^{3}He polarizer. We assume a 65% ^{3}He polarization, the gamma detector configuration described below, and a 30 cm thick and 30 cm in diameter para-hydrogen target.

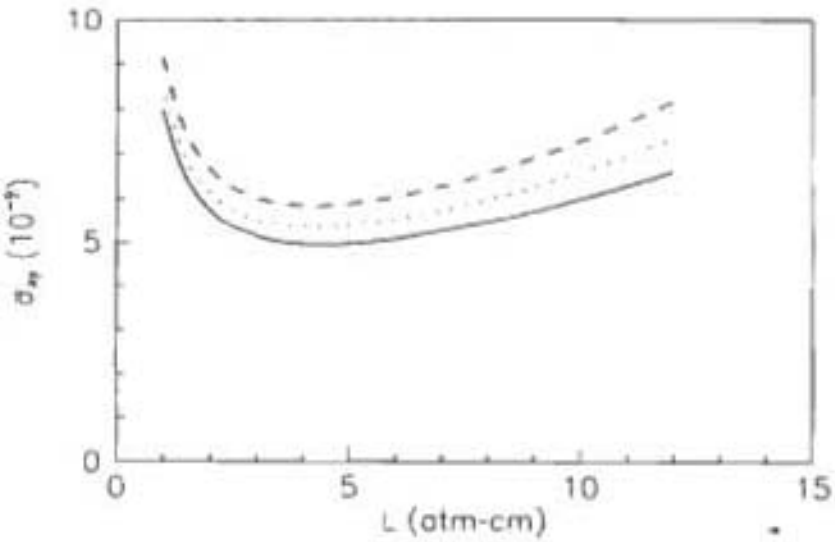

Figure 10: Statistical uncertainty of the experiment as a function of the thickness of the ^{3}He polarizer after one year data taking for ^{3}He polarizations of 55% (dashed), 60% (dotted), and 65% (solid).

The statistical error was calculated by summing the statistical weight over the neutron energy spectrum:

$$W = \frac{T_s}{b} \int dE \frac{d\Phi(E)}{dE} T_n(E) P_n^2(E) c(E) \tag{23}$$

$$\sigma_{A_N} = \frac{1}{\sqrt{W}} \tag{24}$$

Here $T_s = 3.15 \times 10^7$ is the number of seconds in a year, b is a reference statistical efficiency for the gamma detector (see below), dE is the energy bin, $d\Phi(E)/dE$ is the neutron flux per energy at energy E, T_n is the neutron transmission from equation 28, $P_n(E)$ is the neutron polarization from equation 27 and $c(E)$ is the fraction of neutrons that capture in the para-hydrogen target (discussed in section 5.3.1). The error versus ^{3}He thickness has a broad minimum near 4 atm-cm. The broadness of the minimum means that the ^{3}He thickness can be selected suitable for the ^{3}He polarization technique as discussed below and still maintain an error close to the optimum.

The thickness of the CsI detector is set by the mean free path, 5.5 cm, of 2.2 MeV gamma-rays in CsI. A thickness of 15 cm gives 93% absorption. A much thinner detector would have considerable leakage and a large dispersion of the charge deposited. Both of these effects will degrade the figure-of-merit of the detector. Gammas that don't interact don't get counted. The statistical weight above is multiplied by a factor less than unity, $E(Q)^2/E(Q^2) \leq 1$, where Q is the charge created in the detector photocathode. This factor is unity if the gamma energy is completely contained. Gamma-rays of 2.2 MeV have nearly the maximum mean free path. Once a 2.2 MeV gamma interacts the lower energy gammas produced will be efficiently absorbed. We therefore expect a large full-energy peak in the energy, Q, spectrum.

The size of the hydrogen target must cover the beam and contain the neutrons that scatter typically once. The mean free path for capture of a 2 meV neutron is 14 cm. The detailed Monte Carlo calculations described in section 5.3.1 indicate that a 30 cm diameter para-hydrogen target is a reasonable compromise.

The gamma detector must surround the para-hydrogen and detect most of the gammas emitted from the target. How fine grained must the gamma detector be? This question can be answered by considering two limits: an infinitely fine grained detector surrounding a point target and a course detector that detects only whether a gamma ray goes into the upper or lower hemisphere. In the first case $\sigma_{A_N} = \sqrt{3}/\sqrt{N}$ and in the second $\sigma_{A_N} = 2/\sqrt{N}$ where N is the number of gammas detected. From this example we can conclude that position resolution is not a crucial factor in the design of the gamma detector and that large CsI detectors can be used. The $\cos(\theta)$ angular distribution is a slowly varying function of theta and position. So long as the change in $\cos(\theta)$ over a detector element is small, the finite size of the detector elements will not reduce the statistical efficiency of the experiment. We consider the use of cubes of CsI 15 cm on a side. We calculated the coefficient b in $\sigma^2_{A_N} = b/n$ for a detector consisting of n layers of 12 CsI detectors arranged to have a 30 cm by 30 cm hole in each layer as shown in figure 17. We assume a 30 cm long and 30 cm in diameter liquid hydrogen target. We consider both the transverse, b_y, and longitudinal, b_z, spin directions. The results are plotted in figure 11.

From this graph we conclude that the transverse spin orientation produces a smaller error than the longitudinal. The events that give the most information on the asymmetry are those that have the gamma direction along or against the neutron spin. For transverse spin these gamma events are detected, for longitudinal spin they escape. The longitudinal configuration offers some advantages for systematic error because some potential sources of systematic error vanish for the neutron momentum

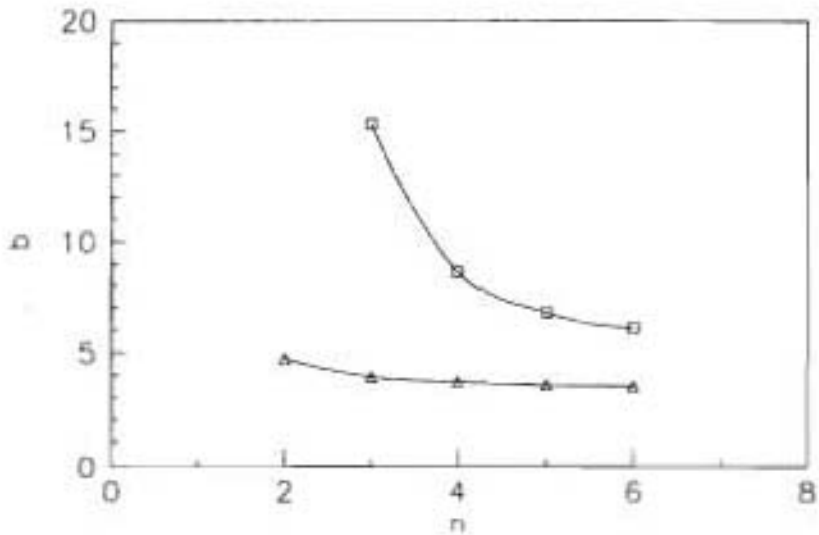

Figure 11: Coefficient b as a function of the number of detector layers. b_x (triangles) corresponds to the case of transverse neutron polarization, b_z (squares) to longitudinal neutron polarization.

along the neutron spin. However the longitudinal configuration has a considerably larger statistical error than the transverse configuration. The error for the transverse configuration doesn't change much after 4 layers and this choice appears appropriate.

3.2 Neutron Polarizer

This experiment requires a neutron polarizer with several unique features:

1. The polarizer should be broad band, providing polarized neutrons of energy up to at least 15 meV, and preferably higher.

2. The polarizer should provide the maximum flux of neutrons (per unit energy) at the detector and therefore transport the neutron beam from the neutron guide to the experiment with maximum efficiency. A cross sectional area of 100 cm^2 is needed to make full use of the 10 cm $\times$ 10 cm beam.

3. The polarizer should optimize the figure-of-merit $P_n^2 T_n$, where P_n is the neutron polarization and T_n is the transmission of the polarizer.

4. The polarizer should produce negligible or easily shielded gamma backgrounds and any residual background should be constant.

5. The polarizer may provide an additional reversal of neutron spin without changing any static (or oscillating) magnetic fields. The importance of this additional spin reversal is discussed in section 4.

Neutron polarization with a polarizing super mirror and with a polarized ^{3}He spin filter should be considered for this experiment. As discussed below, the polarizing super mirror is a well developed technology and a reasonable alternative for this experiment, however there are many advantages to the use of the polarized ^{3}He spin filter that strongly motivate us to implement this technology for this experiment.

3.2.1 Polarizing Super Mirrors

Super mirror polarizers have provided highly polarized cold neutron beams at Grenoble and elsewhere for many years [39], and are also an option for this experiment. A super mirror consists of several leaves stacked across the neutron beam. Each leaf consists of a multi-layer of magnetized cobalt and titanium laid on a gadolinium layer on top of a glass substrate. For very small glancing angles, neutrons of one spin state magnetically scatter from the magnetized Co/Ti multi-layers. The layers of Co and Ti on each leaf have varying thickness to reflect a variety of neutron energies. Neutrons of the other spin state pass through the Co/Ti multi-layer into the gadolinium where they are captured giving off a cascade of gamma rays with energies up to 7 MeV. The leaves themselves are curved from upstream to downstream. As the neutrons reflect along the curved leaves, they are diverted from their initial direction by around 15 mrad. The rate of curvature determines a cutoff neutron energy. If the curvature is too great, neutrons will not be able to follow the leaves through small angle reflections. A smaller curvature allows higher energy neutrons to be transmitted, but the super mirror must be lengthened to insure that there is no line of sight through the device. Typical super mirrors are made with a curvature that transmits neutrons below 9 meV. In principle it would be

possible to raise this cutoff if the leaves are longer and have a smaller curvature. Though larger than most super mirrors, a group at Gatchina believes that they can make a 10 cm × 10 cm super mirror for the proposed experiment that would fill the entire beam.

The transmission of a polarizing super mirror is limited by the curvature of the leaves as mentioned above, and by the range of incident angles reflected by a single leaf. A given leaf typically reflects neutrons with glancing angles less than

$$\theta = \frac{\theta_0}{\sqrt{E}}, \tag{25}$$

where $\theta_0 \approx 860\ \mu\text{rad}\cdot\sqrt{\text{eV}}$. We have modeled the transmission of such a device based on our recent experience at NIST and the anticipated features of the LANSCE nuclear physics beam. The transmission is energy dependent, falling from 25% at the lowest energies to 18% at the cutoff energy, 9 meV. Below the cutoff energy, the polarization of the transmitted beam is greater than 96%. For a super mirror polarizer, we estimate the figure-of-merit, $P_n^2 T_n$, to be 0.18 below 9 meV and close to 0 above 9 meV.

Despite the high figure of merit, super mirrors have drawbacks. The 9 meV cutoff energy affects the statistical accuracy since 25% of the gamma ray yield comes from neutrons above this energy. Neutrons above this energy capture in the mirror, producing a background of 7 MeV gammas, requiring massive shielding for the detectors. In addition, the energy cutoff makes some systematic tests impossible: those that rely on the rapid depolarization in the LH_2 target for neutrons above 15 meV. Also, since a polarizing super mirror is a permanent magnet device, the polarization direction of the beam can only be reversed by changing the direction of the saturation field, which can affect the detector gains. By contrast, the spin of ^{3}He can be quickly reversed with respect to static magnetic fields, and a ^{3}He spin filter has no transmission cutoff for neutron energy. A ^{3}He spin filter provides an additional reversal of neutron spin of great value in reducing systematic errors associated with flipping the neutron spin. Another disadvantage of a super mirror polarizer is that an analyzer is required to measure the beam polarization. This is not the case for a ^{3}He polarizer [40]. Finally, since a super mirror is a reflective device, the beam line is not straight, complicating the alignment of the apparatus.

3.2.2 Neutron Polarization with a ^{3}He Spin Filter

An alternative method for polarizing the low-energy neutron beam for this experiment is to use a polarizing spin filter. Spin filters operate by selectively removing one of the neutron spin states from the incident beam, and allowing the other spin state to be transmitted with only moderate attenuation. A neutron spin filter can consist of either polarized protons or polarized ^{3}He gas. Because the first option is complicated, expensive to build and operate, and requires a several Tesla magnetic field, we consider here only the second option, the polarized ^{3}He neutron spin filter.

The statistical uncertainty of the experiment depends strongly upon the level of ^{3}He polarization achieved in the spin filter. This dependence can be seen from equations 26 and 27 and figure 10. It will be a technical challenge to reach the necessary level of polarization. However, we believe that the systematic advantages of a spin filter justify the technical effort. ^{3}He spin filters possess properties that improve control over the systematic errors of the experiment. Spin filters do not alter the direction of the neutron beam; they transmit a broad range of neutron energies; and their polarization direction can be changed quickly and easily without changing magnetic fields. As discussed below, each of these properties can be used to address specific systematic concerns.

We hope to reach 65% ^{3}He polarization, but ^{3}He polarizations of 50% or less would still provide adequate rate for this measurement. A recent experiment (SLAC E154) produced 50% polarization in a volume comparable to that needed for this experiment, and we believe that we can improve upon this result.

Neutron Spin-Filters In recent years, neutron beam polarization by transmission through a sample of laser polarized gaseous ^{3}He has rapidly advanced toward practicality. Use of polarized ^{3}He as a neutron spin filter [41] is based on a large neutron capture cross section in the reaction ^{3}He(n,p)^{3}H. The capture cross section $\sigma_n = (v_0/v)\sigma_0$, where $\sigma_0 = 5327$ b at $v_0 = 2200$ m/s, is highly spin dependent due to a broad, unbound resonance in ^{4}He of $J^\pi = 0^+$. In order to conserve angular momentum for this s-wave resonance, only neutrons with spin anti-parallel to the ^{3}He spin are resonantly absorbed. There is only a small potential scattering cross section for neutrons with spin parallel to the ^{3}He spin. Ignoring this small potential scattering cross section, the neutron polarization and transmission are given by:

$$T_\pm = e^{-n_3\sigma_n l(1\pm P_3)} \tag{26}$$

$$P_n = \frac{T_+ - T_-}{T_+ + T_-} = \tanh(n_3\sigma_n l P_3) \tag{27}$$

$$T_n = \frac{T_+ + T_-}{2} = e^{-n_3\sigma_n l}\cosh(n_3\sigma_n l P_3) \tag{28}$$

where n_3 is the number density of the ^{3}He, l is the length of the ^{3}He polarizer, and P_3 is the polarization of the ^{3}He.

^{3}He spin filters polarize neutrons over a broad energy range as illustrated in figures 12 and 13. Figure 12 shows the figure-of-merit (FOM), $P_n^2T_n$, as a function of neutron energy for three ^{3}He polarizations. The shape of the FOM curve depends on the ^{3}He target thickness, but is almost independent of ^{3}He polarization. Therefore, the optimal target thickness does not change appreciably with ^{3}He polarization. These curves are drawn for a ^{3}He filter cell with a target thickness of 5 atm-cm. Figure 13 shows P_n, T_n, and $P_n^2T_n$ as a function of neutron energy for the same filter cell with a 50% ^{3}He polarization.

^{3}He spin filters have been used in several experiments and test set-ups. The first experiment using Rb spin-exchange polarized ^{3}He was done by members of this collaboration at Los Alamos. In the experiment, an epithermal neutron beam was polarized in a measurement of parity violation in a resonant neutron absorption [42]. A small 3 cm^3 ^{3}He cell with 70% polarization and 3.5 atm of pressure was used to polarize epithermal neutrons. Similar techniques have later been utilized at ILL [43], KEK, NIST, and the University of Michigan. More recently, a group in Mainz, Germany has polarized thermal neutrons using a cell of polarized ^{3}He transported from the metastability-exchange factory. This set-up has been duplicated at Grenoble where a variety of experiments are underway [44].

Spin-Exchange Optical Pumping Two methods have been developed for polarization of ^{3}He nuclei: spin-exchange with optically pumped Rb and metastability-exchange from optically pumped metastable ^{3}He. Our current plan is to use the Rb spin-exchange method, although the metastability-exchange method is still being considered as an option. Spin-exchange from optically pumped Rb vapor via the hyperfine interaction of the Rb valence electrons with the ^{3}He nucleus was discovered

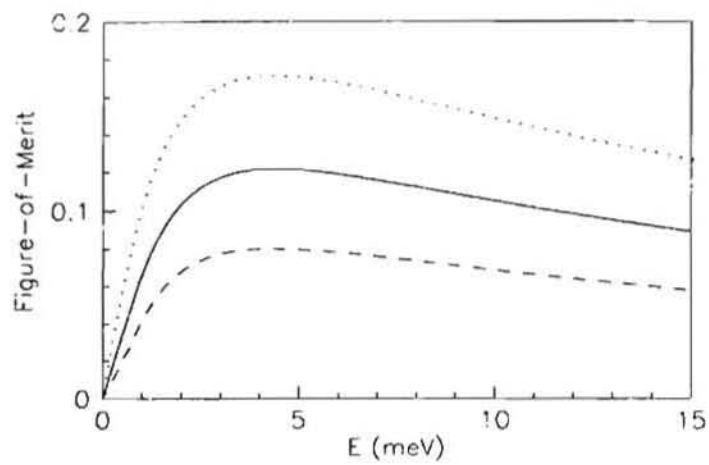

Figure 12: Figure-of-merit, $P_n^2 T_n$, for neutron spin filters with helium polarizations of 40% (dashed), 50% (solid), and 60% (dotted), and a target thickness of 5 atm·cm.

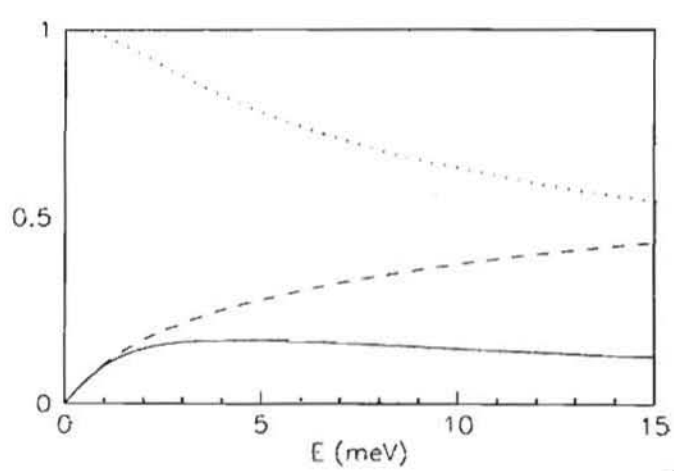

Figure 13: Neutron transmission, T_n, (dashed), polarization, P_n, (dotted), and figure-of-merit, $P_n^2 T_n$, (solid) for a neutron spin filter with 50% polarization and a target thickness of 5 atm·cm.

in 1960 by Bouchiat *et al.* [45]. The polarization of the ^{3}He produced by spin-exchange evolves with time as

$$P_3(t) = P_{Rb}\frac{\gamma_{SE}}{\gamma_{SE}+\Gamma}\left[1 - e^{(\gamma_{SE}+\Gamma)t}\right], \tag{29}$$

where P_{Rb} is the steady state Rb polarization produced by laser optical pumping, $\gamma_{SE} = k_{SE}[\mathrm{Rb}]$ is the rate of spin-exchange from the Rb to the ^{3}He nucleus. Γ is the total ^{3}He spin relaxation rate, which is usually dominated by interactions with paramagnetic impurities on the wall and in the gas. Due to the weakness of spin-exchange ($k_{SE} \approx 0.6\text{-}1.2 \times 10^{-18}$ cm^3/s), Rb densities of 10^{14}-10^{15} Rb/cm^3 and ^{3}He relaxation rates, $1/\Gamma$, of 50-100 hours are required to produce high polarizations [46]. A small amount of nitrogen buffer gas can be added to the cells to suppress radiation trapping for Rb densities greater than 10^{14} [47]. Corning 1720 alumino-silicate and other low iron and/or low helium permeability glasses can be used to suppress wall relaxation.

Sufficient laser power is required to polarize the Rb atoms and to balance Rb spin destruction [48, 49]. The bulk Rb spin destruction rate at high Rb densities and ^{3}He densities below about 5 atm is dominated by Rb-Rb collisions [50] and is given by the total spin destruction rate

$$\Gamma_{SD} = k_{Rb-^3He}[^3\mathrm{He}] + k_{Rb-N_2}[\mathrm{N_2}] + k_{Rb-Rb}[\mathrm{Rb}], \tag{30}$$

where the k's are rate constants for the spin destruction due to collisions of the Rb atoms with the other species and with themselves. For a typical application, $\Gamma_{SD} \approx 500$ s^{-1}. Recently these rates have been re-measured at Princeton, and a strong temperature dependence was observed [51, 52].

The most common lasers in use for Rb optical pumping in high density ^{3}He samples are high-powered laser diode arrays (LDA's) and titanium:sapphire lasers. LDA's dominate current experiments due to price considerations and ease of use compared to Ti:sapphire lasers. We anticipate using about 50 W of laser power from four laser diode bars coupled to optical fiber bundles. The SLAC E154 experiment used three of these fiber coupled LDA's in combination with several Ti:sapphire lasers. In separate studies, the LDA's have been shown to be very effective on their own [53, 54]. At TRIUMF, a target development program produced 70-80% polarization in a 40 cm^3 volume [55]. More recently, up to 5.5% polarization has been achieved in a 200 cm^3 volume with a 10 atm ^{3}He pressure in experiment E154 at SLAC [56]. For the proposed experiment, a 50% polarization would provide adequate statistics, but we hope to extend these results to produce a 65% ^{3}He polarization in a volume of 500 cm^3 at a pressure of 3 atm.

There are several ways to extend the successful SLAC E154 design to the proposed experiment. One possibility is to use a double-cell design [57] similar to that used at SLAC. A double-cell design is essential for electron scattering experiments where the ionization produced by the beam disrupts optical pumping. The double-cell design is convenient because it separates the laser light and the neutron beam. The optical pumping cell would be shaped to optimize coupling to the laser light, and the target cell would be shaped to uniformly polarize the whole neutron beam. The disadvantage of the double-cell design is the complication of construction and the lower average Rb density for a given pump cell temperature.

A second possible design for this experiment uses a single cell. Such a design would simplify cell fabrication and oven design at the expense of added complexity in getting the laser beam into the cell. One version of a single cell design is illustrated in figure 14. In this version, the ^{3}He pressure is held at 2 atm. This is sufficient to provide some broadening of the Rb absorption lines (about 30 GHz) to better match the broad line width of an LDA. Two atmospheres is also practical from a mechanical point of view — holding back 1 atm differential pressure across the 10 cm diameter

window. The consequence of a lower density is the need for up to 50 W of LDA laser power. We are actively pursuing a number of modifications to the single and double cell designs for Rb spin-exchange optical pumping, to better match the conditions of this experiment.

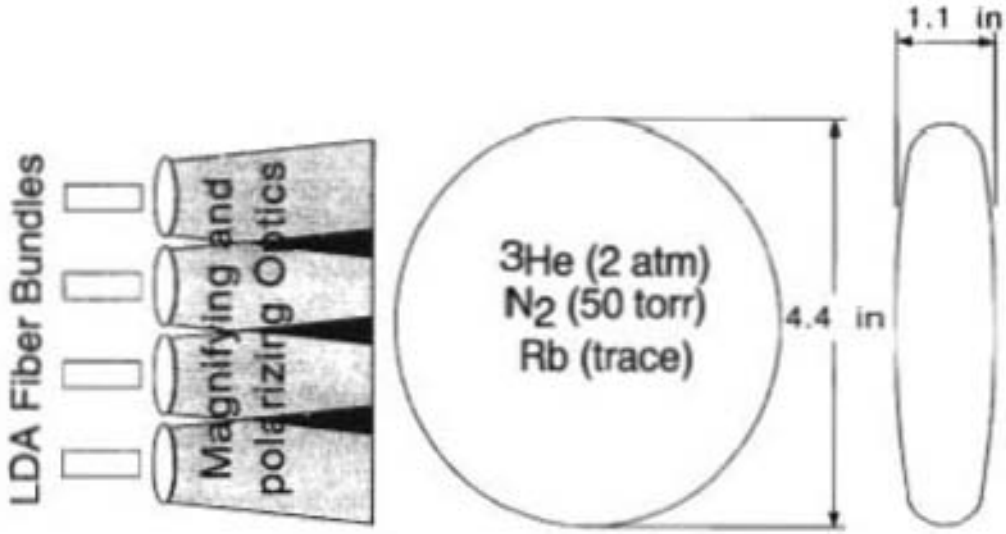

Figure 14: The polarized ^{3}He single cell. The shape and dimensions of the cell accommodate the incident neutron beam, the optimum ^{3}He thickness, and optical considerations. The laser power from four fiber coupled LDA's are incident from the side of the roughly cylindrical cell so that the ^{3}He and the neutrons are transversely polarized.

Metastability-Exchange Optical Pumping Although we currently plan to use spin-exchange optical pumping to polarize the ^{3}He filter cell, it would also be possible to use metastability-exchange optical pumping. In 1962, Colgrove, Shaerer, and Walters [58] demonstrated optical pumping of metastable $^5S_0$ helium in a discharge and thus the possibility of polarizing ^{3}He gas via metastability-exchange between a polarized metastable ^{3}He and a ground state ^{3}He, i.e.

$$^3He^m\uparrow + {}^3He^g \longrightarrow {}^3He^g\uparrow + {}^3He^m \tag{31}$$

The metastability-exchange is a very fast process. It is possible to achieve very high (80%) polarizations in low pressure (a few Torr) samples of ^{3}He. For applications requiring high densities of polarized ^{3}He, the gas must then be compressed without losing the polarization. Metastability-exchange and compression have been used by the Mainz group to produce large volumes of highly polarized ^{3}He. This group built a two-stage titanium piston compressor able to compress 130 cm^3 of polarized ^{3}He to 7 atm of pressure with a final polarization of 46% [59]. Unfortunately, their

apparatus is very complex. To date, they are the only group that has successfully built such an apparatus. Members of our collaboration at Indiana University and at NIST are working to build a metastability-exchange/compressor system to polarize ^{3}He. If this effort succeeds, the new compression system may be ideal for this experiment.

Cell Design Independent of the polarization method, spin filter cells must be made of materials that transmit neutrons. Glass has traditionally been used for polarized ^{3}He cells to achieve the longest spin relaxation times and to transmit the laser light. Unfortunately, most glass contains boron. Natural boron contains 20% ^{10}B, which has a large neutron capture cross section at thermal energies. Two approaches have been used to eliminate this problem: glass can be made using enriched ^{11}B, and materials such as quartz that contain no boron can be used. The NIST group is pursuing construction of cells from ^{10}B-free alumino-silicate glass cells, and the Michigan group is using low-iron quartz that is commercially available. The latest Los Alamos polarized neutron experiments used cells with 3.5 cm inner diameter and 10 cm in length with flat beam windows that were made from ^{10}B-free alumino-silicate glass.

Systematic Considerations ^{3}He neutron spin filters provide several important features that control systematic errors in this experiment. A spin filter's broad transmitted energy spectrum, the ability to change the polarization direction, and the undeflected geometry provide tools for reducing the sensitivity to systematic effects that super-mirrors can not match. There is no high energy cutoff to a spin filter. In fact, figure 13 shows the transmission continuing to increase above 15 meV. As discussed further in section 4.3.1, neutrons with energies greater than 15 meV are quickly depolarized in the target and should demonstrate no gamma asymmetry. These fast neutrons provide an online null test with which to compare the asymmetry signal from the lower energy neutrons.

The direction of the neutron polarization from a spin filter depends only on the direction of the ^{3}He in the filter cell. The ^{3}He polarization can be flipped using adiabatic fast passage (AFP) NMR using a short burst of RF. No magnetic fields need to be changed, although the circular polarization of the laser light must be flipped in order to maintain the new polarization direction. This polarization reversal mechanism provides a powerful systematic reduction technique. The neutron polarization can be changed a few times per day using the spin filter, and every pulse using the RF flipper. These independent flips nearly eliminate sensitivity to systematic effects due to turning on or off the RF spin flipper.

Spin filters do not deflect the polarized beam like super-mirrors do. The target and detector geometry can remain in the same position for high rate systematic tests with the full unpolarized neutron beam. Alignment can be performed independently from the neutron polarizer. In addition, the neutron capture of ^{3}He does not create gamma rays, which is important for a background sensitive experiment. The beam polarization can be accurately monitored using only the transmission through the cell [40], and the acceptance angle of the ^{3}He spin filter is larger than the acceptance angle of the super-mirror polarizer.

The systematic advantages of a polarized ^{3}He spin filter outweigh the challenge of producing the highly polarized ^{3}He gas. Figure 10 shows that the statistical accuracy of the experiment remains quite good even if we do not improve upon the 50% ^{3}He polarization achieved in the SLAC E154 target. If neither the spin-exchange nor the metastability-exchange approaches provide a sufficient ^{3}He polarization, the experiment can still be run with a polarizing super-mirror. This proven technology lacks the systematic advantages of a spin filter, but it should provide a sufficient count

rate for the experiment.

3.3 RF Spin Flipper

There are a number of options for rapid reversal of the neutron polarization; one standard technique is "adiabatic fast passage" (AFP), which has an advantage in that the spin flip results from application of a radio-frequency (RF) field; the RF field can be easily shielded, eliminating possible count rate/asymmetry changes with a changing DC bias field. Unfortunately, AFP requires a substantial magnetic field gradient which, upon spin reversal in the envisioned geometry of the experiment, will create a substantial change in the neutron beam transverse momentum; the resulting change in the incident neutron spatial distribution at the target can easily give a systematic effect at the sought level of experimental sensitivity.

A first-order calculation shows that the trajectory angle changes by

$$\theta \approx h\gamma B_{max}/2E \tag{32}$$

where γ is the neutron gyro-magnetic ratio, B_{max} is the maximum value of the magnetic field in the AFP region, and E is the neutron energy. Taking $B_{max} = 50$ G (as required for efficient reversal of the fastest neutrons) and $E = 0.001$ eV gives an angular deflection of 3×10^{-7} radians; after a 1 m flight from the spin flipper, the center of mass of the neutron beam for this energy neutron would change by 3×10^{-4} mm; if the effective target/detector diameter is 500 mm, the first order change in count rate asymmetry (due to, for example, changes in beam position coupled with detector coupling efficiency or target density variations) could be of order 1×10^{-6}, which is unacceptable.

In order to eliminate the magnetic field gradient deflection, we propose to reverse the neutron polarization using a resonance spin flipper (RSF), which is also based on application of a RF field, however, in this case, in the presence of a homogeneous static magnetic field. The basic idea is that in the presence of homogeneous static and oscillating magnetic fields, one can transform into a rotating frame (about the static field $B_0\hat{z}$) where the RF field becomes static. The effective field becomes

$$\vec{B} = \left(B_0 - \frac{\omega}{2\pi\gamma}\right)\hat{z} + \frac{B_1}{2}\hat{y} \tag{33}$$

for a RF field given by $\vec{B}_{rf} = B_1 \cos(\omega t)\hat{y}$. If $2\pi\gamma B_0 = \omega$, a neutron initially polarized along $\hat{z}$ will precess about the effective field $(B_1/2)\hat{y}$. If the RF field is applied for a time

$$\tau = \frac{1}{\gamma B_1} \tag{34}$$

the neutron spin direction will be reversed relative to $\hat{z}$.

We envision a system where a RF field is confined to a limited space along the neutron beam, in the presence of a homogeneous guide field, with the neutron momentum directed along $\hat{y}$, the direction of the RF field. For fixed RF and guide field values the time/amplitude relation for the spin reversal can be satisfied for only a single velocity component of a continuous beam. However, for a spallation source, B_1 can be varied as a function of time, satisfying the spin reversal condition for all the neutrons in a pulse.

Specifically, we are interested in a neutron energy range of 0.5 to 50 meV, corresponding to a velocity range of 300 to 3000 m/s. If we assume an RF field confined to a length $L_c = 30$ cm along the beam, the maximum RF amplitude would be 3.4 G, which is easily achieved. For a spin flip coil

located $L_0 = 15$ m from the spallation source, the RF amplitude would have to be varied with time as

$$B_1(t) = \frac{v(t)}{\gamma L_v} = \frac{L_0}{\gamma L_v t}. \tag{35}$$

The 3000 m/s neutrons would arrive at the RSF 5 ms after the the spallation pulse time t_0; initially, the RF field would be at 3.4 G, and after 5 ms, would be reduced in amplitude as $1/t$ to a value of 0.33 G at 50 ms. The power requirement (a few amperes of RF current at 30 kHz, into tens of ohms of impedance, corresponds to a power of less than 500 W) and bandwidth requirements are well within the range of commercial audio amplifiers; the ramped signal can be easily generated by a 16-bit DAC driven by the data acquisition system.

The static-field homogeneity and stability requirements can be determined by the effective resonance line width for the slowest neutrons. To achieve a 90% spin reversal, the effective field along $\hat{i}$ in the rotating frame must be less than $B_1/6$, limiting the spatial or temporal variations of B_0 to less than 0.5 G. The magnitude of B_0 is chosen by the transit time of the fastest neutrons, with the requirement that a neutron precesses at least three times in the static field; this corresponds to 30 kHz, or $B_0 = 10$ G; the static field must be homogeneous to a 5% accuracy over the 100 cm^2 beam, and must be stable in time to a 5% accuracy. These constraints are easily achieved, even without static magnetic shielding.

The simplest flip coil would be a solenoid, 20 cm in diameter, 30 cm in length, with aluminum caps at each end, and placed in an aluminum shield. The caps need only be 2 mm thick to effectively shield the 30 kHz (skin depth 0.5 mm).

The eddy currents in the aluminum caps create a field that to a good approximation cancels the $\hat{y}$ component of the RF field at the metallic surface; effectively, the eddy current field is a mirror image of the solenoid in each aluminum end cap. This implies that the transverse fields at the solenoid entrance/exit are twice that of an isolated solenoid, and that the longitudinal gradients are approximately twice as large in these regions. Also, the transverse gradients lead to an additional time dependence of the RF field in the frame of the neutron (the Millman effect); however, the integrated effective B_1 field in the neutron frame varies by less than 5% over a 100 cm^2 region within the 20 cm diameter, 30 cm long solenoid with aluminum end caps.

In the experiment, we envision using the spin flipper to reverse the spin on alternate spallation source pulses. To ensure that the background static magnetic field and possible RF pickup effects remain the same for all pulses, when the spin is not reversed we plan to apply the RF current, ramped in the same way as the spin flip coil, to an identical dummy coil.

In conclusion, we have shown that a resonance spin flipper to give better than 90% spin reversal efficiency can be easily constructed. The primary advantage of the resonance spin flipper is in the elimination of static magnetic field gradients; also, the RF field amplitude is substantially reduced as compared to a AFP spin flipper.

3.4 Liquid Para-Hydrogen Target

A central feature of the proposed experiment is a large volume, thermally stable, and operationally safe liquid para-hydrogen (LH_2) target. A preliminary design of the target has been completed, based on the following design criteria:

- The target volume and shape should be designed to capture at least 50% of the polarized cold neutrons. The fraction of the beam that is not captured must be absorbed efficiently to avoid

creating background ionization in the detector.

- The target volume, pressure, and temperature must be stable; and the target must be capable of running normally unattended for long periods of time (i.e. several months).
- The target must meet the laboratory safety requirements. It must be safe, both during normal operation and in case of loss of power or other equipment failure. Relief valves and burst discs must be installed to prevent rupture of the target vessel or vacuum chamber. Vented hydrogen must be directed away from the experimental area, and hydrogen released into the atmosphere must be kept below the explosive limit. Hydrogen levels must be monitored in the vacuum chamber, in the experimental area, and in the vent path.
- The target liquefier system should be capable of purifying and liquefying hydrogen at a rate sufficient to cool and fill the target from room temperature to operation in 2–4 days time.
- The target must be maintained at a temperature below the boiling point to prevent bubble formation.
- The liquefier system must efficiently convert ortho-hydrogen to para-hydrogen during the filling process.
- The beam entrance windows in the vacuum chamber, radiation shield, and target vessel must be as thin as possible to efficiently transmit the neutron beam and create minimal prompt capture radiation.
- The beam entrance windows must be constructed from zirconium, to avoid systematic errors resulting from neutron-capture reactions on materials such as aluminum.
- The target vessel must be constructed of non-magnetic materials, so that the neutron spin direction can be efficiently transported into the target with negligible beam depolarization.

The above criteria can be met using techniques that have been demonstrated in previous LH_2 targets used for nuclear physics experiments. The proposed target borrows substantially from past designs [60, 61, 62, 63, 64]. A schematic diagram of the target design can be seen in figure 15. It consists of the target vessel, condensate and boil-off lines, a hydrogen liquefier, a cryo-refrigerator, a gas supply and purifier, a pressure relief and vent system, instrumentation, and a vacuum system.

3.4.1 Target Vessel

A Monte Carlo neutron transport analysis was used to determine the size and shape of the target. We found that a cylindrical target, 30 cm diameter and 30 cm long, will capture 65% of the neutron beam. About 15% of the neutrons that do not capture instead scatter back out through the beam window, and the remainder diffuse out the sides or pass through. The target volume is 21,200 cm^3 and contains 1500 g of LH_2 when full. The target surface area is 4240 cm^2. The shape will be slightly conical to enhance convective flow through the target.

Hydrogen is liquid in a limited range of temperature (14–20 K at 1 atm) so the target temperature must be kept very stable to prevent freezing or boiling. This is accomplished by regulating the temperature of the target to approximately 18 K. It is desirable to avoid boiling, since bubbles in the target result in time-dependent density variations, that can potentially cause systematic errors.

Figure 15: Schematic diagram of the LH_2 target design (not to scale).

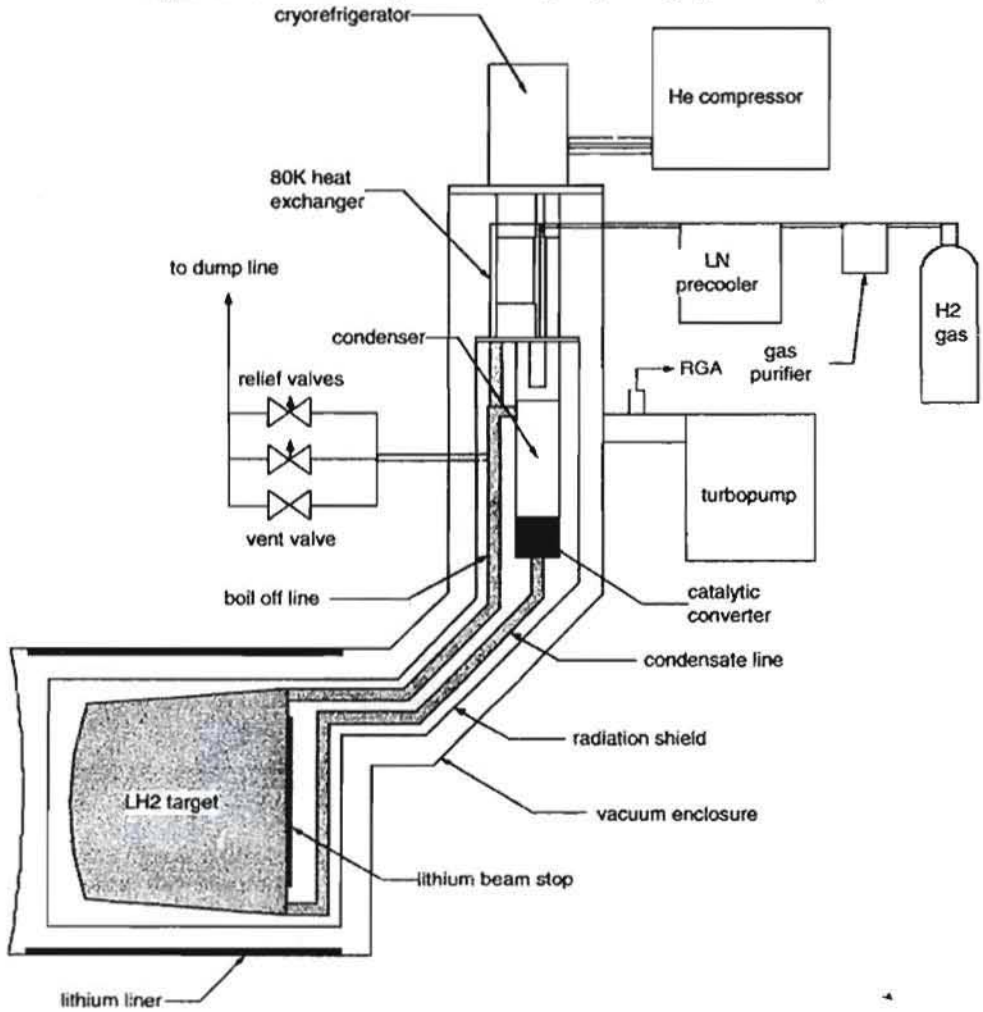

An electric heater connected to a temperature controller will be located on the target to regulate the temperature or to boil the hydrogen when the system is to be warmed and vented.

The target vessel will be constructed of thin (about 0.04 inch thick) aluminum. The beam window will be thinner (0.025 inch) zirconium and convex to strengthen it against the pressure differential. As explained in section 4.2.2, zirconium is used to avoid a systematic error resulting from the capture of neutrons by aluminum. Surrounding the target vessel is a thin (0.02 inch) aluminum or copper radiation shield, again with zirconium beam windows. The radiation shield is covered on both sides with aluminized Mylar "super-insulation" to minimize surface emissivity, except for the beam window area, which is bare. Finally, the target will be enclosed within an aluminum vacuum chamber, which has a concave thin zirconium (0.025 inch) beam window. Lithium fluoride neutron absorber will be placed inside the vacuum chamber to prevent scattered neutrons from escaping into the detector and the experimental area.

3.4.2 Ortho–Para-Hydrogen Conversion

The hydrogen molecule can exist in two different nuclear spin states: ortho-hydrogen, where the proton spins are parallel; and para-hydrogen, where they are anti-parallel. The molecular energies of these two states are different (para-hydrogen is 15 meV lower) so the equilibrium ratio of ortho- to para-hydrogen is temperature dependent. At room temperature the fraction of ortho-hydrogen in normal gaseous hydrogen is 75%, while in LH_2 in equilibrium at 20 K it is only 0.2%. A high concentration of ortho-hydrogen in the target would present a serious problem for this experiment. Ortho-hydrogen has a large spin-incoherent cross section for neutron scattering, so it will rapidly depolarize the neutron beam. Therefore it will be necessary to keep the concentration of ortho-hydrogen in the target near its equilibrium level.

In isolation, the time to equilibrium of newly liquefied hydrogen is quite long, about 5000 hours (the conversion rate constant is 1.14% per hour), so a catalyst is needed to hasten the conversion. In principle any material with a large electronic magnetic moment will catalyze ortho–para-hydrogen conversion. Ferrous hydroxide, neodymium oxide, and chromic anhydride are most commonly used for this purpose and are readily available [65]. In the present target design, the catalytic converter will be contained within a mesh directly beneath the hydrogen condenser. The heat of conversion is higher than the latent heat of vaporization so the hydrogen condensate will tend to vaporize in the converter until the conversion is nearly complete. In this way, when the LH_2 target is full the ortho-hydrogen fraction will be close to its equilibrium value. Because of the large difference in neutron scattering cross sections (see figure 21) below 15 meV, the ratio of para- to ortho-hydrogen can be obtained by measuring the transmission of neutrons through the target.

3.4.3 Cryocooler

Hydrogen can be efficiently liquefied using a commercial two-stage Gifford-McMahon type cryo-refrigerator. This closed-cycle device uses compressed helium gas as a refrigerant and typically obtains 80 K at the first (high power) cold head and 15 K at the second (low power) head. The 80 K head will be used to cool the radiation shield and an initial heat exchanger. The 15 K head will be used to cool the hydrogen condenser.

The target will be filled as follows. Hydrogen gas is admitted at a regulated pressure of 1 atm through a gas purifier, to remove water and particulates, and through a liquid nitrogen (LN_2) filter/precooler. The filter/precooler removes hydrocarbons and condensible gases and cools the

Process	Heat load (J/g)
Cool down from 300 K to 120 K	2400
Cool down from 120 K to 80 K	460
Cool down from 80 K to 20 K	630
Condensation	440
Ortho-para conversion	670

Table 2: Summary of calculated heat loads during liquefaction and filling of the LH_2 target.

hydrogen to about 120 K. It may also contain some ortho-para-hydrogen catalyst material to pre-convert some of the gas. The gas then passes through a pre-heat exchanger, which cools it further to 80 K, after which it enters the condenser. Hydrogen condenses onto copper fins attached to the 20 K cold head, drips down into the ortho-para-hydrogen converter, and follows the condensate line into the bottom of the target vessel. Liquid hydrogen that boils in the vessel flows up through the boil-off line to the top of the condenser where it is liquefied again. This process continues until the target is full, at which point the gas flow is shut off to form a closed system. The target is then maintained at a constant ($\approx$ 18 K) temperature, between the melting and boiling points of hydrogen. The calculated heat loads during liquefaction and filling are summarized in table 2. The total heat needed to fill the target is 3600 kJ in the LN_2 precooler, 690 kJ at the 80 K cold head, and 2600 kJ at the 20 K cold head. To completely fill the target in 72 hours would require 2.7 W at the 80 K head and 10 W at the 15 K head. This is well within the capability of commercially available cryo-refrigerators.

The radiation shield will be cooled by the 80 K cold head of the refrigerator. The power load on the refrigerator due to radiative heating on the shields is estimated to be about 20 W. Using copper and aluminum conductors, it should not be difficult to maintain the temperature of the shield at about 180 K or less around the target vessel. In this case the radiative heat load on the target vessel is about 250 mW. This heat will be removed by the second stage of the refrigerator.

During normal operation, the target temperature is regulated to approximately 18 K. The liquid temperature is determined from the pressure, which will be monitored by a pressure transducer. This signal will also be used to automatically control a heater on the 15 K to maintain this temperature. This will keep the target in a stable condition and prevent the formation of bubbles, which may cause a false asymmetry.

3.4.4 Vacuum system

The target vacuum system will use a turbo-molecular pump to maintain system vacuum $< 10^{-6}$ Torr. Standard ion and thermocouple gauges will measure the vacuum. A hydrogen sensor will be used to monitor the vacuum system for hydrogen leaking from the target.

3.4.5 Hydrogen Safety

Special attention is given to hydrogen safety. We are have formed a working group at Los Alamos for the hydrogen safety of the target. The group consists of ES&H personnel, engineering, and cryogenic and pressure vessel experts. The working group will be involved in the design of the target in the early stage of the work, and its charge will be to provide guidelines for the design, fabrication,

testing, installation and operation of the target. This group will also establish review procedures for different phases of the work. We have also been in contact with personnel at Jefferson Laboratory where two small-size LH_2 targets were recently operated. We plan to draw from their experience and their approach to LH_2 target safety.

Hydrogen gas is explosive in air in concentrations between 4.7–94%. Normally a spark of some kind is needed for ignition, but hydrogen vapor escaping from leaks has been known to spontaneously combust. Therefore it is of paramount importance to design the LH_2 target so that in case of leak or rupture the gas will not exceed the lower explosive limit (LEL) of 4.7%.

A loss of either refrigeration power or vacuum will lead to rapid boiling in the target and an overpressure condition in the target system. The first line of defense against this will be to place the refrigerator and vacuum pumps on an un-interruptible power supply to protect the system from a power failure. If there is an overpressure condition, pressure relief valves on the target system will vent the gas into an argon-filled dump line, through a one-way valve, and into a trunk that exhausts outside the building into a non-flammable area. A large, explosion-proof fan in the trunk will circulate sufficient air to keep the vented hydrogen gas below the LEL. The hydrogen concentration will be continuously monitored in the trunk and in the experimental area. Alarms will alert the operator(s) in case of loss of refrigeration, loss of vacuum, overpressure in the target, or $> 10\%$ of the LEL in any of the hydrogen monitors.

Another mode of failure is a leak from the target system into the vacuum. A hydrogen sensor will continuously monitor the vacuum and alert the operator in case of an increase in the hydrogen pressure, which would indicate a slow leak. In case of a large leak or rupture, the vacuum pumps will trip off, but not vent the system. In case of overpressure, burst discs on the vacuum system will vent hydrogen gas into the dump line and outside the building as described above.

Normal warmup and venting of the target will proceed as follows. The target heater will be energized to increase the rate of boiling to 0.1–1 g/s. A vent valve, which is located in parallel to the relief valves, will be opened and throttled to release hydrogen gas to the dump line at a low and controlled rate, and then through the trunk to the atmosphere outside the building. The gas level will be monitored and kept well below the LEL during this process. When the target system is empty, the system will be warmed to room temperature while flushing with inert gas to remove residual hydrogen.

3.4.6 Instrumentation

A primarily hardware-based instrumentation and control system for the LH_2 target is preferred for reliability and safety. There will be no need for operator control during normal operation of the LH_2 target system System pressure (and hence temperature) will normally be kept within a narrow range slightly above 1 atm (*e.g.* 16–18 psi) by a heater on the 15 K cold head, regulated by a PID controller. The following parameters will be continuously monitored: target pressure (pressure transducer), target level indication (low power resistors), refrigerator cold head temperatures (thermocouples), vacuum pressure (ion gauge) , hydrogen in the vacuum (hydrogen sensor), vent line temperature (thermocouple), and hydrogen gas concentration at various points (hydrogen sensors).

3.5 Gamma Detector

3.5.1 Cesium Iodide Scintillators

The alkali iodides are particularly well suited for the detection of energetic γ-photons because of their high density (4–5 g/cm^3) and the high atomic number of iodine ($Z = 53$). To stop more than 95% of the 2.2 MeV γ-rays, three mean free paths are required, corresponding to a 15 cm thick CsI crystal. The list of basic properties of a few candidate inorganic scintillators are shown in table 3. Our choice for the scintillator is CsI(Tl).

	NaI(Tl)	CsI(Tl)	CsI	
Density	3.67	4.53	4.51	g/cm^3
Index of Refraction	1.85	1.80	1.80	
Interaction Length (2.2 MeV)	5.1	5.5	5.5	cm
Temperature Gradient [66, 67]	−0.4	< 0.2	−1.5	%/°C
Relative Light Yield	1	0.4	0.1(fast), 0.02(slow)	
Decay Time	250	1000	10, 36(fast), 1000 (slow)	ns
Wavelength of Maximum Emission	415	540	310(fast), 480–600(slow)	nm
Average Scintillation Efficiency [68]	11.3	11.9		%
Hygroscopicity	very	somewhat	somewhat	

Table 3: A comparison of crystal scintillators.

Luminescence in crystal scintillators originates from emission centers in the crystalline compounds themselves or centers formed by activating agents introduced into the crystal in controlled amounts. Imperfections due to lattice dislocations, impurities or radiation damage in the crystal create additional energy levels in the energy gap region. Excitons in the energy gap or electrons in the conduction band can move into these energy levels that correspond to activation centers of three types:

1. Luminescence centers, at which recombination of an electron-hole pair excites the center and then a decay occurs via a photon emission; fluorescence. This is the main mechanism of the scintillation light.

2. Quenching centers, are like luminescence centers except that the excitation energy is dissipated as heat via phonons instead of photons. This means that a change in the gamma ray rates will change the temperature of the crystal and thus has an effect to the detection efficiency.

3. Traps, which are metastable energy levels at which electrons and holes, or excitons, can remain for a long time before acquiring sufficient thermal energy to return to the conduction and valence bands or to move to a luminescence or quenching center. When they do move to a luminescence center, this delayed emission of light is called phosphorescence. In some cases the delayed emission has been measured to be very long [69].

The shape of the scintillation pulse depends on the type of crystal, nature and concentration of the activator, type of radiation detected and temperature. The fall time of the pulse can be typically resolved into the two main components:

1. A prompt, exponential component (fluorescence) with a time constant from a few hundred nanoseconds to a few microseconds.

2. A delayed component (phosphorescence, delayed fluorescence) lasting several microseconds.

The fact that the delayed component may account for as much as 20% to 40% of the total emission of light sets a limit on the usefulness of the crystal scintillators in high-count rate pulse counting applications. In the $\vec{n} + p \rightarrow d + \gamma$ experiment the gamma rates are too large for the pulse counting and therefore the current mode γ detection will be performed (see section 3.5.2). We have studied the scintillation decays in a CsI(Tl) crystal 2.5 cm thick and in a CsI(pure) crystal 15 cm thick using cosmic rays. Figure 16 shows an averaged scintillation decay of CsI(Tl) and CsI(pure). We fit the decay of the light from cosmics on CsI(Tl) to a Gaussian with exponentially decaying tails. Four different decay components can be identified with time constants of 1.6, 4.9, 21, and 120 μs. For the CsI(pure), the decay can be fit with three time constants: 2.5, 7.2, and 62 μs. None of these component are long enough to cause any serious problem to the experiment.

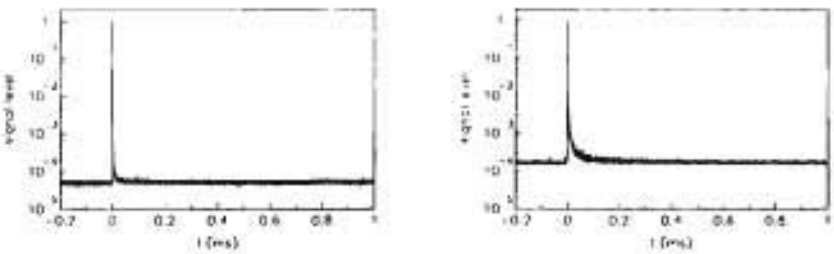

Figure 16: Light output as a function of time for pure CsI (left) and CsI(Tl) (right) from cosmic ray events. The signals have been averaged over approximately 20,000 events, and are normalized to unity at the peak light output.

The segmentation of the detector is required to resolve the angular dependence of the expected parity-violating signal and discriminate false effects. The importance of the segmentation of the detector and its solid angle is discussed in section 3.1.

A total of 48 CsI(Tl) scintillators, with a size of $15 \times 15 \times 15$ cm^3, will be placed around the liquid hydrogen target as indicated in figure 17. The plan is to couple the CsI(Tl) crystals to either 5 inch photomultiplier tubes or vacuum photo-diodes that have S20 photocathodes. The signals are then taken directly from the anode to decrease the sensitivity of the detector gain to magnetic fields and other drifts as discussed in section 3.5.3. The S20 photocathode has a response curve that matches well with the spectral distribution of the scintillation emission from CsI(Tl), which has a maximum at 540 nm.

Temperature influences scintillation effectiveness (number of photons emitted per unit time per radiation in MeV), pulse decay time and emission spectrum. For CsI(Tl), the temperature sensitivity has been measured to be less than 0.2% per °C. Similar detectors have been observed to have acceptably low gain drifts (< 1% per week [70]).

The slight hygroscopicity of the crystals will be handled by closing the crystals into sealed aluminum cans. The canning will also help the mounting of the crystals around the liquid hydrogen

Figure 17: Proposed design for the CsI detector array.

target.

Radiation damage of the crystal will decrease the transparency of a crystal resulting in a decrease in detected light. CsI(Tl) has been found to be rather radiation hard [71] up to doses of more than 50 kRad.

3.5.2 Current Mode Signal

Because of the high gamma-ray rates (10^{10}–10^{13} s^{-1}, depending on neutron time-of-flight), single-pulse counting is not possible. Even when divided among 48 detector elements, the rates are too high. Instead, current-mode techniques are used. Since the average time between detector pulses is much shorter than the pulse width, the signal from the photocathode takes the form of a continuous current whose magnitude is proportional to the instantaneous detector rate. The effect of counting statistics is manifest as a quantum shot noise, due to the discrete nature of the charge deposited by each gamma. This shot noise can be described as a current noise density, which is given to a good approximation by $I_{sn}/\sqrt{I} = \sqrt{2qI}$, where q is the charge deposited per gamma and I is the photocathode current.

3.5.3 Amplification of Photocathode Signal

Light of scintillation from the CsI(Tl) strikes the detector photocathode, causing the emission of typically 500 photoelectrons for every 2.2 MeV gamma. This process results in a current that must be amplified and converted to a voltage before it is digitized. To preserve the statistical accuracy of the signal, the amplifier must contribute very little noise. Normally, this amplification is done by an electron multiplier, contained within the photomultiplier tube.

Although an electron multiplier is very low noise, it is also quite sensitive to magnetic fields. A 10 G magnetic field reduces the gain of a typical photomultiplier tube by a factor of 10. Since a changing magnetic field (either DC or RF) is required in our case to reverse the neutron spin direction, such a large sensitivity to magnetic fields can result in a spin-dependent detector efficiency. The resulting systematic error is avoided altogether by using an electronic amplifier instead.

The efficiency change of the photocathode due to magnetic fields is more than four orders of magnitude smaller than for the electron multiplier (see section 5.1.4); only 2×10^{-5} G^{-1}. The requirements on magnetic shielding are then reduced to a practical level. Instead, the difficulty is in designing an electronic preamplifier that has low enough noise. This problem has been solved, as

will be seen in the next section.

3.6 Detector Electronics

The detector electronics must transform the signal from the gamma detectors into digital form without significantly increasing the noise above the shot noise of the signal. In addition, this criterion must be met over a wide dynamic range, including total count rates from 10^{10}–10^{13} s^{-1}. A third criterion is that the detector efficiency must be very insensitive to magnetic fields to avoid systematic errors resulting from changes in magnetic fields during neutron spin reversal. This last requirement rules out the use of electron multipliers, such as are found in photomultiplier tubes. While such devices act as extremely low-noise current amplifiers, the gain is notoriously sensitive to magnetic fields. Instead, electronic amplifiers are used throughout.

The process of converting the detector photo-currents into digital signals occurs in stages. First, the anode currents are converted to voltages by low-noise current-to-voltage (IV) preamplifiers located in the detector bases. Second, the detector signals are combined by taking sums and differences in order to reduce the dynamic range requirements. Finally, the sum and difference signals are digitized. The detector electronics are shown schematically in figure 18.

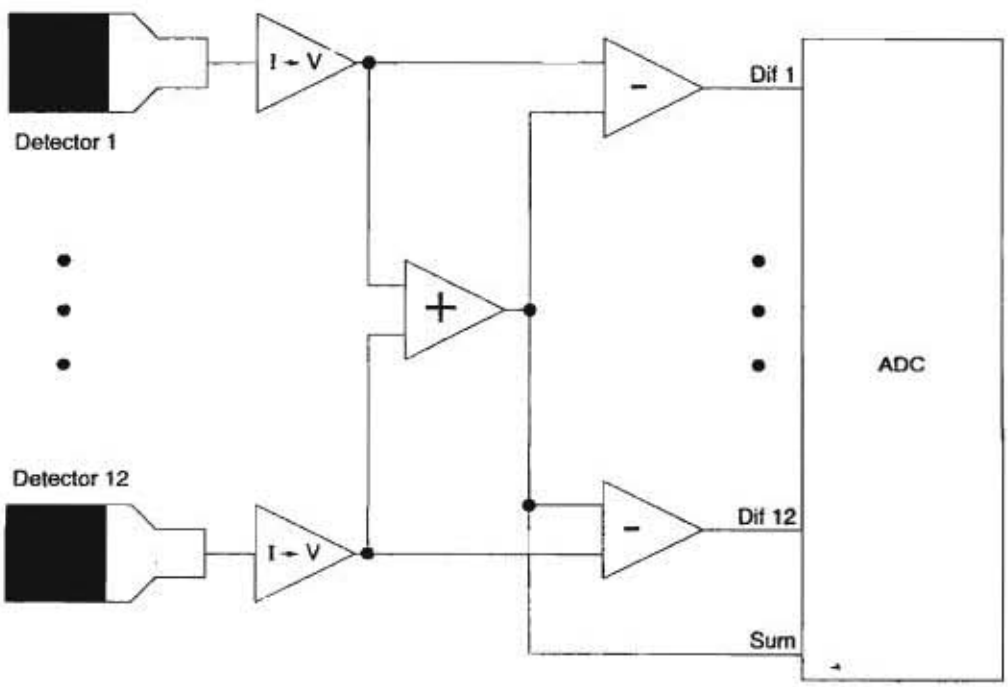

Figure 18: Schematic representation of the detector electronics.

In addition to the current-mode electronics, pulse-mode electronics are needed for calibration and

diagnostics. This system will consist of standard phototube bases, amplifiers, and charge-integrating ADC's. In this mode of operation, the preamplification will be performed by the electron multiplier in the phototube. Such an arrangement will be used at a reduced neutron flux to check the detector efficiencies and establish background levels. For these tests, it is not necessary to operate the entire detector array simultaneously, and so the pulse-mode electronics will have a smaller number of channels than the current-mode electronics.

3.6.1 Low-Noise Preamplifiers

The statistical fluctuations due to the number of detected gammas appear as shot noise in the photocathode currents I, given by the rms current noise density $I_q/\sqrt{f} = \sqrt{2Iq}$, where q is the charge deposited per gamma. A second source of signal fluctuations, variations in the number of electrons produced in the photocathode per gamma incident on the detector, is small by comparison. Electronic noise in the IV preamplifiers must be small compared to the signal fluctuations in order to preserve the statistical accuracy of the measurement. This requirement is most stringent at the lowest anticipated count rate, 10^{10} s^{-1}, where $I_q/\sqrt{f} = 1.6$ pA/$\sqrt{\text{Hz}}$ from a photocathode current of 16 nA for each detector. A suitable current-to-voltage amplifier has been constructed and successfully tested, displaying a noise density equivalent to only 20 fA/$\sqrt{\text{Hz}}$. Equally important, the amplifier has a sufficiently short time constant (100 μs) to allow measurement of the neutron time-of-flight.

The preamplifier design is shown in figure 19. The circuit functions as a current-to-voltage amplifier, built around an AD745A low-noise operational amplifier, having a typical voltage noise of 2.9 nV/$\sqrt{\text{Hz}}$ and typical current noise of 6.9 fA/$\sqrt{\text{Hz}}$ at 1 kHz. The feedback resistor is 10 MΩ, giving a DC gain of 10 V/μA. The 10 pF feedback capacitor limits the 3 dB bandwidth to approximately 3.0 kHz, corresponding to a time constant of approximately 50 μs. Precision resistors with low temperature coefficients (20 ppm/°C) are used to reduce thermally-induced drifts.

3.6.2 Sum and Difference Amplifiers

Since we are interested in a small ($\approx 5 \times 10^{-8}$) variation in gamma yield as a function of azimuthal angle ϕ, the dynamic range requirements for the signals can be greatly reduced by taking appropriate differences in hardware. If the counting rates in all detector elements are equal, it is sufficient to subtract the average signal from each individual signal, and then digitize the differences as well as the sum. In our test measurements we found that such differences remained stable to $\approx$ 1% of the original signals, allowing a reduction of two orders of magnitude in dynamic range. In practice, because the detector elements do not view the target with the same solid angle, detectors will be grouped according to solid angle, with differences from the mean being formed within each group. With this technique, differences between any two detectors within the same group can be reconstructed with statistically-limited uncertainties during analysis of the data.

3.7 Data Acquisition System

Like the detector electronics, the data acquisition system can be described in stages. Transient digitizers sample the sum and difference signals many times during each beam burst. These digitizers reside in a VME crate and store the data in memory shared with the VME controller. This controller performs some compression on the data and writes it to a tape drive, either directly or through a

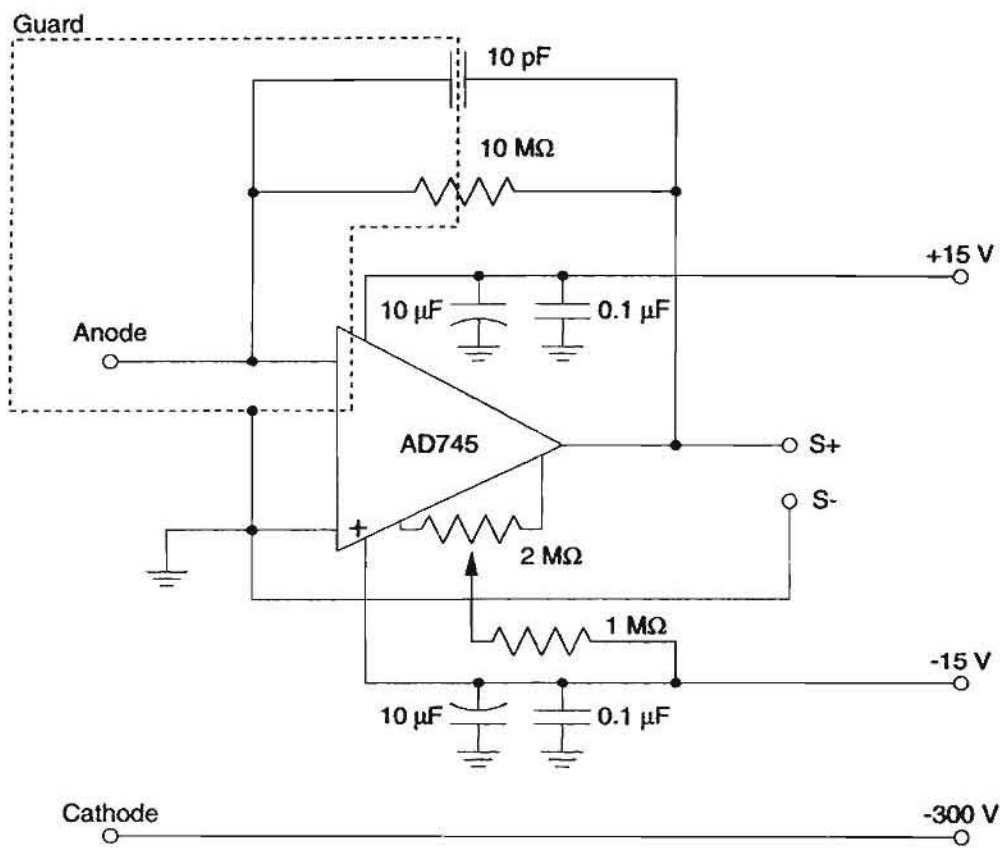

Figure 19: Circuit diagram for the photocathode preamplifier.

personal computer (PC)-based data acquisition system. The PC system performs the tasks of monitoring, control, and online analysis and display. An off-line system is also required for the final analysis of the experimental data. In addition, since the collaboration consists of many institutions, a mechanism must exist for providing remote access both to the data and to the computing resources.

3.7.1 VME-Based Data Acquisition Electronics

The sum and difference signals will be digitized by commercially available[2] 16-bit transient digitizers, with a maximum sampling rate of 100 kHz. The signals need to be sampled several times during each beam burst to provide neutron time-of-flight information. There is, however, a more stringent requirement on the sampling rate. Because of the very high counting rates, small statistical accuracies are obtained in a short time. If the sampling interval is too long, the one-bit uncertainty in the digitization process can approach the size of the statistical uncertainty. For this reason, we will sample at 10 μs intervals. Several samples can then be averaged to reduce the amount of data, while retaining the statistical accuracy. The electronics arrangement for one fourth of the full detector array is shown schematically in figure 18.

The transient digitizer contains a controller and its own memory. The memory will be divided into two buffers, which will be used to hold the data from alternate beam pulses. The inactive buffer can be read by the VME host computer, which performs the signal averaging and combines the data with other information, such as neutron time-of-flight and spin direction. The full event information is then transferred both to tape and to the PC data acquisition system (DAQ) for further online processing, monitoring and display. Control commands can be sent from the PC DAQ to the VME host to stop and start data acquisition, or change to diagnostic modes, for example. All of the VME components are commercially available and supported with industry-standard software.

3.7.2 PC-based Data Acquisition System (PC DAQ)

The PC-based data acquisition system (PC DAQ) will provide monitoring and control of the VME system, as well as online analysis and display. PC DAQ is a full-featured DAQ and analysis shell. The program provides both DAQ and replay (disk file input) modes. It can also be used for Monte Carlo projects. Extensive software control flags, which may be set either in script command files or interactively, are provided so that the user can control the flow of data through the program. PC DAQ is designed to run on a 32-bit Windows operating system (Windows 95, Windows NT 4.0, or above) running on the INTEL 80x86 processor line.

PC DAQ provides histogramming, testing, and plotting packages. Histogram data can be exported to spreadsheets or analyzed in user supplied programs. The test package defines tests that are used to see which histograms should be incremented. Tests can be defined in scripts or interactively (indirect gates and boxes). Test result summaries can be printed or copy/pasted into other programs. The plotting package is based on the xyPlot package defined by Tom Mottershead. Plots can be copied as bitmaps to other programs or printed. Plot analysis is in user supplied FORTRAN analysis code.

An upgrade to provide VME capability is underway. Other usability changes can also be expected. A full description of PC DAQ may be found in [72].

[2] Alphi Technology, Tempe, Arizona

3.7.3 Data Storage and Distribution

Raw data from the VME system will be written to tape through a standard SCSI interface. This data will be written at a time-averaged rate of approximately 600–700 kbytes/s, and will consist of digitized difference signals for each detector, averaged over approximately 100 samples, as well as digitized sum signals, neutron time-of-flight, and auxiliary information such as beam intensity, neutron spin direction, etc. This rate is well below the limits of current technology. Since each tape has a capacity of 20 Gbytes, tapes will be filled at a rate of approximately one every two days. Automatic tape changers are available to ensure that new tapes are loaded as needed.

PC DAQ writes its data, i.e. histograms and test results, to disk. Past practice with PC DAQ has been to periodically archive these disk files onto tape and then reclaim the disk space. PC DAQ can automatically start new runs at fixed intervals so that no one run is too large for efficient analysis. This also means that it can run in an unattended mode for long periods if the tape drive has a tape changer attached. Since PC DAQ will be writing the compressed data only, requirements on speed and storage capacity are approximately 10 times less than for the raw data.

The full data-set after one year (live) of running will consist of approximately 4 Tbytes of raw data and 400 Gbytes of compressed data. Access to the raw data will rarely be needed, and it will remain archived on tape. Collaborators at remote locations will, however, require access to the full set of compressed data. The simplest and most cost-effective alternative, at present, is to make the tapes available through a large-capacity (approximately 20 tape) tape changer. The disadvantage of this primary approach is access time, which could become prohibitive, if low-level data analysis is to take place remotely. Alternative technologies include large disk farms and digital video disks. While both of these options are, at present, quite expensive, prices are dropping rapidly as the technology advances and may soon (mid-1998) be practical.

3.8 Magnetic Guide Field

Three different sets of transverse magnetic fields are required by the experiment. The first field is the 10 G Helmholtz field of the polarizer, the second field is the 10 G field that guides the neutron spin to the spin flipper and then to the LH_2 target. The third field is the 10 G static field of the resonance spin flipper described in section 3.3. Careful design is needed to match the fields to each other to prevent depolarization.

For maximum ^{3}He polarization and minimum polarization losses during polarization reversal by the adiabatic fast passage, the inhomogeneity of the polarizer field has to be less than 3 mG/cm [73, 74]. Magnetic field gradients in the ^{3}He cells would cause spin relaxation of the polarized ^{3}He gas, which would compete with the slow spin exchange polarization process. Once the neutron beam is polarized, a static magnetic guide field is required to maintain the polarization. The projection of the neutron spin on the field direction is an adiabatic invariant, and is approximately conserved when ω_B/ω_L is small. Here, ω_B is the rate of change of the magnetic field direction, and ω_L is the neutron spin Larmor frequency, 29 kHz at 10 G. The 10 G guide field is large compared to ambient magnetic fields.

The magnetic guide field will be created by a series of Helmholtz coils, oriented along the direction of neutron polarization (vertical). The diameters of the coils will vary according the size of the apparatus and the homogeneity requirements in each region. Trim coils will be used to improve the field uniformity in the transitions between adjacent coils. Monte Carlo [75] calculations of the neutron spin transport will aid in the design of the coils.

4 Systematic Effects in the Experiment $\vec{n} + p \rightarrow d + \gamma$

We distinguish between statistical (section 4.1) and systematic (section 4.2) errors. The experiment is designed to measure the directional asymmetry of the emission of gamma rays with the neutron spin direction. A systematic error produces a signal in the detector that is coherent with the state of the neutron spin; for example, the current in a magnet used to flip the neutron spin might be picked up by the gamma detector, or a guide field might steer the neutron beam up-down as the spin is changed from up to down. A source of statistical error produces a detector signal that is not correlated with the neutron spin direction; for example fluctuations in the number of detected gamma rays due to counting statistics or drifts in amplifier offsets. The size of statistical errors is important when discussing systematic errors, because it is important to be able to diagnose systematic errors in a time that is short compared to the time it takes to measure the directional γ asymmetry. Systematic errors can be further classified according to whether they are instrumental in origin and are present whether or not neutrons are being detected or arise from an interaction of the neutron spin other than the directional γ asymmetry in the $\vec{n} + p \rightarrow d + \gamma$ reaction, for example the parity-allowed asymmetry $\vec{s}_n \cdot (\vec{k}_n \times \vec{k}_\gamma)$. Finally, it is important to isolate and study experimentally potential sources of systematic errors. For example we can search for false asymmetries from activation of components of the apparatus due to the capture of polarized neutrons by emptying the liquid hydrogen target. We can monitor in situ effects such as the parity allowed $\vec{s}_n \cdot (\vec{k}_n \times \vec{k}_\gamma)$ correlation in $\vec{n} + p \rightarrow d + \gamma$ that produces left-right asymmetries. We discuss auxiliary and in situ systematics checks in section 4.4 below.

4.1 Statistical Errors

The statistical uncertainty associated with the number of gamma rays detected, counting statistics, is unavoidable; the limit is set by the beam intensity and the detector solid angle. The design goal of the detector, electronics, and data acquisition system is to make other sources of noise small compared to counting statistics. In order to measure the asymmetry with a statistical accuracy of 0.5×10^{-8} in one year, it is necessary to observe $\approx 4 \times 10^{16}$ photons. The asymmetry must be measured with an accuracy of 1×10^{-4} for each neutron beam pulse. In section 3.6 we showed that electronic noise and drifts were small compared to counting statistics. The preamplifier noise is more than 100 times smaller than counting statistics at the rates that will be achieved in the apparatus. This very low level of electronic noise has important implications for our ability to diagnose systematic errors that are instrumental in origin.

4.2 Sources of Systematic Effects

4.2.1 Systematic Errors of Instrumental Origin

It is not possible to give a complete list of sources of instrumental systematic errors. Many come to mind: the influence of magnetic fields on detector gains, shifts in the mains voltage as power supplies are turned on and off, leakage of control signals into preamplifiers, etc. It is essential to be able to tell whether such effects are present in a short time, to learn where they come from, and fix them. These effects are not associated with the neutron beam. There are two types of instrumental asymmetries; additive couplings and gain shifts. Additive couplings will be diagnosed by running the experiment with the beam off and looking for a non-zero up-down asymmetry. The electronic

noise is 1/100 of counting statistics. In the presence of electronic noise only, achieving an accuracy of 0.1×10^{-8} (the statistical error in A_γ will be 0.5×10^{-8} in one year of data) will require a running time $5^2/100^2$ of 1 year, ≈ 1 day.

In order to search for gain shifts we will illuminate the detectors with light from light emitting diodes. The level of illumination will produce a photo-cathode current 10 times larger than that due to neutron capture where we expect the number of photo-electrons per 2.2 MeV gamma from CsI(Tl) will be ≈ 500. The time to measure a gain shift of 0.1×10^{-8} will be $5^2/(10 \times 1000)$ of 1 year ≈ 1 day. We will be able to diagnose and eliminate instrumental systematic errors before we take beam, and without a complete apparatus. We will be able to check for problems during periods when the beam is off.

The most important experimental tool we have to isolate a parity violating signal in this experiment is the neutron spin flip. It is therefore absolutely essential that the process of flipping the neutron spin have a negligible effect on all other properties of the apparatus. In this section we discuss some of the ways that this idealization may fail, and our estimates for the size of the resulting systematic effect.

In our considerations above we assumed that the spin flip process is "perfect", that is, that the only difference between the flip/no-flip states of the experiment is that the neutron polarization is reversed. In practice this condition cannot be met. We now relax these assumptions and consider the consequences. We will concentrate on two methods of neutron spin reversal: use of a RF magnetic field on the neutron beam and reversal of the polarization direction of the ^{3}He polarizer.

One method of spin reversal consists of reversing the polarization direction of the ^{3}He target. The ^{3}He spin can be reversed by an adiabatic fast passage or adiabatic reversal of the magnetic holding/guide field. The magnetic field (at the polarizer the fully polarized ^{3}He nuclei create a field of about 2 Gauss) due to the reversed magnetic moments of the polarized ^{3}He nuclei in the neutron polarizer causes a change in the static magnetic field at the location of the gamma detectors. This change is about 1×10^{-6} Gauss. Coupled with the measured change in the gamma detector efficiency 2×10^{-5} per Gauss, this gives a negligible efficiency change of 2×10^{-11}.

The other method of neutron spin reversal is effected by turning on and off the ≈ 30 kHz magnetic field in the spin flipper. This field, although closer to the detectors than the ^{3}He cell, can be shielded very effectively because the skin depth of the 30 kHz RF field in aluminum is 0.5 mm. In addition, the intrinsic detector efficiency should be less sensitive to an RF field than a DC field. Care must be taken to insure that there is no spurious electronic pickup induced by the RF switching. We intend to forestall this problem by switching the RF power into a dummy coil when the neutron spin is not being flipped.

We will reverse the neutron spin on a 20 Hz time scale using the RF spin flipper with a $+ - - + - + + -$ pattern. This pattern eliminates the effects of first and second order drifts, as discussed in section 4.2.3. The neutron spin will be reversed every few hours by reversing the polarization direction of the ^{3}He polarizer. Finally, we will reverse the direction of the holding/guide field every few hours. Instrumental effects arising from the state of the RF spin flipper, the ^{3}He cell, the holding/guide field, or from other parts of the apparatus will have different dependences on the different reversals. These different dependences can be used to identify the source of potential instrumental systematic errors. Any instrumental or spin-dependent systematic error that depends on the ^{3}He state, the spin flipper state, or the holding field state would be eliminated by averaging over different reversal methods.

4.2.2 Systematic Errors from Interactions of the Neutron Spin

In this section we consider systematic errors arising from interactions of the polarized neutron beam itself. This type of false effect is potentially the most difficult to eliminate. Fortunately, these effects are all small, $\ll 10^{-3}$, and do not require heroic efforts to eliminate. In order to produce a false asymmetry, an interaction must occur after the spin is reversed by the RF spin flipper, otherwise the effect of the interaction would be averaged out by the eight-step reversal sequence. The interaction must involve the inner product of the neutron spin vector and some vector made up of the vectors and scalars from the initial and final states. At least one quantity from the final state that deposits energy in the detector must be involved. We have tried to identify all possible Cartesian invariants that satisfy these conditions and evaluate the associated false asymmetries. We evaluated invariants that produced asymmetries $\approx 10^{-10}$ more carefully than asymmetries $\ll 10^{-10}$. Different potential sources of false asymmetry produce effects that depend on time of flight (neutron energy) in a characteristic fashion. The $\vec{n} + p \to d + \gamma$ directional asymmetry, A_γ, produces an up-down pattern (for neutron spin up-down) that is independent of neutron energy up to an energy of 15 meV. Above 15 meV, the neutrons depolarize in the para-hydrogen and the asymmetry vanishes.

$\vec{n} + p \to n + p$ The parity-conserving transverse analyzing power A_y for np elastic scattering shifts the neutron beam centroid left-right before capture takes place. This shift changes the effective solid angles of the detectors, producing a left-right γ-ray asymmetry. Because of the low energy of the neutrons, however, the scattering is almost purely s-wave. Since p-wave scattering is necessary for $A_y \neq 0$, the effect scales as k, the neutron momentum. Extrapolating from $A_y \approx 5 \times 10^{-5}$ at 10 keV [76], averaged over the detector angles, we obtain $A_y \approx 2 \times 10^{-8}$ at 1 meV. Since this effect produces a left-right asymmetry, the systematic effect in the up-down direction is estimated to be a factor of 100 smaller, giving a false asymmetry $F \approx 2 \times 10^{-10}$.

$\vec{n} + p \to d + \gamma$ There are two sources of false asymmetry associated with the capture reaction itself. The gamma-ray has a small circular polarization correlated with neutron spin corresponding to the parity even ($P+$) and time reversal even ($T+$) invariant $\vec{\epsilon}_\gamma \cdot \vec{\epsilon}_n$, and there is a small $P+$ and $T-$ left-right asymmetry corresponding to the invariant $\vec{\epsilon}_n \cdot (\vec{k}_\gamma \times \vec{k}_n)$. These asymmetries are potentially dangerous because the experiment is designed to efficiently detect this decay mode. We estimate these false effects below and find them to be small compared to 0.5×10^{-8}. The branching ratios for the double radiative capture mode ($\vec{n} + p \to d + \gamma + \gamma$) is 1% of the dominant $\vec{n} + p \to d + \gamma$, so this mode is neglected. The branching ratio for the pair decay mode ($\vec{n} + p \to d + e^+ + e^-$) is 2% of $\vec{n} + p \to d + \gamma$ and this mode is also neglected.

$\vec{\epsilon}_n \cdot (\vec{k}_\gamma \times \vec{k}_n)$ The size of this asymmetry, $A_{t-\gamma}$, has been calculated by A. Csótó and B.F. Gibson [77]. They find: $A_{t-\gamma} = 0.23 \times 10^{-8}$ ($E_n = 1$ meV). The asymmetry is left-right and the symmetry of the apparatus will suppress its effect by $\approx 10^{-2}$, leading to a false asymmetry of 1×10^{-10}. The TOF of this asymmetry is t^{-2}, and there is no asymmetry above 15 meV.

$\vec{\epsilon}_n \cdot \vec{\epsilon}_\gamma$ The transfer of neutron polarization to gamma-ray circular polarization is small: 1.5×10^{-3} [78] and the analyzing power for gamma-ray circular polarization is small; this analyzing power arises from Compton scattering from polarized electrons. For 10 cm of saturated iron, the analyzing power is $\approx 10^{-2}$; for a false asymmetry of 10^{-10} we can tolerate no more than 5×10^{-4} g/cm^2 of fully magnetized iron. This limitation precludes the use of ferromagnetic

materials in the apparatus. The susceptibility of liquid hydrogen and aluminum are small and the magnetization of these materials in a 10 Gauss field are 2×10^{-10} and 3×10^{-9}, respectively, relative to fully magnetized iron, and these materials pose no problem.

Neutron Beta Decay $\vec{n} \to p + e^- + \bar{\nu}$ The weak decay symmetries, in regard to analyzing power induced false asymmetries, are $P-$ and $T+$; the beta direction is correlated with the neutron spin direction. The fraction of neutrons that decay in the target is approximately the stopping time divided by the neutron decay time

$$\approx \frac{10^{-4}\ \mathrm{s}}{10^{3}\ \mathrm{s}} \approx 10^{-7}. \tag{36}$$

The asymmetry is 0.11 and the conversion of beta energy to gamma energy in the slowing down process is small — the fractional radiation yield for a beta having half the end point energy $Q_\beta/2 =$ 0.39 MeV is 3.6×10^{-4} [79]. We estimate the false asymmetry F to be

$$F \approx (10^{-7})(0.11)\frac{0.39\ \mathrm{MeV}}{E_\gamma}(3.6 \times 10^{-4}) \approx 7 \times 10^{-13}, \tag{37}$$

where $E_\gamma = 2.2$ MeV. The effects of the radiative decay $n \to p + e + \nu + \gamma$, internal bremsstrahlung, is estimated as

$$F \approx (10^{-7})(1.1 \times 10^{-1})\frac{\alpha Q_\beta}{E_\gamma} \approx 3 \times 10^{-11}, \tag{38}$$

where α is the fine structure constant. The circular polarization of gammas from bremsstrahlung is ≈ 1, but the small analyzing power for circular polarization discussed above in the case of $\vec{s}_n \cdot \vec{s}_\gamma$ makes this source of false asymmetry negligible.

$\vec{n}+d \to t+\gamma$ A deuterium (D_2) contamination in the liquid hydrogen target can produce gammas via $\vec{n} + d \to t + \gamma$. An upper limit for the gamma asymmetry of 1.5×10^{-6} was obtained using the DDH limits for H^1_π and H^0_ρ. The abundance of D in H is $\leq 1.5 \times 10^{-2}$, the D cross section is 1.5×10^{-3} that of H, and the energy of the gamma ray is 6.2 MeV. We estimate the false asymmetry to be

$$F \approx (1.5 \times 10^{-6})(1.5 \times 10^{-2})(1.5 \times 10^{-3})\frac{6.2\ \mathrm{MeV}}{2.2\ \mathrm{MeV}} \approx 10^{-10}. \tag{39}$$

$n+{}^6\mathrm{Li}\to{}^7\mathrm{Li}^* \to \alpha + t$ ^{6}LiF will be used to line the liquid hydrogen target to absorb neutrons that don't capture. This process is dangerous because a large fraction, $\approx 30\%$, of the neutrons that originally entered the LH_2 target will be captured by ^{6}Li in the proposed geometry. $n +^6 \mathrm{Li} \to^7 \mathrm{Li}^* \to \alpha + t$. The parity violating $\vec{s}_n \cdot \vec{k}_\alpha$ correlation has been measured to be $< 6 \times 10^{-8}$ [80]. The alphas make (α, n) reactions leading to fast neutrons with a production probability of $\approx 10^{-4}$ [81]. These fast neutrons can deposit large energies, ≈ 20 MeV gamma equivalent, in the detector. We estimate the false asymmetry to be:

$$F < 0.3 \times 6 \times 10^{-8} \times 10^{-4} \times \frac{E_n}{E_\gamma} \approx 2 \times 10^{-11}, \tag{40}$$

where $E_n = 20$ MeV and $E_\gamma = 2.2$ MeV. The fraction of neutrons that capture on the ^{7}Li and the ^{19}F will be small because the capture cross sections are small, 0.16 and 0.034 barns at 2 meV as

opposed to 3.5×10^3 barns for ^{6}Li at 2 meV. We assume 10% ^{7}Li and 90% ^{6}Li. The fraction of neutrons that capture on ^{7}Li and ^{19}F are then 0.5×10^{-5} and 1.2×10^{-5}. We consider the false asymmetries from the beta decay of these polarized species below.

Mott-Schwinger Scattering of Polarized Neutrons The electromagnetic neutron spin-orbit interaction is much larger at low energies than the nuclear spin-orbit scattering: the amplitude is about 10^{-3} of the strong interaction neutron scattering amplitude for a bare nucleus. However this amplitude is imaginary, and its interference with the nuclear scattering amplitude is suppressed for most nuclei, whose nuclear scattering amplitudes are almost entirely real at low energy. Furthermore, the electromagnetic scattering amplitude is reduced at small momentum transfer (large impact parameter) by the screening of the nuclear charge by the atomic electrons. The left-right scattering asymmetry causes the beam to move left-right between the two polarization directions.

A careful calculation was performed for the hydrogen target. The calculation took into account the details of the angular dependence of the Mott-Schwinger scattering due to the differing form factors for the neutron scattering from the nuclear and electronic charge distributions, the corrections due to the shape of the molecule, and the geometry of the target and detector array. The result is an analyzing power $\approx 10^{-7}$ at a scattering angle of 45 degrees. The beam center shifts left-right by a small amount. The resulting change in the gamma ray intensity is about 10^{-8} in the left-right direction. The symmetry of the apparatus reduces this effect in the up-down direction by 10^{-2} giving a false asymmetry of 10^{-10} at 2 meV. Most of the asymmetry comes from scattering in the liquid hydrogen; the effect from the aluminum entrance window is minimal because the interaction probability is small. The time-of-flight dependence of this effect is $t^{-2.8}$.

$\vec{\mu} \cdot \nabla B$ The $\vec{\mu} \cdot \nabla B$ force can steer the neutrons up down and cause an up-down asymmetry. This effect is minimized by the use of the radio-frequency spin flipper. The 10 Gauss guide field is homogeneous from the ^{3}He polarizer and the $\vec{\mu} \cdot \nabla B$ force vanishes. For a 0.1 Gauss field change over the dimensions of the apparatus we estimate a false asymmetry of 10^{-10}. This false asymmetry depends on TOF as t. The false asymmetry changes sign when the guide field is reversed.

$\vec{s}_n \cdot \vec{k}_n$ The neutron experiences a parity violating $\vec{s}_n \cdot \vec{k}_n$ interaction as it propagates through the liquid hydrogen. Heckel estimates a spin rotation of 2×10^{-7} radians/cm. This produces a rotation of 6×10^{-6} radians in the 30 cm thickness of the target. This rotation has the same consequences as the detector asymmetry. The rotation produces a false asymmetry by coupling some left-right asymmetry into the up-down direction. We have assumed a detector asymmetry of 10^{-2} above and $6 \times 10^{-6} \ll 10^{-2}$. The parity violating longitudinal asymmetry is $\propto k_n$ and is negligible for cold neutrons. This asymmetry shifts the beam in a forward-backward direction and is rejected by the symmetry of the apparatus.

Beta Decay of Polarized Nuclei from the Capture of Polarized Neutrons The false effect from these processes arises from the parity-violating beta decay of polarized nuclei. We assume a correlation of 0.1 between the neutron spin direction and the direction of emission of the beta. The false asymmetry is reversed by a factor of fQ_β/E_γ, where Q_β is the end-point energy, f is the fraction of the beta energy converted to bremsstrahlung in the slowing down process, and $E_\gamma = 2.2$ MeV. We take this fraction from ref. [79]. The time structure of the beam and the relaxation of the nuclear

spin reduce the asymmetry by a factor:

$$g = \frac{T}{\tau}\frac{1/2 - 1/4(a - a^{3/2} + 2a^4)}{1 + a}, \tag{41}$$

where T is the time width of the cold neutron pulse ($\approx$ 10 ms), and τ is the beta decay lifetime. If D is the time between macro pulses (50 ms) and ρ is the spin relaxation time (assume $\rho \gg T$), then we can write a, the decay of the spin due to decay and depolarization between macro pulses as $a = e^{-D(1/\tau + 1/\rho)}$. g varies between $T/2\tau$ and $3T/16\tau$ as a varies between 1 and 0, as shown in figure 20. We estimate the false asymmetries produced by the polarized neutron beam interacting

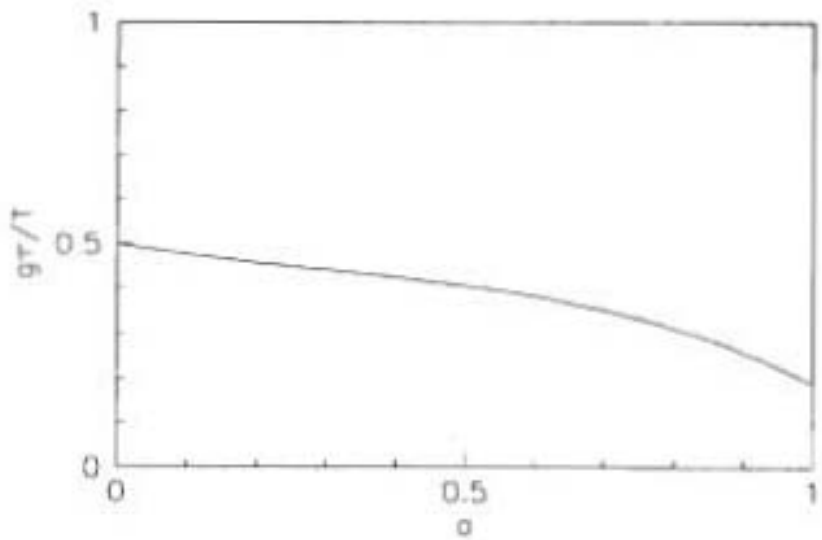

Figure 20: Variation in $g\tau/T$ as a function of a.

with 0.1 g/cm^2 of various materials. In the case of the LiF liner, we assume that 1/4 of the neutrons interact. For a sequence of isotopes such as ^{12}C and ^{13}C only the heaviest isotope has to be considered and the false asymmetry is reduced by the fractional abundance of this isotope. Carbon is a great material because the ^{14}C daughter has $J = 0$ and hence has no beta decay asymmetry. Furthermore, the false asymmetries are small because capture cross sections are small.

From the estimates presented here, it is clear that false asymmetries from the capture of polarized nuclei will not produce serious false asymmetries as can be seen from table 4.

4.2.3 Time-Dependent Effects

Time-dependent systematic effects arise from drifts or fluctuations in experimental parameters such as detector gain, incident flux, and beam position on the target. The primary technique for reducing

	^{27}Al	^{25}Mg	^{7}Li	^{19}F	^{18}O	^{96}Zr	^{208}Pb
Abundance	1	0.11	0.1	1	0.002	0.03	0.52
Daughter	^{28}Al	^{27}Mg	^{8}Li	^{20}F	^{19}O	^{97}Zr	^{209}Pb
Mean Life (s)	138	570	0.84	11.4	29	6.1×10^{4}	1.2×10^{4}
g	1.4×10^{-5}	3.2×10^{-5}	2.7×10^{-3}	1.7×10^{-4}	6.5×10^{-5}	4.1×10^{-7}	1.6×10^{-7}
$\sigma_{capture}$ (b)	0.85	0.13	0.16	0.034	5.7×10^{-4}	0.08	1.1×10^{-2}
Q_β (MeV)	4.6	1.8	16.0	7.0	3.5	2.65	0.64
Fraction	1.9×10^{-3}	3.3×10^{-5}	1.1×10^{-5}	1.2×10^{-5}	4.3×10^{-9}	5.0×10^{-5}	1.7×10^{-6}
F_{rad} $(E_\beta/2)$	2.0×10^{-2}	8.9×10^{-3}	3.1×10^{-2}	1.4×10^{-2}	9.4×10^{-3}	4.1×10^{-2}	3.8×10^{-2}
$E_\beta F_{rad}/4.4$ MeV	2.1×10^{-2}	3.6×10^{-3}	0.11	2.2×10^{-2}	7.5×10^{-3}	2.5×10^{-2}	5.5×10^{-3}
F	5.6×10^{-10}	2.1×10^{-14}	1.4×10^{-10}	2.6×10^{-11}	1.1×10^{-16}	5.1×10^{-13}	7.8×10^{-16}

Table 4: Properties of nuclei that can contribute to false asymmetries by beta decay after capturing polarized neutrons. The isotope that gives the largest false asymmetry is shown.

the false asymmetries generated by these changes is fast spin reversal. This allows asymmetry measurements to be made in each neutron spin state very close together in time, before significant drift occurs. In addition, by carefully choosing the sequence of spin reversal, the effects of any remaining drifts can be further reduced. We plan to reverse the neutron beam polarization at 20 Hz; that is with each beam pulse. The optimal spin-reversal sequence depends upon the specific characteristics of the largest systematic drifts and has yet to be determined. We will describe one possible sequence.

The importance of the spin reversal sequence can be illustrated by considering an efficiency difference between up and down detectors that drifts linearly with time, such that the difference is positive and increasing. If the neutron spin is simply alternated between the two states $\uparrow\downarrow\uparrow\downarrow\ldots$, the second state will always have a larger asymmetry, leading to a false effect. However, if the four-step sequence $\uparrow\downarrow\downarrow\uparrow$ is chosen instead, the effect is canceled. Carrying the process one step further gives the eight-step sequence $\uparrow\downarrow\downarrow\uparrow\downarrow\uparrow\uparrow\downarrow$, which cancels time-ordered drifts to quadratic order [82].

A more realistic example is a spin-independent false asymmetry that has an exponential time dependence $\varepsilon = Ae^{-t/\tau}$. We take for amplitude $A = 1 \times 10^{-5}$ and for the time constant $\tau = 100T$, where T is the time between spin states. These parameters reflect reasonable values for slowly drifting systematic effects. This false asymmetry is greatly reduced by taking the difference between asymmetries measured with positive and negative neutron spin directions, but the size of the reduction depends strongly on the spin-flip sequence chosen. We will consider three different sequences, consisting of eight asymmetry measurements, four for each neutron spin direction: 1) the two-step sequence $\uparrow\downarrow\uparrow\downarrow\uparrow\downarrow\uparrow\downarrow$, the four-step sequence $\uparrow\downarrow\downarrow\uparrow\uparrow\downarrow\downarrow\uparrow$, and the eight-step sequence $\uparrow\downarrow\downarrow\uparrow\downarrow\uparrow\uparrow\downarrow$. The results, summarized in table 5, clearly show that for this type of systematic drift the eight-step sequence is superior.

The most important time-dependent systematic effects arise from drifts in detector efficiencies. This is because differences in detector efficiency are the origin of the largest time-independent systematic asymmetry, which is of order 10^{-2}. To the extent that this effect is constant with time, it is removed by reversing the neutron spin. Thus, it is only the time-dependent drifts that can cause a false effect. We divide the detector drift into two components: an intrinsic term, which is independent of environmental conditions and a temperature-dependent term. Both have been measured by Frlez, *et al.* [70] for similar detectors, who report coefficients of 1% per week for intrinsic drift and 1% per degree C for temperature-dependent drift.

Spin Sequence		Asymmetry
Two-Step	↑↓↑↓↑↓↑↓	4×10^{-7}
Four-Step	↑↓↓↑↑↓↓↑	4×10^{-9}
Eight-Step	↑↓↓↑↓↑↑↓	8×10^{-11}

Table 5: False asymmetry due to an exponentially decaying signal for three neutron spin-flip sequences. The signal has an initial magnitude of 1×10^{-5} and a time constant of 100 times the spin-flip interval.

We can then estimate the systematic asymmetries from these effects by assuming the drifts are exponential and uncorrelated between different detectors. We note here that correlations tend to reduce the size of the effects. We further assume a maximum rate of temperature change of 1 degree C per hour. In the case of an eight-step sequence with a spin-flip rate of 20 Hz, this estimate gives a false asymmetry of 2×10^{-22} for the intrinsic term and 2×10^{-15} for the temperature-dependent term, well below our expected statistical uncertainty.

4.3 Online Diagnostics

4.3.1 Identification of Systematic Effects: TOF Dependence and Target Depolarization

At a pulsed neutron source, there is a relation between the arrival time of the neutron after the proton burst strikes the target and the neutron energy: $E \propto 1/t^2$. The relation between the neutron energy and the timing of the gamma ray signal is blurred somewhat by the distribution of moderation times of the neutrons in the cold moderator and the hydrogen target (which averages about 100 μs), but this effect is small in comparison to the arrival times of the low energy neutrons of interest (of order a few milliseconds). Therefore the time dependence of the gamma ray signal can be correlated with the incoming neutron energies.

The parity-violating analyzing power A_γ in $\vec{n} + p \rightarrow d + \gamma$ is energy independent for low energy neutrons. If there were no depolarization of the neutrons in the para-hydrogen target, the time dependence of the parity-violating asymmetry would result only from the time dependence of the neutron polarization. As noted in the introduction of section 3, however, neutrons with energies above 15 meV are strongly depolarized before they capture. The time dependence of the parity-violating asymmetry should therefore follow the time dependence of the beam polarization for long time-of-flight, corresponding to neutrons with $E \leq 15$ meV, but decrease significantly for shorter time-of-flight, corresponding to neutrons with $E \geq 15$ meV.

Both of these features, the time dependence of the asymmetry and the energy dependence of the neutron depolarization, are very useful for isolating and identifying systematic effects. Different systematic effects possess different dependences on neutron energy. For example, a systematic effect associated with neutron beam motion due to the Stern-Gerlach effect in the gradient magnetic field grows as the square of the time spent in the field gradient, and thus increases as a function of time-of flight. On the other hand, a systematic effect from Mott-Schwinger scattering grows with incident neutron energy and therefore decreases with time-of-flight. Each systematic effect has a characteristic time signature that can be used as a partial means of identification, and most of these time signatures are different from that expected from the true asymmetry.

The neutron depolarization above 15 meV not only effectively turns off the parity violating signal: it also must turn off all systematic effects that require the neutrons to be polarized in the para-hydrogen target. For example, Mott-Schwinger scattering effects in para-hydrogen, bremsstrahlung from parity-violating beta decay of ^{7}Li formed from polarized neutron capture in the target liner, and the parity-conserving asymmetry must vanish above 15 meV. On the other hand, systematic effects not associated with hydrogen, such as Mott-Schwinger scattering and bremsstrahlung from parity-violating beta decay of window materials before the target, will still be present at neutron energies above 15 meV.

The combination of these diagnostics is an important tool for identifying sufficiently large systematic effects that either have been overlooked or underestimated in our analysis. We have indicated in the systematic effects section both the expected time dependence of the systematic effect and whether or not it turns off as the neutrons are depolarized in the target above 15 meV.

4.3.2 Target Diagnostics

Two properties of the target must be ensured. It is essential that the ortho-hydrogen content in the target remain small, to minimize neutron depolarization before capture. In addition, it is important to verify that the neutron polarization upon capture in the target behaves as expected in order to make full use of the time-of-flight diagnostic technique for systematic effects described above.

There are two convenient ways to monitor the ortho-para ratio of the target. For a 20 K liquid hydrogen target held at atmospheric pressure the equilibrium concentration of para-hydrogen is 99.8%. This concentration can be measured with a gas thermal conductivity cell. One measures the resistivity change of a wire in thermal contact with the gas. The technique exploits the significant difference between the thermal conductivities of ortho and para hydrogen gas [83, 84]. The measurement accuracy of this technique is about 0.4%. This method suffers from possible changes in the ratio due to conversion on the tube walls during extraction of the gas. In addition, it may not be compatible with the safety requirements for the target.

Another solution is to allow a fraction of the forward scattered neutrons in the target to escape the ^{6}Li neutron shielding and reach a beam monitor behind the target. The beam monitor can be used to see changes in the relative concentrations of ortho-hydrogen and para-hydrogen in the target (and in the neutron cold source). This is possible due to the very large difference in neutron cross sections for the two species at low neutron energies (see figure 21). At 4 meV neutron energy, for example, the ortho-hydrogen cross section is larger than the para-hydrogen cross section by a factor of about 20. Furthermore, this cross section ratio changes as a function of energy in a known way in our energy regime. For a small change in the ortho-hydrogen concentration of the target, the fractional change in transmission is therefore larger (by the same factor) than an equivalent change in the target density. Doubling the 0.2% equilibrium ortho-hydrogen concentration in the target, for example, leads to a 10% decrease in the transmission at 4 meV. This monitoring method is more direct and is completely compatible with liquid hydrogen safety requirements. The transmission method is sensitive to ortho-para changes in the cold moderator as well. Changes in the efficiency of the cold moderator are expected to be smaller for a given change in ortho concentration than changes in the para-hydrogen target transmission. We will verify this expectation with empty-target measurements soon after the cold moderator is operational. Once the steady-state properties of the moderator and target are established, a time-independent transmission spectrum is sufficient verification that the ortho concentration is acceptable.

The appropriate beam monitor for this task would need to possess an efficiency with known

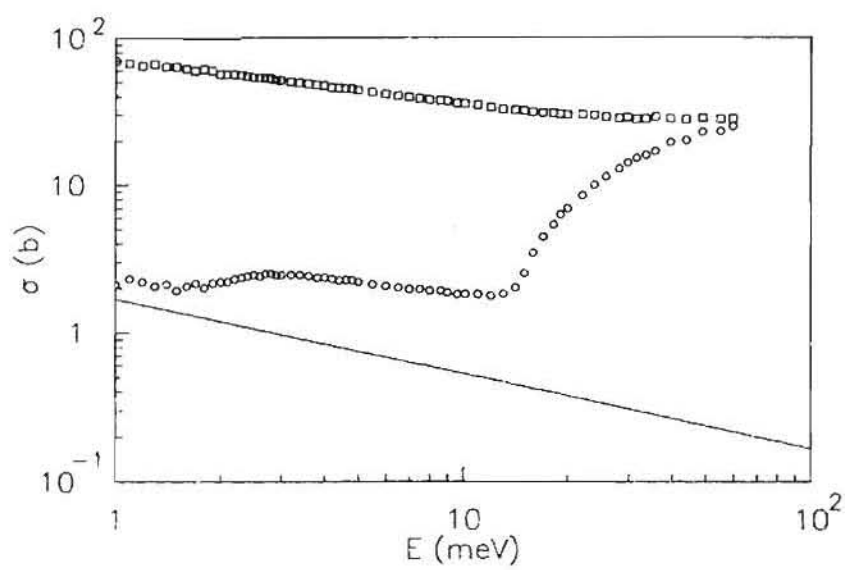

Figure 21: Measured scatt ng cross sections for neutrons on para-hydrogen (circles) and neutrons on normal (75% ortho-) hydrogen (squares). The solid line is the cross section for n–p capture. [85].

energy dependence. The two practical ways to achieve this goal for low energy neutron beams are

1. to use a "thin" detector and exploit the $1/v$ dependence of neutron absorption cross sections, and

2. to use a totally absorbing detector.

In the latter case current mode detection may be required due to the high rates. A low Z target is also preferred to reduce sensitivity to the intense gamma flash from the spallation burst and to capture gammas from the source. Such a beam monitor has already been developed by the TRIPLE collaboration [86]. It is a dual ion chamber with ^{3}He and ^{4}He as the working gases. The signals from the two ion chambers are subtracted to remove the gamma-induced component of the signal.

Information on the neutron polarization before capture is more difficult to obtain experimentally. The ideal approach would be to introduce a liquid that depolarizes neutrons in the same way as para-hydrogen and possesses a nuclear species with a large parity-violating asymmetry. ^{35}Cl possesses a parity-violating gamma asymmetry integrated over the neutron capture gamma spectrum of 2×10^{-5} [87], which is large enough to collect counting statistics in a short time. Cl is a component in several room-temperature liquids. No liquid containing this $I = 3/2$ species will reproduce the full energy dependence of neutron depolarization produced in the para-hydrogen target, however. To the extent that the depolarization could be calculated for some liquid with ^{35}Cl, it would certainly be useful as a demonstration of the techniques described above.

The polarization of the neutrons leaving the target carries some information on the energy dependence of the depolarization process. One can analyze the polarization of forward scattered neutrons as a function of energy using a polarized ^{3}He analyzer and a transmission detector. Similar measurements have recently been performed at LANSCE in an effort to determine the absolute neutron beam polarization produced by a polarized ^{3}He target [88]. Only a relative transmission measurement is required [40]. This measurement would give a upper bound as a function of energy on the neutron polarization before capture. In addition, such a measurement can be used as a check on a theoretical calculation of the depolarization.

4.4 Auxiliary Measurements

Auxiliary measurements to test for and limit possible systematic errors can be divided into two broad classes. The first class are those measurements done "on-line", that is, while $\vec{n} + p \rightarrow d + \gamma$ data is being acquired.

Because of the geometrical suppression expected by the left-right and up-down symmetries of the detector, any observed left-right current asymmetry (expected to be 2×10^{-9} due to a parity conserving n–p interaction, see section 4.2.2) can be divided by 100 to get the possible contamination to the up-down (parity) current change correlated with the neutron spin reversal.

It will also be important to determine whether there is any change in neutron trajectory correlated with the spin flipper operation. Such a trajectory change could give a false parity signal because the gammas created by the neutron capture will have a spatial distribution, hence a different solid angle at each detector. The change in count rate R between the two detectors, for a point source located between them at a distance d from each, is given by the change in solid angle $\Delta\Omega$ to each detector:

$$\Delta R \propto \Delta\Omega \propto \frac{1}{(d-\delta)^2} - \frac{1}{(d+\delta)^2} = \frac{4\delta}{d^3} \tag{42}$$

or a fractional change of

$$\frac{\Delta R}{R} = \frac{4\delta}{d}, \tag{43}$$

which is a first order change in a small transverse displacement δ. Such an effect can be isolated by appropriate reversals of the polarizer and guide fields. This effect can also be measured by increasing the distance from the spin flipper to the target, although this will likely result in reduced statistical accuracy because of neutron loss due to beam divergence.

The trajectory change can be determined with better accuracy by use of an off-line measurement; if a knife edge is placed in the neutron beam a long distance from the flipper, any net trajectory change will be evident by a change in count rate. In fact, if the guide field terminates somewhere near the flipper (normally the hydrogen target is placed in the guide field), as the neutrons leave this field, they will experience a transverse force that should be easily evident by a change in the knife-edge detector count rate. The limit on a possible spin-correlated systematic can be readily determined by the appropriate length and magnetic field change scalings.

Effects of spin-correlated bremsstrahlung from neutron capture beta decay can be amplified by a large amount. For example, the liquid hydrogen target can be substituted with a large solid aluminum slug, in which case a systematic signal correlated with, for example, the hydrogen vessel input window could be amplified by a factor of 100,000. In fact, any material, used in the construction of the apparatus and that comes in contact with polarized neutrons, could be tested in this manner.

Systematic changes in system gain correlated with operation of the spin flipper can be discriminated by an appropriate flip sequence. However, any such effect could be directly tested by blocking the neutron beam and setting the photo-detector currents to their operating value by exposing them to a weak constant light source. The shot noise associated with this current would be an order of magnitude less than that from the neutron gamma capture photo-current.

Similarly, the change in background and pickup associated with operation of the spin flipper can be easily determined by blocking the neutron beam and measuring the dark current correlation.

Finally, the system can be calibrated by substituting the liquid hydrogen target with a material with a large and well-know capture gamma ray asymmetry; an excellent candidate is carbon tetrachloride. The gamma asymmetry for polarized neutron capture on ^{35}Cl is approximately 2.5×10^{-5}; a cell containing one cold neutron mean free path (about 1 cm) of this material could be used to accurately test and calibrate the apparatus in a few minutes of running.

5 Progress to Date

5.1 Test Run

A proof-of-principle test run has been performed using unpolarized thermal neutron capture on polyethylene. This arrangement was selected as it produces approximately the same rate of 2.2 MeV gammas as we expect in the actual experiment. The primary purposes of this test were to verify that the electronic noise of the detector system can be reduced below the quantum fluctuations in detector current from counting statistics, and to measure the sensitivity of the detector efficiencies to magnetic fields. For the test an array of 12 CsI detectors similar to what will be used in the actual experiment was used.

In the test experiment, a 15 cm diameter by 5 cm thick target of polyethylene, supported by a cylindrical polyethylene shell, was placed in a 10 cm diameter neutron beam. The 12 CsI detec-

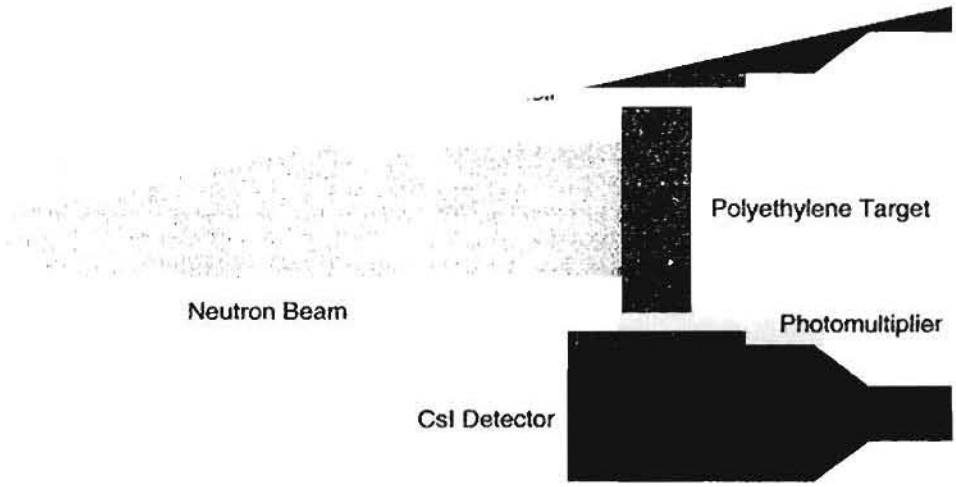

Figure 22: Experimental arrangement for the test experiment, showing the neutron beam, polyethylene target, and CsI detectors.

Two different electronic configurations were tested. In the first, only two individual phototubes were connected to low-noise preamplifiers attached directly to the phototube sockets. The amplified signals then went to a NIM module that formed sum and difference signals. This arrangement was used to measure the electronic noise and is similar to the design of the actual measurement, where each photocathode will have an individual amplifier. In the second configuration, the detector photocathodes were connected together in two groups of six. These two signals then went to external preamplifiers and then to the sum and difference amplifiers, as described above. This arrangement was used to study fluctuations in the capture gamma flux, due to effects such as beam intensity and position modulations. With this arrangement, we could measure the spectral density of the beam noise.

The detector electronics used for the noise measurements are shown in figure 23. The circuit consists of two low-noise current-to-voltage (IV) amplifiers, followed by stages that take the sum and difference of the two voltages. The IV amplifiers where designed using AD745A op-amps. These op-amps have a typical voltage noise density of 2.9 $nV/\sqrt{Hz}$ and a typical current noise density

of 6.9 fA/$\sqrt{\text{Hz}}$ at 1 kHz. The 10 MΩ feedback resistor gives a DC gain of 10 V/μA. A 10 pF feedback capacitor combined with an external low-pass filter limit the 3 dB bandwidth to 3.0 kHz. This corresponds to a time constant of approximately 50 μs. Precision resistors (0.1%) with low temperature coefficients (20 ppm/°C) are used in the IV, sum, and difference amplifier stages. The sum circuit was designed to have an overall gain of 10 V/μA, and the difference circuit a gain of 1.0 V/nA. The spectral density measurement, used the same circuit with the preamplifier gain reduced by a factor of 50, and the bandwidth increased to 160 kHz.

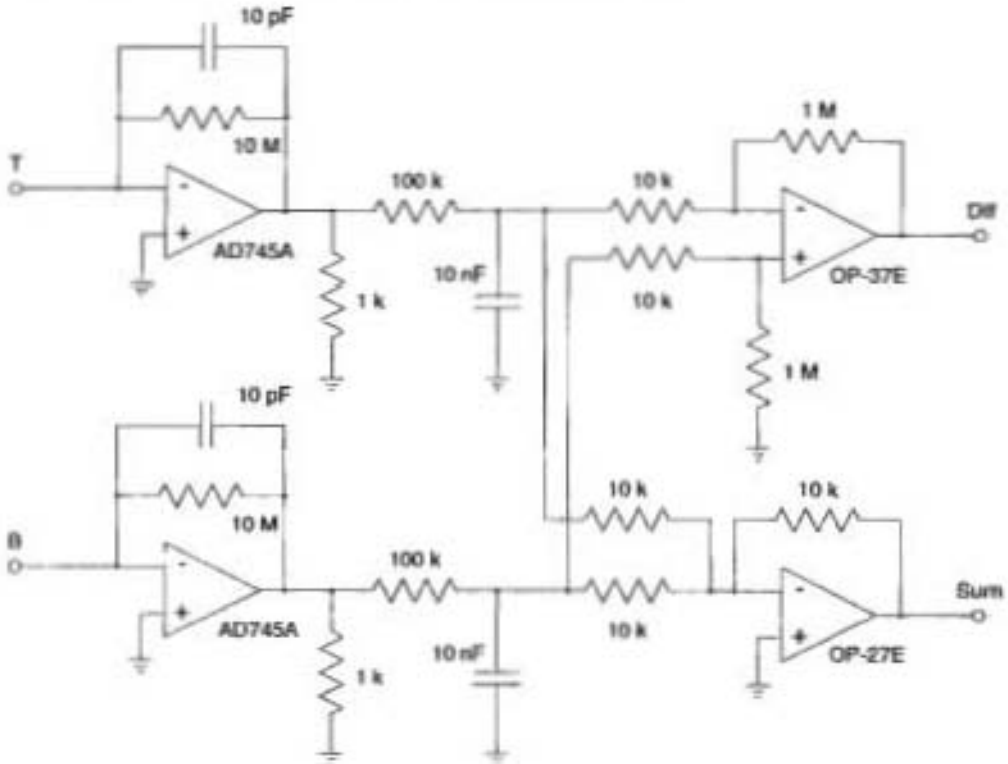

Figure 23: Diagram of the detector front-end electronics for the test experiment.

5.1.1 Current-Mode Signal

Several measurements were performed to ensure that the observed detector current for the full array, 0.56 μA for 1 eV neutrons, was consistent with calculations based on neutron capture gamma rays from hydrogen in the polyethylene target. This number is the product of the neutron flux, the probability for the neutron to capture on a proton, the probability that the capture produces

a gamma ray that absorbs in the detector, and the charge per gamma ray that appears at the photocathode. The instantaneous flux of 1 eV neutrons on the target could not easily be measured directly. Instead, a flux of $5 \times 10^{10}\ s^{-1}$ was inferred from a measurement of the count rate in a totally-absorbing ^{6}Li scintillator, 1 cm in diameter, located 56 m from the spallation target. At this location and neutron energy the count rate, 10.8 kHz, was low enough to use normal pulse-counting methods.

A Monte Carlo calculation was performed to estimate the fraction (approximately 60%) of incident neutrons that capture on protons in the polyethylene target after moderation. Most of the remaining neutrons backscatter from the target. The mean transport path for thermal neutrons in polyethylene used in the calculations, 5 mm, was verified by relative transmission measurements. The prediction for the amount of backscattered neutrons was tested by moving the location of the target relative to the detector array and observing that the target position that gave the largest detector signal was located about 6 cm downstream from the center of the detector annulus. The large size of the signal at this position, about 2.5 times larger than the signal for the target centered on the array, was attributed to backscattered neutrons that capture on the protons in the cylindrical polyethylene support structure for the target (gamma rays from the support are closer to the detectors and have a larger solid angle).

Since the solid angle was known, the only remaining quantity needed to calculate the detector current is the number of photoelectrons produced in the CsI detector's photocathode by the 2.23 MeV gamma ray. This number was determined by two independent methods. First, the polyethylene target was replaced by a totally-absorbing In target. Indium possesses a large neutron resonance at 1.46 eV, which decays primarily by gamma emission. Using the measured detector current at the resonance, we inferred a value of 70 photoelectrons per MeV of deposited gamma ray energy. This number was consistent within errors with the value of 65 photoelectrons per MeV inferred from previous measurements of the energy resolution of the CsI detectors for the gamma rays from a ^{60}Co source. The number of photoelectrons per MeV was calculated under the assumption that the energy resolution is dominated by the statistical fluctuations of the number of photoelectrons.

Based on this combination of measurements and simulations, the predicted detector current for the full array is about $0.5 \pm 0.1\ \mu$A for 1 eV neutrons. The agreement with the measured value of $0.56\ \mu$A has two consequences: 1) the current mode signal is indeed dominated by gamma rays from neutron capture on protons, 2) the value for the number of photoelectrons per MeV in the detector is determined. This value is needed to calculate the expected amount of noise in the detector array due to current shot noise from neutron counting statistics.

5.1.2 Electronic Noise

Using a digital oscilloscope, the electronic noise was measured for the sum and difference outputs. The noise in the sum output was $760\ \mu V_{rms}$. Referred to the input, this corresponds to $1.4\ pA/\sqrt{Hz}$. The difference output had $110\ \mu V_{rms}$ of noise, corresponding to $0.2\ pA/\sqrt{Hz}$ at the input. It is useful to compare the difference noise to the rms shot noise created by the quantized nature of the expected detector signal

$$I_{sn}/\sqrt{f} = \sqrt{2qI}, \qquad (44)$$

where q is the charge generated in the photocathode per gamma and I is the photocathode current. Using the expected values $q \approx 150e$ and $I \approx 100$ nA, we obtain $I_q/\sqrt{f} \approx 2\ pA/\sqrt{Hz}$, a factor of 10 greater than our electronic noise. Calculations with a SPICE model of the preamplifier indicate that

an electronic noise of just 13 fA/$\sqrt{\text{Hz}}$ should be obtainable. We attribute the excess noise observed in our test to be from 60 Hz pickup. This contribution will be reduced with improved electrostatic shielding. More progress has been made on reducing the preamplifier noise since the test run (see section 5.2). In addition, the CsI(Tl) detectors that will be used in the experiment will produce approximately 500 electrons per gamma, which will also improve the ratio of electronic noise to statistical fluctuations.

5.1.3 Spectral Density

Periodic variations in beam parameters can produce false asymmetries. These effects include fluctuations in beam intensity and position, which are expected to dominate over other terms. Because of this, the experiment has been designed so that these terms do not contribute to a false asymmetry in first order. Since the experimental asymmetry is formed by taking the difference between up and down detector currents, the two currents are measured simultaneously, making the apparatus quite insensitive to incident flux variations. Second, the azimuthal symmetry of the apparatus suppresses the contribution from beam motion. While such effects do not lead directly to false asymmetries, it is possible for them to contribute in higher order. For example, beam motion combined with detector-efficiency differences can give a non-zero effect. For this reason, it is important to know the size of the fluctuations in beam parameters.

We measured the influence of these fluctuations on the detected signal and set an upper limit for their contribution. We sampled the difference signal from the detectors every 50 ms for a 20 minute period while the spallation source operated in a steady-state mode. This was done by integrating the voltage for 1 μs every beam pulse The autocorrelation function of the difference signal, $f(\tau) = \langle i(t)i(t-\tau)\rangle$ was then calculated. The Fourier transform of this quantity, $F(\omega) = \int_{-\infty}^{+\infty} f(\tau)e^{i\omega\tau}d\tau$, is the spectral density of the intensity fluctuations of the neutron source as filtered through the difference signal of interest. There were no periodic sources of noise observed in the 0–10 Hz range (fig. 24). The upper limit of this range is set by the sampling rate, which is in turn limited by the pulse spacing. Because the signal bandwidth (160 kHz) was larger than this upper observable frequency, the noise above 10 Hz is aliased into the 0–10 Hz range. Correcting for this effect, we estimate an upper limit of 5 fA/$\sqrt{\text{Hz}}$ on beam-induced fluctuations on the difference signal.

5.1.4 Detector Sensitivity to Magnetic Fields

The sensitivity of the detectors to magnetic fields was measured by applying a 10 G magnetic field to the detectors using a pair of Helmholtz coils and reversing the field at 0.1 Hz. The field was oriented parallel to the photocathode surfaces of the photomultiplier tubes in an attempt to maximize the size of the effect. The observed change in the detector efficiency was 2×10^{-5} G^{-1}. This is about five orders of magnitude smaller than one would expect for a typical photomultiplier tube operated in the normal fashion with high voltage on the dynodes.

5.2 Development of the Detector Electronics

As discussed in section 5.1, the development of low-noise electronic amplification of the detector photo-cathode signals is crucial to the success of the experiment. Fortunately, we have succeeded in designing and testing op-amp based current-to-voltage preamplifiers that exhibit approximately 250 times less noise than expected from the actual signal. The performance of the preamplifiers was

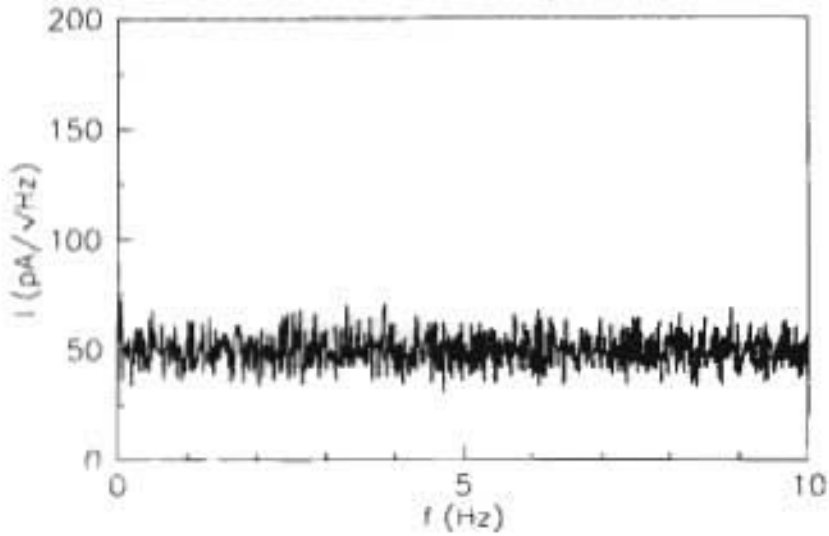

Figure 24: Spectral density of the detector difference signal, due to fluctuations in the neutron beam parameters.

verified in the test run, and further improvements were then made in bench tests. A two-channel prototype sum and difference amplifier set was used for these tests.

In the test run, the electronic noise was measured to be 0.2 pA/$\sqrt{\text{Hz}}$ at the input. This is a factor of 8 smaller than the rms shot noise corresponding to counting statistics at the lowest neutron flux. Further improvements since the test run, primarily from improved electrostatic shielding, have reduced the current noise density to just 20 fA/$\sqrt{\text{Hz}}$ (figure 25), a factor of 250 smaller than the signal shot noise.

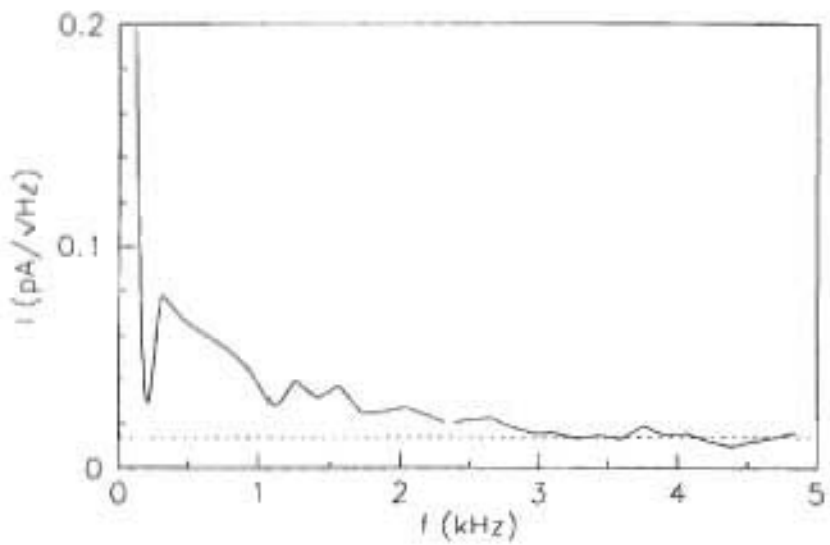

Figure 25: Current noise density measured from the current-to-voltage preamplifier and referred to the input. The dashed line indicates the level of noise from the measurement apparatus. The frequency response of the preamplifier was externally limited to 3 kHz. Note that the large value at zero frequency corresponds to the DC signal.

5.3 Computer Modeling

5.3.1 Neutrons in the Liquid Para-Hydrogen Target

We have modeled the transport of the neutrons in a liquid para-hydrogen target using both MCNP and a home-written code. The scattering kernel reproduces the measured dynamic structure factor $d^2\sigma/d\Omega\, dE$ of liquid para-hydrogen where it has been measured [89]. These calculations seek to determine

1. what are the optimal dimensions of the hydrogen target, and

2. how quickly do the neutrons depolarize in the target at incident energies ($\geq$ 15 meV) that are high enough to excite the para-hydrogen molecule.

The target dimensions can be estimated from the need to stop and capture neutrons of a few meV kinetic energy. The neutron transport in the target can be thought of as being composed of two steps: first the neutrons reach equilibrium with the target, and then they diffuse in the target until they escape or capture. We can perform a crude estimate as follows. The mean free path $l = 1/n\sigma_s$ for 4 meV neutrons in para-hydrogen is about 9 cm, and one expects the average number of collisions before capture, $N = \sigma_s/\sigma_a$, to be about 2.5 for 4 meV neutrons. σ_t, σ_s, and σ_a are the total, scattering, and absorption cross sections. The mean distance to capture is therefore $l\sqrt{N} = 14$ cm. However, this estimate does not include all of the dynamics of the process, such as the angular dependence of the scattering and the energy transfer. To obtain an estimate including these factors, we performed Monte Carlo calculations. The results of the calculation show that a target with a radius of 30 cm and a length of 30 cm is sufficient to capture 60% of the incident neutrons.

The average scattering angle as a function of incident neutron energy is shown in figure 26. Monte Carlo simulations show that above 10 meV the average scattering angle varies from 75–60 degrees as the energy increases. Figure 26 also shows the average energy loss for the initial scattering event as a function of incident neutron energy. Above 10 meV, the incident neutron loses on average 3/4 of its initial energy in the first collision.

In order to understand the implications of these results, it is convenient to divide the neutrons into two classes: those above 15 meV and those below 15 meV. Refer to figure 21, which shows the energy dependence of the neutron scattering and absorption cross sections in para-hydrogen. After 1–2 collisions the average energy of the neutrons is below 15 meV. When this state is reached the kinetic energy of the neutron is not far from that of the molecules in the target, and so one expects the neutron motion to become isotropic. Below 15 meV the average number of scatterings before capture is similar, and it varies slowly as a function of neutron energy for the range of incident neutron energies in the beam. We therefore expect that we will need to make the target about twice as long along the beam direction as it is wide due to this "free streaming" of the beam in the forward direction prior to the first scattering.

Figure 27 shows the fraction of incident neutrons that produce capture gammas in a cylindrical target as a function of target dimensions. We assume a 10 cm $\times$ 10 cm beam with the expected energy distribution from the planned LANSCE cold moderator. About 60% of the incident neutrons capture in the hydrogen. Given the slow rate of increase of the capture efficiency of the target with increasing size, we have settled on a 15 cm radius and a 30 cm length as the design dimensions for the target. Of the neutrons that do not capture in the target, about 10–15% backscatter or diffuse out the front of the target, 5% are transmitted, and the rest leak out radially. These results for the fraction of neutrons that capture in the target are consistent with the experience of the previous attempt to measure parity violation in $\vec{n} + p \rightarrow d + \gamma$ performed at the ILL [10].

The issue of neutron depolarization can be discussed qualitatively as follows. As mentioned above, the ground state of the hydrogen molecule, para-hydrogen, has $J = L = S = 0$, and the first excited state, ortho-hydrogen, is at 15 meV. Neutrons below this energy cannot excite the para-hydrogen molecule so only elastic scattering is allowed, and spin-flip scattering is forbidden. The neutron polarization therefore survives the scattering events that occur before capture. (In fact, there is a small amount of depolarization due to the presence of ortho-hydrogen and deuterium impurities: we estimate that one retains 98% of the incident polarization if one assumes a 0.2% ortho-

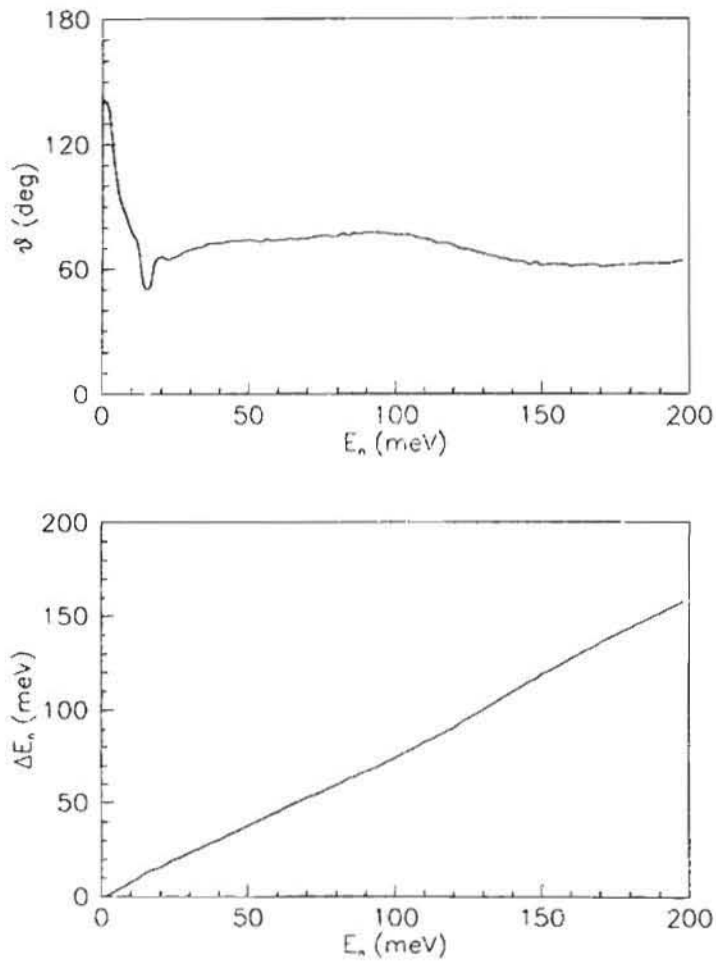

Figure 26: Monte Carlo calculation of the average scattering angle (top) and average energy loss (bottom) of neutrons in para-hydrogen as a function of neutron energy.

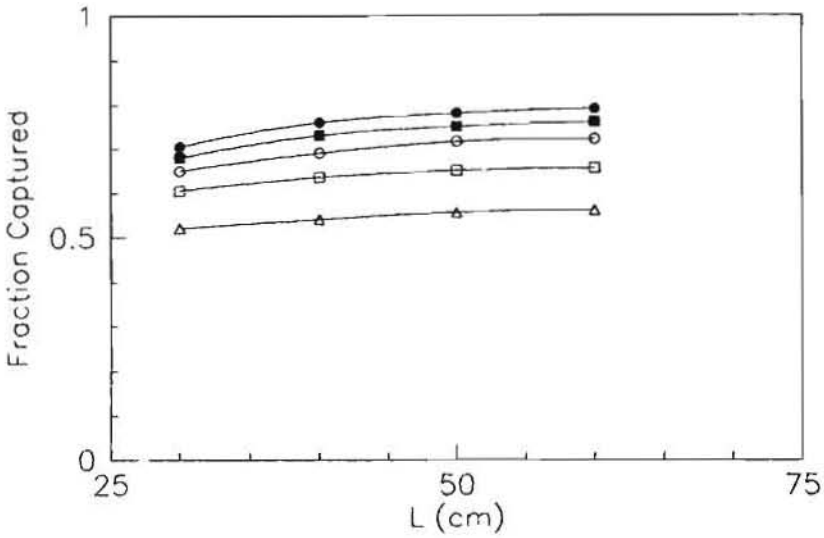

Figure 27: Monte Carlo calculation of the fraction of neutrons producing capture gamma rays in the para-hydrogen target for target radii of 10 (open triangle), 15 (open square), 20 (open circle), 25 (filled square), and 30 cm (filled circle).

hydrogen concentration. There will also be a small amount of depolarization from the deuterium impurities in the target). Higher energy neutrons will undergo spin-flip scattering and will depolarize. We therefore expect the neutron polarization before capture to be high below 15 meV and to fall sharply above 15 meV as spin-flip scattering becomes possible.

A complete calculation of the spin-flip scattering probability of a polarized neutron from a hydrogen molecule must take into account all of the details of the rotational dynamics of the molecule in the liquid and is rather involved. However, we can perform a calculation that sets an upper limit on the ratio of the spin-flip scattering to the total scattering as follows. It is easy to derive the following expression for the cross sections for spin-flip and no-spin-flip scattering from a single isolated nucleus [90]: $\sigma_{noflip} = \sigma_c + 1/3\sigma_i$ and $\sigma_{flip} = 2/3\sigma_i$ where σ_c and σ_i are the coherent and incoherent neutron scattering cross sections. When coherent scattering is dominant, the depolarization is small. When incoherent scattering is dominant, as it is for the higher energy neutrons on hydrogen, the beam is quickly depolarized.

We have performed a Monte Carlo calculation of the neutron polarization upon capture as a function of incident neutron energy for this extreme case. The results are seen in figure 28. The results can be understood as follows. The neutrons with energy greater than 15 meV, which are susceptible to depolarization quickly (within 1–2 collisions), lose enough energy that their kinetic energy falls below 15 meV, where they are safe from further depolarization before capture. In the incident energy range from 15–50 meV, the neutrons undergo one scattering event that brings their energy below 15 meV, and so the final polarization upon capture is close to the theoretical extreme of $-1/3$, that is, the polarization decreases and is reversed. At higher energies where one gets on average two scattering before falling below 15 meV, the polarization is positive again and down by another factor of $1/3$.

This crude estimate effectively treats the atoms in the molecule independently and so is expected to be accurate only for higher energy neutrons. It will fail in the intermediate energy region, and more sophisticated calculations need to be performed. We intend to pursue an approximation in that only the effects of the $L = 0, S = 0$ to $L = 1, S = 1$ para-ortho transition is taken into account, since it is the dominant feature in the rise in the scattering cross section above 15 meV. We will use the free rotor approximation for liquid hydrogen (the Young-Koppel model) in this estimate. It is important to verify the understanding of the depolarization mechanism by analyzing the transmitted neutron polarization behind the hydrogen target.

5.3.2 Modeling of CsI Detector Array

The goals for the modeling of the gamma detector array are

1. to calculate the acceptance,
2. to model the electron-photon shower and determine its relevant properties,
3. to determine for each detector the average fraction of energy that is deposited and the fluctuations in this average.

Our proposed segmented gamma detector contains 48 cubes of CsI, 15 cm × 15 cm × 15 cm. The 15 cm thickness corresponds to 3 mean free paths for 2.2 MeV gamma rays. Figure 17 shows the arrangement of the crystals relative to the central volume of the liquid hydrogen target. We have calculated the fraction of gammas from the target that are stopped in the array using the MCNP

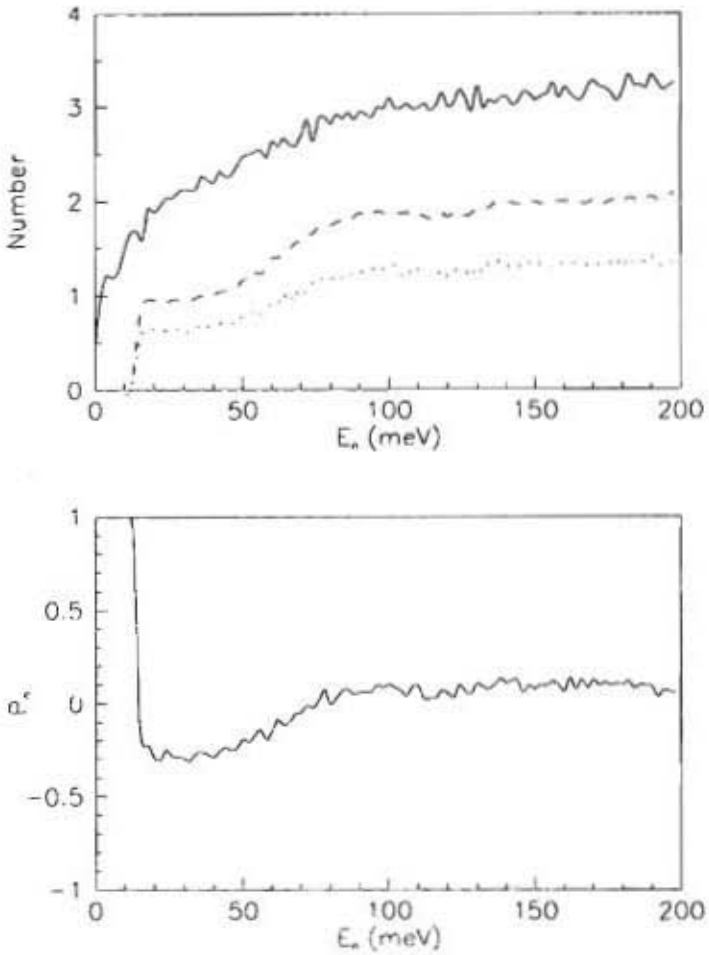

Figure 28: The top panel shows a Monte Carlo calculation of the average number of neutron scatterings before capture (solid), scatterings with final $E_n > 15$ meV (dashed), and scatterings that cause neutron spin flip (dotted) The bottom panel shows a Monte Carlo calculation of the average neutron polarization at capture, assuming an initial polarization of 1.

Monte Carlo. We calculate this fraction both for the isotropic component of the capture-gamma distribution and for the parity-violating component, which has a $\cos(\theta)$ angular distribution with respect to the neutron polarization. The results as a function of the length of the array are shown in figure 29. For the proposed array size (60 cm), we accept 87% of the gammas associated with the parity-violating component of the signal.

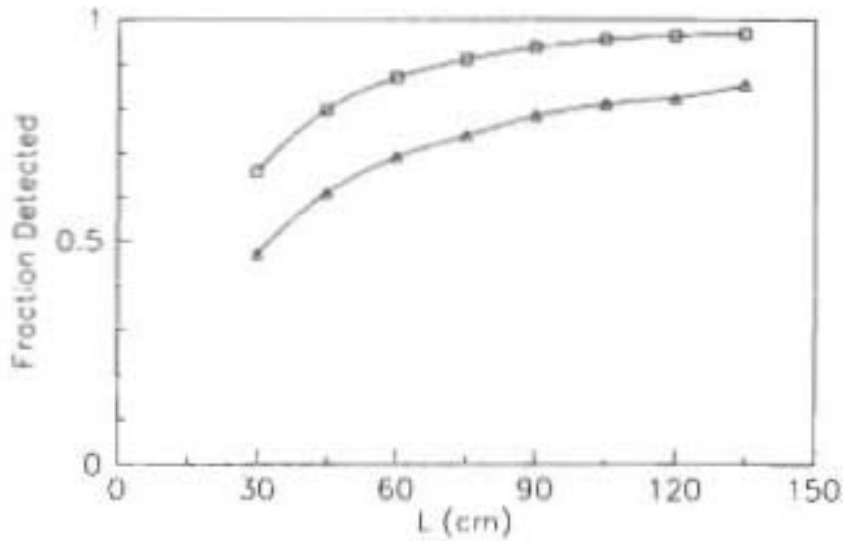

Figure 29: Monte Carlo calculation showing the fraction of gammas detected from parity-conserving (triangles) and parity-violating (squares) events as a function of detector length. The proposed length is 60 cm.

One needs to know the width of the electron-photon showers in the detector in order to know how much of the initial energy of a gamma ray that strikes a particular detector is distributed to neighboring detectors. We are performing simulations using the EGS4 code to see the spatial distribution of the energy deposited by a 2.2 MeV gamma in CsI detectors of our dimensions. Results are incomplete. We expect the transverse dimensions of the gamma shower to be near the Moliere radius of 2.73 cm, which sets the scale for the transverse size of electron-photon showers for higher-energy gamma showers.

It is important to understand the fluctuations in the average energy deposited per gamma. In normal gamma ray spectroscopy, the full energy of the gamma is typically deposited in each event. For N events in a narrow energy region corresponding to the full energy peak the fractional statistical error is simply $1/\sqrt{N}$. In current mode counting, however, all of the gamma events, whether or not they deposit their full energy, contribute something to the detector current. Thus the fractional statistical error in the detector current is larger than $1/\sqrt{N}$ for N incident gammas and depends on

the distribution of energy deposition in the detector.

Consider the asymmetry $A_\gamma = (Q_2 - Q_1)/(Q_2 + Q_1)$, where Q_1 and Q_2 are the total charge from the detector with and without spin flip (approximately equal in our case, since the asymmetry is so small). If q is the charge deposited from one incident gamma and there are N incident gammas in one of the spin flip states, then the fractional statistical error in A_γ is $\sqrt{(1 + \langle q^2 \rangle / \langle q \rangle^2)/2N}$ [91], which only reduces to the usual counting statistics estimate if there are no fluctuations in q. This extra contribution to the noise must be small relative to the usual $\sqrt{N}$ counting statistics in order for the predicted statistical accuracy of the experiment to be justified.

In our test experiment, we were able to place a constraint on the following effects

1. fluctuations in the scintillation light output for a given gamma ray energy due to the statistical nature of the conversion process,
2. variations in the light collection efficiency from different locations in the detector,
3. fluctuations in the amount of energy deposited in the gamma detector due to energy escaping the detector, and
4. fluctuations in the number of photoelectrons produced at the photocathode by the light.

This constraint applies for the smaller (approximately 7 cm × 10 cm × 15 cm) CsI detectors coupled to the photocathodes of Hamamatsu R5004 phototubes used in the test. By comparing the measured detector current noise to the rms shot noise $I/\sqrt{f} = \sqrt{2qI}$ expected from $\sqrt{N}$ counting statistics, we determined $\sqrt{1 + \langle q^2 \rangle / \langle q \rangle^2} = 1.5$. For the larger crystals that we propose to use in the experiment, we expect the contribution to the charge variations from this mechanism to be smaller. Simulations are in progress.

5.4 Neutron Guide and Shutter

The experiment requires a 10×10 cm^2 cross section neutron guide in order to achieve the proposed statistical accuracy in one year (live time). At MLNSC, the new bulk shield penetrations viewing the new LH_2 moderator (flight paths 12 and 13) were sized to use mercury shutters. They were not made to accommodate a neutron guide and a proper shutter system because of the limited space. We have been cooperating with LANSCE on the design of the new guide and shutter system. We have a conceptual design consisting of two separate neutron guide sections; one inside the existing bulk shield penetration and another in the external shutter mechanism that is enclosed in its shielding, as shown in figure 30.

The neutron guide inside the biological shield will be constructed in two sections that have to be externally aligned and then moved into position as a single unit. Both sections will consist of four super-mirror plates bonded to the inside of a precision glass cylinder to form a 10×10 cm^2 cross section guide. The cylinder provides support and rigidity for the thin (few-millimeter) super-mirror plates. The outer section will be supported in a steel frame, while the inner section will be cantilevered from the frame. This arrangement is necessary because the small diameter of the shield penetration near the interior does not allow space for any support structure. Engineering calculations confirm that this design will safely support the guide with acceptable sag and misalignment. The entire guide will be enclosed in a thin aluminum envelope, which will isolate the experiment from the spallation target vacuum and allow for helium gas cooling of the guide. Such cooling may be necessary to keep temperature of the guide below 80°C, where diffusion of the multi-layer surfaces

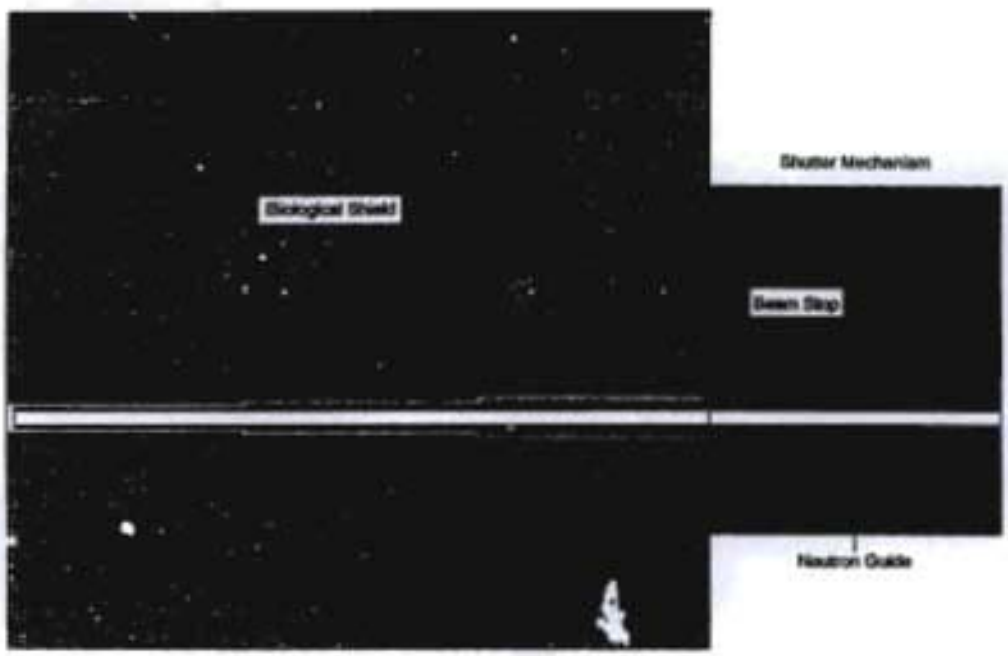

Figure 30: Concept of the neutron guide and shutter system. Not shown are the aluminum vacuum jacket around the guide inside the penetration of the biological shield and the extra shielding around the shutter mechanism. The beam stop is composed of polyethylene, steel, and tungsten, while the shutter block is made primarily of steel.

becomes possible. It is thought that elevated temperatures are more harmful to the guide than radiation damage. In any case, the mounting system will be designed to allow replacement of damaged guide sections.

The shutter mechanism will consist of a steel block, about 1.5 m long, with a penetration for a neutron guide, similar to the guide section inside the biological shield, to transport the beam when the shutter is open (the upper position). In the shutter closed position (the lower position) the beam will interact with the beam stop, a combination of polyethylene and steel layers surrounded by tungsten as indicated in figure 30. The shutter will be raised and lowered by pneumatic cylinders, and precision fixtures will establish the relative alignment of the fixed and movable guide sections when it is open. To keep the radiation levels to an acceptable level at the experimental room, the shutter mechanism has to be enclosed within a proper designed radiation shield.

6 Progress Expected in the Near Future

During the next MLNSC production cycle, we are planning a test experiment that will test several pieces of the experimental apparatus and will measure the sensitivity to as many systematic effects as possible. Since the beam line required for the final experiment will not be available, these tests will be done on an existing cold neutron beam line. We will construct a test apparatus consisting of 4 of the full complement of 48 detectors. The detectors, each a 15 cm cube of CsI(Tl) as in the full experiment, will be placed symmetrically up, down, left, and right around a polyethylene target. This target will be chosen to have the same diameter and hydrogen thickness as the LH_2 target. This test setup will allow for the development and test of the data acquisition system, as well as tests of many systematics.

The test will proceed in stages. In the first stage, bench tests will be performed, both with and without gamma sources, to test detector performance, data acquisition, noise levels, and electronic pickup. During this phase, the VME DAQ development will be completed. Stability of the detectors and associated electronics with temperature, time, and magnetic field will be established. Using light emitting diodes, we will measure the system linearity. In the second stage, the apparatus will be moved to an existing cold neutron beam line, with the beam being captured in the polyethylene target. This will allow systematic tests for asymmetries associated with drifts and with beam intensity and position modulations. In third stage, the beam will be polarized by a small ^{3}He polarizer. Tests for false asymmetries associated with neutron polarization will be conducted. In addition, development and testing of the RF spin flipper, magnetic guide field, and full-scale ^{3}He polarizer will be conducted.

At the end of this series of tests, all major components of the experiment, with the exception of the LH_2 target[3], will have been tested. In addition, the sensitivity of the apparatus to most systematic effects will have been established.

7 Conclusion

The parity violating asymmetry A_γ in $\vec{n} + p \rightarrow d + \gamma$ can be measured to a statistical accuracy of 5×10^{-9} in one year of data at the upgraded version of LANSCE now under construction. The systematic errors will be held below the statistical errors by creative use of the time structure of

[3]The development of the LH_2 target will proceed in parallel, but will not require a neutron beam.

a pulsed neutron source. A unique feature of this experiment is that A_γ determines the weak NN coupling H_π^1 with negligible uncertainty due to nuclear structure. The proposed measurement of H_π^1 will

1. unambiguously determine its value,
2. determine the longest range and most important of the weak NN couplings,
3. provide an essential step in over-constraining the weak NN couplings and testing the meson-exchange picture of the weak NN interaction, and
4. test QCD modifications of quark-quark neutral currents in bound systems; mesons and nucleons. The implications of the measurement of A_γ in $\vec{n} + p \rightarrow d + \gamma$ are discussed in more detail in section 1.8 at the end of the introduction.

A Budget and Manpower

The total request from DoE is $1675k. The total budget of the project consists of $2128k of unburdened capital equipment costs, which are itemized in table 6. Also shown is the responsible institute for each item and its status. The plan for the funding is presented in table 7. As can be seen from this table we are looking for funds from DoE, NSF, LANL, and the collaborating institutions. In addition to the capital equipment costs there are also $100k per year of operational costs, as indicated in table 8. All costs shown in the tables are unburdened. The operational costs will have the full laboratory burden. The capital equipment burden on the DoE funds is indicated in table 7.

Item	Cost ($k)	Institution	Status
Signal Processing	75	LANL	Design, prototype testing
Data Processing	53	LANL	DAQ software development
Detector	464	KEK	4 crystals ordered, CsI and tube testing
^{3}He Polarizer	148	Michigan	Preliminary design, test of concepts
Super Mirror Polarizer	40	NIST	Backup for ^{3}He, sources contacted
Spin Flipper	24	LANL	Prototype in fabrication
Spin Transport	25	Berkeley	Design, spin transport modeling
LH_2 Target	221	NIST	Conceptual design, preliminary quotes
Beam Monitor	8	Indiana	Preliminary design
Shielding	273	LANL	MCNP calculations, design
Clean Power and Grounds	30	LANL	Preliminary design
Neutron Transport	700	LANL	Design collaboration with LANSCE
Technician (0.5 FTE)	67	LANL	
Total	2128		

Table 6: Itemized capital equipment budget. Status of the item and the responsible institute is also indicated.

Brief description of the items and contingencies:

Signal Processing This item includes front-end electronics, such as preamplifiers and differential and summing amplifiers. The costs are reasonably well understood and therefore a contingency of 5% has been added.

Data Processing This item includes the online data acquisition system and off-line data analysis and data transfer devices. During the life of the experiment about three tera bytes of data will be accumulated. It is important for the success of the experiment that the outside collaborators have fast access to the data. A 5% contingency has been used since the costs are known.

Detector The detector size is determined by the size of the LH_2 target and the interaction length of the 2 keV gamma rays in CsI. The size of the individual crystals ($15 \times 15 \times 15$ cm^3) matches the crystal size resulting from the manufacturing process. This will reduce the costs because no extra cutting is required. The cost of the detector is based on list prices and quotations. A contingency of 5% is used.

^{3}He Polarizer The ^{3}He technology is known, but achieving 65% polarization is not trivial. We are testing new ideas to increase the performance of the ^{3}He polarizers. Most of the components have a list price. A contingency of 5% has been used.

Super Mirror Polarizer This system is a backup for the ^{3}He polarizer. The price is given by the manufacturer. No contingency, if contingency is required it can be taken from the ^{3}He polarizer.

Spin Flipper This item is straight forward to build and the costs of components are known. A contingency of 5% has been added.

Spin Transport This item includes a pair of "race track" shaped coils. The challenge is to match the field of this pair with the field requirement of ^{3}He polarizer and of the spin flipper. A contingency is 5% has been added.

LH_2 Target The liquid para-hydrogen density must be constant over the volume of the target, therefore there must be no bubbles. This is achieved by maintaining the temperature of the target below the boiling point with a closed-loop cryo cooler. Because of the n-^{27}Al reaction may create a spin-dependent asymmetry in the detector, the size of which is close to the expected asymmetry from the np capture reaction, the parts of the cryostat that are exposed to the neutron beam must be manufactured from zirconium. A contingency of 10% has been added because of the effect of the use of zirconium on the costs is not well understood.

Beam Monitor This item is required for the beam normalization. The costs are known and therefore a contingency of 5% is used.

Shielding This item includes the shielding around the neutron guide and experiment. The final costs of the shielding are mainly effected by two constraints. First, the experiment must be located at a minimum distance of 15 m from the neutron source to provide enough room for the apparatus. The 13 m long neutron guide must be shielded. Second, since this 10×10 cm guide directly views the moderator, allowing fast neutrons (> 1 keV) to reach the experiment, a proper beam dump and a polyethylene-steel combination shielding around the experiment are required to achieve the radiological levels defined by the facility. A contingency of 5% is used.

Clean Power and Ground From experience we know that the facility power is too noisy for this type of experiment and that there is no good ground available. We need to build both. No contingency.

Neutron Transport This item includes a 13 m long neutron super mirror guide, a mechanical shutter, and a frame definition chopper. A ~ 4 m long neutron guide with support will be mounted inside the biological shield. The shutter includes a massive block of steel, a 2 m long neutron guide, and a tungsten beam block. After the shutter we need to mount the frame definition chopper and 7 m of neutron guide. The design of the neutron guide and shutter mechanism is a collaborative effort with LANSCE. We plan to design a guide and shutter system that will maximize the available neutron flux, and therefore be well suited to future nuclear physics experiments, though not for neutron scattering experiments. At present we only have a conceptual design and therefore a contingency of 20% has been added.

Technician (0.5 FTE) During the peak capital equipment construction years (FY99 and FY00), additional technician support, at the level of 0.5 FTE above the existing support, is required.

Item	Base Costs ($k)	Proposed Funding Sources DoE New ($k)	NSF New ($k)	Collaboration ($k)
Signal Processing	75	70		5*
Data Processing	53	53		
Detector	464	379		35* + 50†
^{3}He Polarizer	148	88	50‡	10‡
Super Mirror Polarizer	40	40		
Spin Flipper	24	19		5*
Spin Transport	25			25§
LH_2 Target	221	52	100¶ + 50‖	11* + 8¶
Beam Monitor	8	8		
Shielding	273	132		141*
Clean Power and Grounds	30	30		
Neutron Transport	700	369		331*
Technician (0.5 FTE)	67	67		
Subtotal	2128	1307	200	621
LANL Capital Equipment Burden		368		
Total		1675		

*LANL
†KEK
‡Michigan
§Berkeley
¶Indiana
‖NIST

Table 7: Proposed funding sources.

The funding profile, shown in table 8, has been planned so that the main capital equipment construction will take place in 1999 and 2000. The important milestone is the installation of the shutter and neutron guide system. Installation will start during the January–February 1999 beam break and finish during the September–November 1999. This timing allows the experiment to begin beam-on systematic tests when the beam is available in February 2000. Most of the funding for the ^{3}He polarizer and the LH_2 target needs to occur in 1999 so that these important components are ready when the experiment starts to take data at the beginning of 2000. Some of the CsI crystals must be ordered in 1999, and the rest in 2000. The goal is to have the full detector operational in the middle of 2000.

Year (FY)	Capital Equipment ($k)	DoE ($k)	NSF ($k)	Collaboration ($k)	Operations ($k)
1998	250	65	0	185	20
1999	1279	654	200	426	70
2000	599	588	0	10	100
2001	0	0	0	0	100
2002	0	0	0	0	100
2003	0	0	0	0	100
Subtotal	2128	1307	200	621	490
LANL Capital Equipment Burden		368			
Total		1675			

Table 8: Projected profile for the capital equipment and operations budget.

Year (FY)	Scientists (FTE)	Postdocs (FTE)	Students (FTE)	Technicians (FTE)
1998	7	3	4	1.5
1999	8	4	5	2.5
2000	8	4	5	2.5
2001	8	4	5	1.5
2002	7	4	5	1
2003	7	4	4	1

Table 9: Projected profile for the all personnel.

Year (FY)	Scientists (FTE)	Postdocs (FTE)	Students (FTE)	Technicians (FTE)
1998	3	1.5	0.5	1
1999	3	2	1	1.5
2000	3	2	1	1.5
2001	3	2	1	1
2002	3	2	1	1
2003	3	2	1	1

Table 10: Projected profile for LANL personnel.

B Schedule

The schedule for the experiment depends upon the availability of the construction part of the funding and the availability of beam at MLNSC. The first important milestone is the installation of the shutter and neutron guide for the nuclear physics beam line. This allows the start the important testing of the systematics using the beam. The present plan is to start the installation of the shutter and neutron guide during the January–February 1999 beam break and complete the mounting during the September–November 1999 break. Our plan is to use this beam line for the first time starting in February 2000, first to test the different components of the experiment, and then to begin taking data in June 2000. In figure 31, we show the proposed schedule. The beam schedule is the present plan for MLNSC production; it includes start up and tuning, lasting up to two months of each running period. The facility has provided us with the plan for the MLNSC production only until year FY2002. Systematics studies will be conducted both with and without the beam. The first systematic studies will be done using the test beam line during the 1998 and 1999 run cycles.

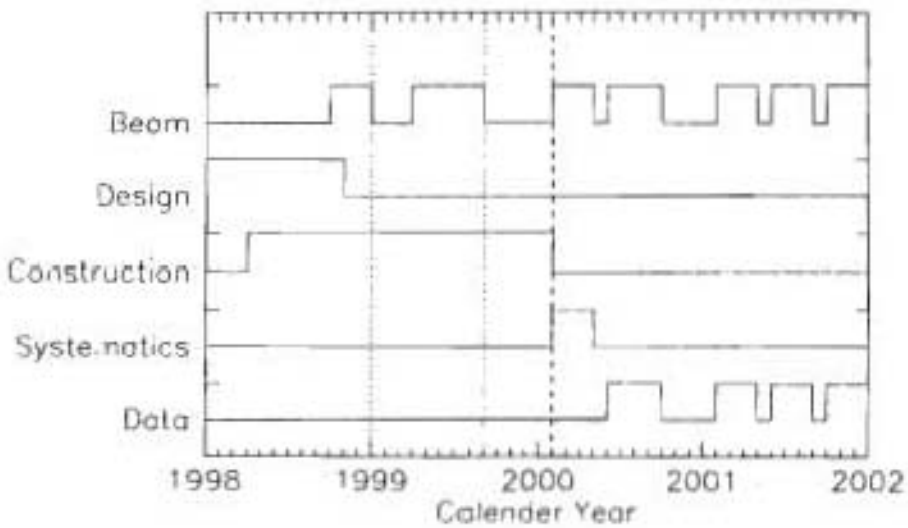

Figure 31: Proposed schedule indicating the design, construction, systematic test, and data collection phases. Also indicated are the expected periods of production beam at MLNSC. The dotted line represents the mounting of the neutron beam shutter and guide system, while the dashed line indicates the earliest possible start of data collection.

C Personnel

Los Alamos National Laboratory

J.D. Bowman Fellow. Extensive experience in the study of parity violation and fundamental symmetries: PV in compound nuclear reactions, PV in p–p interactions at 15, 800, and 6000 MeV. Symmetry violating processes: $\mu \to e + \gamma$ and $\mu \to e + \gamma + \gamma$. Extensive experience in detector development and methods to reduce systematic errors in symmetry tests.

G.L. Greene Staff Member. Active in the field of precision measurements and symmetry test with low energy neutrons for more than twenty years. Participated in the first observation of P-violating neutron spin precession and in measurements determining the mass, lifetime and magnetic moment of the neutron, among other activities.

G.E. Hogan Staff Member. Extensive experience in particle and nuclear physics experiments. Played a major part in the design, construction, and running of the MEGA ($\mu \to e + \gamma$) experiment. Experience in hardware (chambers, complex gas systems, scintillators) and software (analysis, databases, and stand alone DAQ systems) design and construction. Currently part of the Proton Radiography project. Designed and coded the PC DAQ program, a Windows based data acquisition program.

J.N. Knudson Staff Member. Participated in medium-energy nuclear physics research for more than fifteen years. Active participant in a program studying parity violation in nuclear systems for eight years.

S.K. Lamoreaux Staff Member. Extensive theoretical and experimental work in the applications of atomic systems and cold neutrons to the study of fundamental interactions. Participated in the most sensitive measurements of atomic and neutron electric dipole moments, and in the measurement of neutron-nucleon weak interactions by spin rotation.

G.L. Morgan Staff Member. Active in the field of nuclear physics at both low and intermediate energies for over thirty years. Participated in numerous experiments, principally at Los Alamos (LANSCE) and Oak Ridge (ORELA) in both pure and applied research in the field of neutron physics.

C.L. Morris Fellow, Extensive experience in medium energy physics. Active in the fields of cold and ultra cold neutron experimentation at LANSCE.

S.I. Penttilä Staff Member. Studied for years parity violation with low-energy neutrons, extensive experience in cryogenics and optically polarized ^{3}He, years of experience in MLNSC and its beam lines.

D.A. Smith Post-Doctoral Researcher. Active in research at Los Alamos for the past eight years. Performed the final experiments measuring parity violation in the compound nuclear system, along with auxiliary experiments into neutron resonance spectroscopy. Active in the development and use of polarized ^{3}He for the production of low-energy polarized neutron beams.

T.B. Smith Post-Doctoral Researcher. Completed a Ph.D. using a polarized ^{3}He target to study the spin structure of the neutron at SLAC. Participated in the Endstation A spin structure program at SLAC since 1992.

W.S. Wilburn Staff Member. Active in the field of symmetry tests in nuclear physics, including parity and time-reversal invariance. Precision measurements in few-nucleon systems. Measurements of gamma emission from neutron-induced reactions.

V.W. Yuan Staff Member. Involved for 20 years in symmetry measurements in the nucleon-nucleon system. Spokesman for the PV measurement in p-p scattering at 800 MeV. Helped start the program at Los Alamos to study parity violation in compound-nuclear resonances. Has participated in this program for 10 years. Currently is a co-principal investigator on experiments to use the Doppler broadening of neutron resonances to dynamically (on a short time scale) measure temperatures in material systems.

Petersburg Nuclear Physics Institute

A. Bashenov Staff Member. Participant of the experiment for measurement of circular polarization of gamma-rays during the capture of polarised neutrons by para-hydrogen. Participant in the Gatchina experiment searching for the neutron EDM. Involved in the development of electronic hardware for fundamental experiments.

E. Kolomenski Staff Member. Participant in the $\vec{n}+p \rightarrow d+\gamma$ experiment which measured the P-violating circular polarization. Also participated in the measurement of circular polarization of gamma-rays from the capture of polarised neutrons by para-hydrogen. Involved in development of Gatchina neutron EDM experiment.

A. Pirozhkov Staff Member. Participant in the $\vec{n}+p \rightarrow d+\gamma$ experiment which measured the P-violating circular polarization. Also participated in the measurement of circular polarization of gamma-rays from the capture of polarized neutrons by para-hydrogen. Involved in development of Gatchina neutron EDM experiment.

A. Serebrov Professor. More than 25 year experience of work with cold polarized and ultra cold neutrons. Participated in the EDM experiment with UCN from the beginning. Took measurements of neutron lifetime with gravitational trap of UCN. Involved in measurements of neutron beta-decay asymmetries with high precision. Conducted measurements of P-violating effect of neutron spin rotation in vicinity of the resonance. Design and production of cold neutron sources and ultra cold neutron sources.

University of Michigan

T.E. Chupp Professor. Expertise in polarization and symmetry experiments, particularly polarization of noble gases by laser optical pumping and polarized ^{3}He neutron spin filters. Recent experimental activity includes measurement of atomic electric dipole moments with optically pumped masers, probing nucleon structure by electron scattering from polarized targets and measurement of T-violation with polarized neutrons (emiT collaboration).

K.P. Coulter Assistant Research Scientist. Extensive experience in the production of polarized noble gases (H, D, ^{3}He, and ^{129}Xe) for symmetry and nuclear physics experiments. These include measurements of PV in compound nuclear reactions (including the first use of laser polarized ^{3}He as a neutron spin filter), nucleon spin structure using polarized electrons on polarized targets, and T-violation in polarized neutron beta-decay.

R.C. Welsh Postdoctoral Research Fellow. Expertise in nuclear physics experiments, specifically: tracking algorithms, data analysis, Monte Carlo simulations, data acquisition, on-line and off-line data presentation. Experimental experience in heavy ion nuclear collisions (LBL-DLS, BNL-878/896), deep inelastic scattering (SLAC-E154/E155), ^{3}He polarization techniques, and medical imaging.

J. Zerger Graduate Student. Working with Drs. Chupp, Coulter and Welsh on novel devices for polarizing ^{3}He with the spin exchange optical pumping method. Mr. Zerger was also an Academic All American Football Player in College.

University of California, Berkeley

S.J. Freedman Professor. Actively involved in experimental tests of the Electroweak Standard Model. Precision tests in nuclear and neutron beta decay. Searches for new particles and unexpected phenomena.

B.K. Fujikawa Staff Member. Extensive experience in precision nuclear beta decay measurements: partial lifetime of the super-allowed Fermi decay of ^{10}C, ^{14}C beta decay shape factor, and heavy neutrino searches in ^{35}S beta decay. Symmetry tests: T-violation with polarized neutrons (emiT). Experimental particle physics: neutrino oscillations (LAMPF E645).

National Institute of Standards and Technology

T.R. Gentile Staff Member. Development of neutron polarizers based on polarized ^{3}He, with emphasis on the metastability-exchange optical pumping method; neutron tomography.

G.L. Jones Staff Member. While at Princeton, Gordon Jones measured the beta asymmetry of ^{19}Ne as a search for right handed weak currents. Since 1996 he has worked at NIST where he has continued to study the symmetries of the weak interaction as part of the emiT collaboration. His primary work at NIST has been developing a polarized ^{3}He neutron spin filter for cold neutron beams at the NIST reactor.

F.E. Wietfeldt Staff Member. Three years of experience with fundamental nuclear physics experiments using polarized and unpolarized neutron beams at N.I.S.T. and the I.L.L. Participated in measurements of the free neutron lifetime, PNC neutron spin rotation in liquid helium, time reversal violation in neutron decay, and the neutrino-spin asymmetry coefficient in neutron decay.

University of New Hampshire

M.B. Leuschner Research Assistant Professor. Experience in polarization and parity violation experiments, including measurements with low energy neutrons and gamma ray asymmetries. Development of techniques for polarizing noble gases via the spin-exchange method.

V.R. Pomeroy Graduate Student. Recent participation in low energy neutron physics program at LANSCE. Development of polarized ^{3}He neutron spin filter. Extensive experience in spin-exchange techniques for polarizing noble gases.

Kyoto University

A. Masaike Professor. Working in the wide field of elementary particle physics, in particular precise test of symmetries, high energy spin physics, hyperon-nuclear interactions, high energy astro-physics, etc.

Y. Matsuda Graduate Student. Recently completed a Ph.D. on the study of parity violation in compound nuclear systems, carried out at LANSCE.

KEK National Laboratory

S. Ishimoto Staff Member. Active in the field of spin physics using polarized and liquid hydrogen targets for more than twenty years. Participated in the study and development of the polarized proton filter at KEK. Developed polarized proton and deuteron targets at KEK, LANL and CERN. Developed several types liquid hydrogen targets at KEK.

Y. Masuda Staff Member. Precision tests of symmetry violation in the nucleus. Polarization of neutrons and nuclei.

K. Morimoto Staff Member. Extensive experience in precision measurements.

Indiana University

C. Blessinger Graduate Student. Indiana/IUCF since summer 1997. M.S. in electrical engineering, Rose-Hulman 1996. Intended thesis: parity violation in $\vec{n} + p \rightarrow d + \gamma$.

G. Hansen Graduate Student. Indiana/IUCF since summer 1997. Working on development of polarized ^{3}He neutron polarizers. Designing a Stern-Gerlach analyzer for polarized neutrons.

H. Nann Professor. Experience in Monte-Carlo simulations for nuclear and high energy physics, magnet design, and low-energy neutron-induced reactions.

D.R. Rich Graduate Student. Active in the Weak Interactions Group at IUCF since 1994. Contributed to the measurement of parity violation in compound nuclear resonance scattering in Xe. Recent concentration in the development of polarized ^{3}He based neutron spin filters.

W.M. Snow Assistant Professor. Neutron weak interactions and neutron scattering. Measurement of the decay rate of the neutron. Parity violation in the *NN* interaction. Development of polarized ^{3}He targets as neutron polarizers. Development of advanced methods in neutron flux measurement

Joint Institute for Nuclear Research

E.I. Sharapov Staff Member. More than 30 years experience in the low energy neutron and gamma-ray spectroscopy, $(n,^3\mathrm{He})$, $(n,^6\mathrm{Li})$, $(n,^7\mathrm{Li})$ reactions, (n,d) capture. Fundamental symmetries with neutrons, participation in the first observation of parity violation in P-wave resonances and in systematic studies of the weak matrix element in heavy nuclei.

D Publications and Presentations

Papers

1. W.S. Wilburn and J.D. Bowman. *Consistency of parity-violating pion-nucleon couplings extracted from measurements in ^{18}F and ^{133}Cs.* Physical Review C. Accepted for publication.

2. W.M. Snow, W.S. Wilburn, J.D. Bowman, M.B. Leuschner, S.I. Penttilä, V.R. Pomeroy, D.R. Rich, E.I. Sharapov, and V. Yuan. *Progress toward a new measurement of the parity violating asymmetry in $\vec{n} + p \rightarrow d + \gamma$.* Submitted to Nuclear Instruments and Methods.

3. A. Csótó and B.F. Gibson. *Parity conserving γ asymmetry in n-p radiative capture.* Physical Review C **56**, 631 (1997).

Contributed Talks

1. W.S. Wilburn, J.D. Bowman, S.I. Penttilä, V. Yuan, M.B. Leuschner, V.R. Pomeroy, D.R. Rich, W.M. Snow, and E.I. Sharapov. *Low-noise photocathode preamplifiers for measuring A_γ in $\vec{n} + p \rightarrow d + \gamma$.* Bulletin of the American Physical Society **42**, 1667 (1997).

2. W.S. Wilburn and the npdg collaboration. *A proposed experiment to measure A_γ in $\vec{n} + p \rightarrow d + \gamma$ at LANSCE.* Bulletin of the American Physical Society, to appear.

3. C. Blessinger and the npdg collaboration. *Parity violation in polarized neutron capture on protons: Target and detector simulations.* Bulletin of the American Physical Society, to appear.

4. W.M. Snow and the npdg collaboration. *Parity violation in polarized neutron capture on protons: An analysis of systematic effects.* Bulletin of the American Physical Society, to appear.

Seminars and Colloquia

1. J.D. Bowman. *Parity violation in $\vec{n} + p \rightarrow d + \gamma$.* Technical Seminar. Los Alamos National Laboratory, Los Alamos, NM. October 21, 1997.

2. J.D. Bowman. *Parity violation in $\vec{n} + p \rightarrow d + \gamma$.* Technical Seminar. Hebrew University, Jerusalem, Israel. October 28, 1997.

3. J.D. Bowman. *Parity violation in $\vec{n} + p \rightarrow d + \gamma$.* Technical Seminar. Tel Aviv University, Tel Aviv, Israel. November 4, 1997.

4. W.S. Wilburn. *The f_π controversy: ^{18}F, anapoles, and the future.* Technical Seminar. National Institute for Standards and Technology, Gaithersburg, MD. December 12, 1997.

5. J.D. Bowman. *Measurement of the Parity-Violating Gamma Asymmetry A_z in $\vec{n}+p \rightarrow d+\gamma$.* Presentation to the Physics Division Advisory Committee. Los Alamos National Laboratory, Los Alamos, NM. January 27, 1998.

6. W.M. Snow. *Weak interactions of low energy neutrons.* Physics Department Colloquium. University of New Hampshire, Durham, NH. February 4, 1998.

7. W.S. Wilburn. *The f_π controversy: ^{18}F, anapoles, and the future.* Nuclear Physics Seminar. Indiana University Cyclotron Facility, Bloomington, IN. February 20, 1998.

8. J.D. Bowman. *Parity Violation in the weak hadronic interaction, $\vec{n}+p \rightarrow d+\gamma$.* Physics Colloquium. Catholic University, Washington, DC. April 2, 1998.

References

[1] E.G. Adelberger and W.C. Haxton, Ann. Rev. Nucl. Part. Sci. **35**, 501 (1985).

[2] Yu. Abov *et al.*, Phys. Lett. **12**, 25 (1964).

[3] G. Arnison *et al.*, Phys. Lett. **166B**. (1986).

[4] UA2 Collaboration, Z. Phys. C **30**, 1 (1986).

[5] UA2 Collaboration, Z. Phys. C **47**, 11 (1990).

[6] F. Abe *et al.*, Phys. Rev. D **44**, 29 (1991).

[7] S. Abachi *et al.*, Phys. Rev. Lett. **75**, 1456 (1995).

[8] B. Desplanques, J.F. Donoghue, and B.R. Holstein, Ann. Phys. **124**, 449 (1980).

[9] B. Desplanques, in *Parity-Non-Conserving Nucleon-Nucleon Interactions*, edited by N. Auerbach and J.D. Bowman (World Scientific, Singapore, 1996), p. 98.

[10] J.F. Caviagnac, B. Vignon, and R. Wilson, Phys. Lett. **B67**, 148 (1977).

[11] V.A. Knyaz'kov, E.M. Kolomenskii, V.M. Lobashov, V.A. Nazarenko, A.N. Pirozhov, A.I. Shablii, E.V. Shalgina, Y.V. Sobolev, and A.I. Yegorov, Nucl. Phys. **A417**, 209 (1984).

[12] E.D. Earle, A.B. McDonald, S.H. Kidner, E.T.H. Clifford, J.J. Hill, G.H. Keech, T.E. Chupp, and M.B. Schneider, Can. J. Phys. **66**, 534 (1988).

[13] C. Bennet, M.M. Lowry, and K. Krien, proposal (unpublished).

[14] W.C. Haxton, Phys. Rev. Lett. **46**, 698 (1981).

[15] Ya. B. Zel'dovich, Zh. Eksp. Teor. Fiz. **33**, 1531 (1958).

[16] A. Bohr and B.R. Mottelson, *Nuclear Structure* (W.A. Benjamin, New York, 1969), Vol. I.

[17] V.F. Dmitriev and V.B. Telitsin, Nucl. Phys. **A613**, 237 (1997).

[18] V.V. Flambaum and I.B. Kriplovich, Zh. Eksp. Teor. Fiz. **79**, 1656 (1980).

[19] W.C. Haxton, Science **275**, 1753 (1997).

[20] W.C. Haxton, E.M. Henley, and M.J. Musolf, Phys. Rev. Lett. **63**, 949 (1989).

[21] V.V. Flambaum and D.W. Murray, Phys. Rev. C **56**, 1641 (1997).

[22] C.S. Wood, S.C. Bennett, D. Cho, B.P. Masterson, J.L. Roberts, C.E. Tanner, and C.E. Wieman, Science **275**, 1759 (1997).

[23] W.S. Wilburn and J.D. Bowman, Phys. Rev. C , accepted for publication.

[24] P.A. Vetter, D.M. Meekhof, P.K. Majumder, S.K. Lamoreaux, and E.N. Fortson, Phys. Rev. Lett. **74**, 2658 (1995).

[25] A.R. Berdoz *et al.*, in *Proceedings of the Sixth Conference on Intersections between Particle and Nuclear Physics*, edited by T.W. Donnelly (AIP Press, Woodbury, New York, 1997), Vol. 412.

[26] V.M. Lobashov, D.M. Kaminker, G.I. Kharkevich, V.A. Kniazkov, N.A. Lozovoy, V.A. Nazarenko, L.F. Sayenko, L.M. Smotritsky, and A.I. Yegorov, Nucl. Phys. **A197**, 241 (1972).

[27] V.N. Litvinenko *et al.*, Phys. Rev. Lett. **78**, 4569 (1997).

[28] Y. Avishai and P. Grange, J. Phys. G **10**, L263 (1984).

[29] B. Heckel, Nucl. Instrum. Methods A **284**, 66 (1989).

[30] G.A. Miller, 1998, private communication.

[31] E.M. Henley, W-Y.P. Hwang, and L.S. Kisslinger, Phys. Lett. B **367**, 21 (1996).

[32] R.F. Dashen, S.C. Frauchi, M. Gell-Mann, and Y. Hara, in *The Eight-Fold Way*, edited by M. Gell-Mann and Y. Néemann (W.A. Benjaman, New York, 1964).

[33] D.B. Kaplan and M.J. Savage, Nucl. Phys. **A556**, 653 (1993).

[34] G.S. Danilov, Phys. Lett. **18**, 40 (1965).

[35] B. Desplanques and J. Missimer, Nucl. Phys. **A300**, 286 (1978).

[36] V. Lobashov, V. Nazarenko, V.A. Saenko, L.F. Smotritisky, and O.I. Kharkevitch, JETP Lett. **5**, 59 (1967).

[37] V. Lobashov, V. Nazarenko, V.A. Saenko, L.F. Smotritisky, and O.I. Kharkevitch, Phys. Lett. **B25**, 104 (1967).

[38] P.W. Lisowski, C.D. Bowman, G.J. Russell, and S.A. Wender, Nucl. Sci. Eng. **106**, 208 (1990).

[39] O. Schaerpf, Physica B **156 & 157**, 631 (1989).

[40] G.L. Greene, A.K. Thompson, and M.S. Dewey, Nucl. Instrum. Methods A **356**, 177 (1995).

[41] L. Pasell and R.I. Schermer, Phys. Rev. **150**, 146 (1966).

[42] K.P. Coulter *et al.*, Nucl. Instrum. Methods A **288**, 463 (1990).

[43] F. Tasset, T.E. Chupp, J.P. Pique, A. Steinhof, A. Thompson, E. Wasserman, and M. Ziade, Physica B **180**, 896 (1992).

[44] R. Surkau *et al.*, Nucl. Instrum. Methods A **384**, 444 (1997).

[45] M.A. Bouchiat, T.R. Carver, and C.M. Varnum, Phys. Rev. Lett. **5**, 373 (1960).

[46] W.A. Fitzsimmons, L.L Tankersly, and G.K. Walters, Phys. Rev. **179**, 156 (1969).

[47] T.E. Chupp and K.P. Coulter, Phys. Lett. **55**, 1074 (1985).

[48] T.E. Chupp, M.E. Wagshul, K.P. Coulter, A.B. McDonald, and W. Happer, Phys. Rev. C **36**, 2224 (1987).

[49] T.B. Smith *et al.*, 1995, demonstration of 65% ^{3}He polarization with a laser diode array.

[50] T.E. Chupp and M.E. Wagshul, Phys. Rev. A **49**, 3854 (1994).

[51] M. Romalis, 1997, private communication.

[52] T.G. Walker, Phys. Rev. A **40**, 4959 (1989).

[53] T.E. Chupp, K.P. Coulter, S.R. Hwang, T.B. Smith, and R.C. Welsh, J. Neutron Res. **5**, 11 (1995).

[54] G.D. Cates, 1997, private communication.

[55] B. Larson *et al.*, Phys. Rev. A **44**, 3108 (1991).

[56] K. Abe *et al.*, Phys. Rev. Lett. **79**, 26 (1997).

[57] T.E. Chupp, R.A. Loveman, A.K. Thompson, A.M. Bernstein, and D.R. Tieger, Phys. Rev. C **45**, 915 (1992).

[58] F.D. Colgrove, L.D. Schaerer, and G.K. Walters, Phys. Rev. Lett. **8**, 439 (1962).

[59] J. Becker, W. Heil, B. Krug, M. Leduc, M. Meyerhoff, P.J. Nacher, E.W. Otten, T. Prokscha, L.D. Schearer, and R. Surkau, Nucl. Instrum. Methods A **346**, 45 (1994).

[60] N.K. Sherman, Nucl. Instrum. Methods **116**, 301 (1974).

[61] M.E. Sadler *et al.*, Phys. Lett. **B119**, 69 (1982).

[62] M. Kobayashi *et al.*, Jap. Journ. Appl. Phys. **24**, 593 (1985).

[63] K. Komisarcik *et al.*, Nucl. Instrum. Methods A **248**, 291 (1986).

[64] J.M. Cameron, Nucl. Instrum. Methods A **305**, 257 (1991).

[65] N.S. Sullivan, D. Zhou, and C.M. Edwards, Cryogenics **30**, 734 (1990).

[66] H. Grassmann *et al.*, Nucl. Instrum. Methods **228**, 323 (1985).

[67] H. Kobayashi, 1988, KUNS-900

[68] I. Holl *et al.*, IEEE Trans. Nucl. Sci. **35**, 105 (1988).

[69] C.F.G. Delaney and A.M. Lamki, Int. J. App. Radiat. Isotopes **19**, 169 (1968).

[70] E. Friez *et al.*, Bull. Am. Phys. Soc. **42**, 994 (1997).

[71] D. Renker, in *Proceedings of the ECFA Study Week on Instrumentation for High-Luminosity Hadron Collider* (CERN, Geneva, 1989), Vol. CERN 89-10.

[72] G.E. Hogan, 1998, http://pchogan.lampf.lanl.gov/proton/.

[73] R. Gamblin and T. Carver, Phys. Rev. **138**, A946 (1965).

[74] G.D. Cates, S. Schaefer, and W. Happer, Phys. Rev. A **37**, 2877 (1988).

[75] W.S. Wilburn, Ph.D. thesis, Duke University, 1993.

[76] R.A. Arndt, phase-shift analysis SM97, 1997, (private communication).

[77] A. Csótó, B.F. Gibson, and G.L. Payne, Phys. Rev. C **56**, 631 (1997).

[78] A.N. Bazhenov *et al.*, Phys. Lett. **B289**, 17 (1992).

[79] M.J. Berger and S.M. Seltzer, in *Studies in Penetration of Charged Particles in Matter* (National Academy of Science—National Research Council, Washington, DC, 1964), p. 69.

[80] J. Andrezwski *et al.*, in *AIP Report* (AIP Press, Woodbury, NY, 1991).

[81] M.A. Lone, D.C. Santry, and W.M. Inglis, Nucl. Instrum. Methods **174**, 521 (1980).

[82] N.R. Roberson *et al.*, Nucl. Instrum. Methods A **326**, 549 (1993).

[83] T.W. Bradshaw and J.O.W. Norris, Rev. Sci. Instrum. **58**, 83 (1986).

[84] M. Devoret, N.S. Sullivan, D. Esteve, and P. Deschamps, Rev. Sci. Instrum. **51**, 1220 (1980).

[85] W.D. Seiffert, Technical Report No. EUR 4455d. Euratom (unpublished).

[86] J.J. Szymanski, J.D. Bowman, P.P.J. Delheij, C.M. Frankle, J. Knudson, S. Penttila, S.J. Seestrom, S.H. Yoo, V.W. Yuan, and X. Zhu, Nucl. Instrum. Methods A **340**, 564 (1994).

[87] Avenier *et al.*, Nucl. Phys. **A436**, 83 (1985).

[88] D.R. Rich *et al.*, 1998, in preparation.

[89] R.E. MacFarlane, Technical Report No. LA-12146-C, Los Alamos National Laboratory (unpublished).

[90] V.F. Turchin, *Slow Neutrons* (Israel Program for Scientific Translations, Jerusalem, 1965).

[91] J.D. Bowman and J.C. Vanderleeden, Nucl. Instrum. Methods **85**, 19 (1970).